Characterization and Modulation of Electrochemical Processes at the Cathode-Electrolyte Interface in Lithium-Ion Batteries

By

Shuyu Fang

A dissertation submitted in partial fulfillment of

the requirements for the degree of

Doctor of Philosophy

(Chemistry)

at the

UNIVERSITY OF WISCONSIN – MADISON

2017

Date of final oral examination: 2/1/2017

Members of the Final Oral Committee:
      Robert J. Hamers, Professor, Chemistry
      Song Jin, Professor, Chemistry
      Dane Morgan, Professor, Material Science and Engineering
      John C. Wright, Professor, Chemistry
      Kyoung-Shin Choi, Professor, Chemistry

Characterization and Modulation of Electrochemical Processes at the Cathode-Electrolyte Interface in Lithium-Ion Batteries

Shuyu Fang

Under the supervision of Professor Robert J. Hamers

University of Wisconsin-Madison

Abstract

Advancement of battery technology requires cathode materials with high capacity and stable cycle performance. The application of high-voltage cathode such as $LiNi_xMn_yCo_{1-x-y}O_2$ (NMC) poses new challenges in sustaining stable cathode-electrolyte interface, which is key to long-term performance. The solution is to be obtained through careful examination of electrochemical processes at the cathode-electrolyte interface and development of treatment strategies to modulate these processes.

This thesis begins with an analytical study of the cathode-electrolyte interphase (CEI). X-ray photoelectron spectroscopy (XPS) is chosen as the primary characterization technique, and a combination of correlation analysis and binder-free cathode preparation method removes the ambiguity in peak assignation and CEI quantification. We have found, quite interestingly, that the CEI layer contains electrolyte decomposition products that originate from the anode side and then migrate to the cathode. It is also found that Al_2O_3 coatings can effectively reduce the deposition of anode-originated migrants. This work leads to new insight on the CEI concept and new design principles of cathode coatings. Following this work, Chapter 3 focuses on the development of Si-containing organic coatings. Through modulation of coating coverage, we achieved 27% improvement in capacity after 100 cycles. Mechanistic study with XPS, ICP, thermal mass spectrometry and impedance spectroscopy reveals a clear coverage-performance correlation. It is believed that the Si-containing coatings have two functions - facilitation of interfacial charge-transfer, and suppression of electrolyte decomposition. The hydrophobicity of coatings is identified as a key property for assisting lithium-ion desolvation at the interface. Finally, Chapter 4 presents a novel *in situ* method for battery failure diagnosis. Raman mapping technique is used to construct state-of-charge images of a working NMC cathode, which reveals the intrinsic inhomogeneity in the cathode failure process.

Acknowledgments

I certainly am very lucky to have gone this far in my academics, and that is largely because of the people who I met through the journey and who supported me altruistically.

My PhD advisor, Professor Robert Hamers, is the first person I would like to acknowledge. Bob appreciates the work of his students. He is enlightening when you get stuck; and encouraging when you have new ideas. I certainly am very lucky to have him as my advisor, and owe him a million thanks for always dragging me out of the mud and lighting up my day.

I am lucky to have met excellent mentors and coworkers who share my passion on battery research. Xin Chen, Juan Tuberquia, Joe Yeager and Monica Urey are my earliest mentors on batteries. My PhD project is funded by the Dow Chemical Company, and my project managers, Dr. Dee Strand, Dr. Mike Olken, and Dr. Mark Dreibelbis, have been excellent supporters and reviewers of my research. For the most part of my study, I have worked with David, Wansoo, Ha, Shenzhen and Laskar, and it is amazing that we've collaborated for so long and learned so much from each other. Laura Slaymaker joined the battery team later, and she is a truly nice coworker and travel companion. And of course, Sarah Guillot, who is going to take up the same torch after I leave.

I do not seem to have enough space acknowledging everyone that I've worked with in the Hamers group. Jamie, my officemate and consultant on so many things; Caroline, Yizheng and Di, who got me started in the lab; Rose and Kacie, whom I had a short overlap with but learned a lot from even after they left the group; Linghong, my peer and a great friend; Mimi, so considerate and always willing to help people; and Margy, Arielle, Tim, Kirsten and Shuo, I am lucky to have worked with you all.

The last part is dedicated to my family. Among all the wonderful things in my life, they are the best part. My parents have been devoted to my education in the earlier days and supportive of my choice after I left home. I am still amazed at their wisdom when facing life's challenges and many choices. Yue, my husband, is a great partner in life and a surprisingly good pal in science as well. Having them is the luckiest thing in my life, and it heartens me knowing that they will continue to stand by my side in the years to come.

Table of Contents

Chapter 1

Introduction and Background

1.1 Rechargeable Lithium-ion Batteries

Batteries provide a means to covert between electrical and chemical energy.[1] The first practical battery was the "electric pistol" invented by Alessandro Volta in 1800. In the 1970s, damand of consumer electronics accelerated the commercialization of lithium pimary batteries, and stimulated the interest in secondary, rechargeable systems that can be charged and discharged multiple times.[2] In 1980s, Goodenough and co-workers demonstrated compounds for rechargable lithium-ion batteries that are still used almost exclusively today.[4] Following that, Sony Coorporation commercialized the first lithium-ion battery in 1991.[6] Over the past decade, lithium-ion batteries have become the power source of choice for portable electronics and electric vehicles.

Illustrated in figure 1.1 is a rechargeable lithium-ion battery consisting of a positive electrode (cathode), a negative electrode (anode), separated by an electrolyte solution and a porous membrane (separator). Both the anode and cathode are compounds that can reversibly accept and release lithium ions from their open structure and assume various valence states.[2] Classical materials are $LiCoO_2$ cathode and graphite anode. The electrolyte is a lithium-conductive and electron-insulating media that is usually a liquid containing organic carbonate compounds and dissociated lithium salts,[3] but can also be a solid material with proper ion conductivity.[5] The separator can be a microporous plastic film, gelled electrolyte or other porous inert material that permeates electrolyte and insulates electrons.[7] In a charged battery, a spontaneous chemical occurs involving reduction of the cathode and oxidation of the anode. Li^+ is never reduced or oxidized, but it migrates from anode to cathode through electrolyte and induces an oxidative or reductive reaction of its host. Electrons flow externally from cathode to anode, providing energy to other devices. After full discharge of the battery, external current can be applied in the opposite direction to drive the reversed processes and store energy back in the battery.

The amount of electrical energy a battery delivers is linked to the chemistry of materials and cell construction. Energy is associated with the cell capacity and voltage. The *open-circuit potential (OCP)*
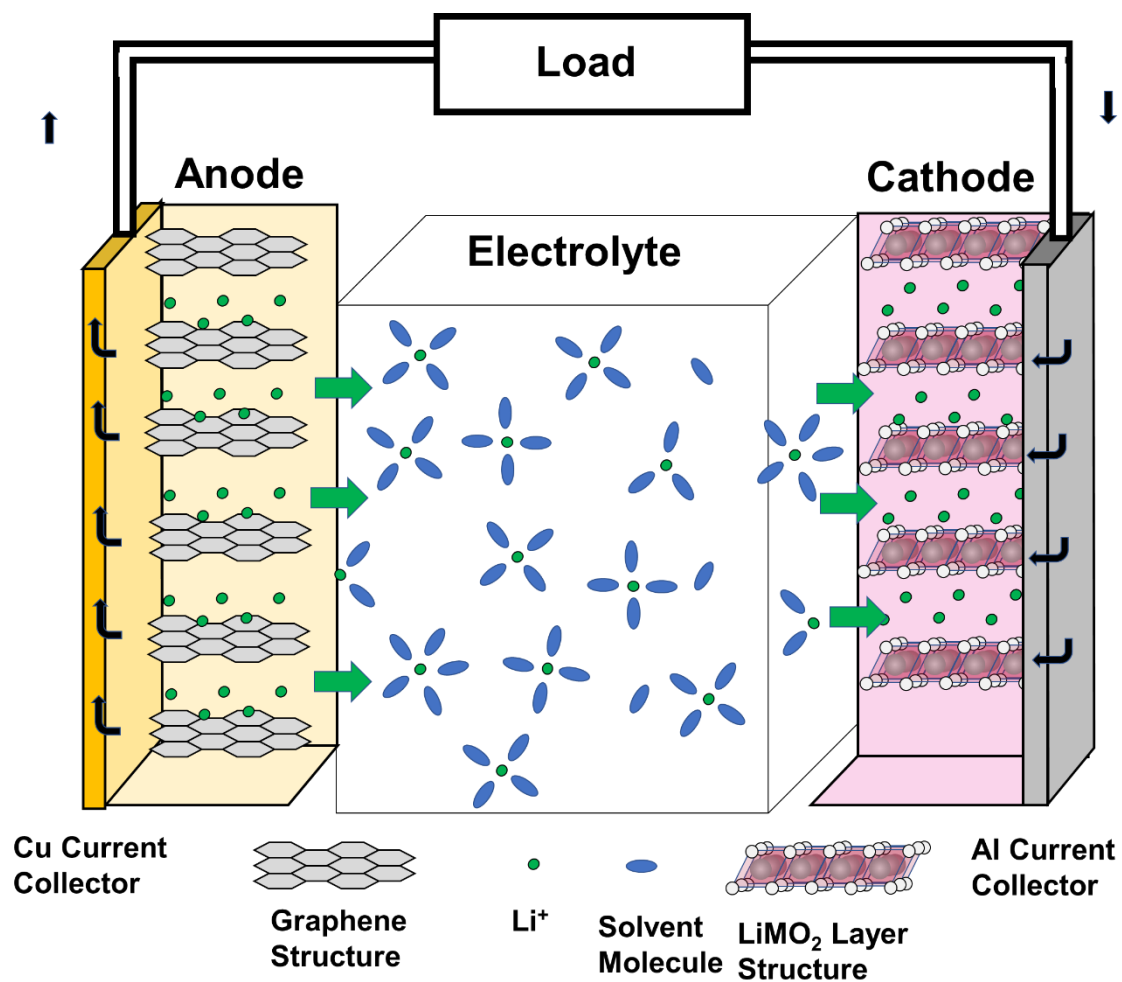
Figure 1.1 Schematic representation of a secondary lithium ion battery that employs graphitic carbon as anode and layered transition metal oxide as cathode. Graph adapted from reference [3] and reference [5].

is the voltage one would measure given no load between the cathode and anode. It is a function of the two active materials that are undergoing the reduction and oxidation chemistry as well the state of charge of the battery. In galvanostatic charge-discharge test, current is expressed in terms of *C-rate* that is a measure of current relative to its maximum capacity. A 1C discharge rate means that the current will discharge the entire battery in 1 hour. A C/10 charge rate means that the current will charge the battery in 10 hours. *Capacity* characterizes the total Amp-hours available between the fully-charged and fully-discharged states. It is calculated by multiplying the charge-discharge current (in Amps) by the time (in hours). *Capacity* usually decreases with increasing *C-rate* due to kinetic limitations at high current. *Coulombic Efficiency* refers to the ratio of discharge capacity vs. charge capacity. It can be used to evaluate the amount of capacity lost to thermal heating due to internal resistance or side reactions such as electrolyte decomposition. The charge-discharge capacity usually decays over repeated cycling, and the number of cycles before the battery fails to meet specific performance criteria is given by *cycle life*. The *cycle life* is dependent on the nature of interfaces between the electrode and electrolyte.[8]

1.2 Processes at the Electrolyte-Electrolyte Interface

The operation window of a battery is determined by the chemical properties of cathode, anode, and electrolyte. As illustrated in Fig. 1.2, the Fermi energies of cathode (μ_c) and anode (μ_a) should fall within the electrolyte stability window to avoid oxidation and reduction of the electrolyte itself.[9] In practice, graphite or lithium anode operates near 0 V vs. Li/Li$^+$ with μ_a above LUMO level of common electrolyte.[9-11] At such reducing potentials, electrolyte will decompose on the surface of anode, forming a solid-electrolyte interphase (SEI) layer.[12-14] Major electrolyte decomposition products include RCOOLi, ROLi, ROCO$_2$Li, LiF and Li$_x$MF$_y$.[10, 15-20] Property of the SEI layer determines the cycle ability of the anode. For a lithium anode, the passivation SEI layer creates a barrier for electron transfer from anode to electrolyte and thus enables operation of the anode above the electrolyte LUMO level. However, on repeated charge/discharge cycles, breaking of the SEI layer in selected areas results in the formation of dendrites that can grow across the electrolyte to short-circuit the battery with dangerous consequences[9]. In contrast to the lithium anode with large volume fluctuation during charge-discharge,
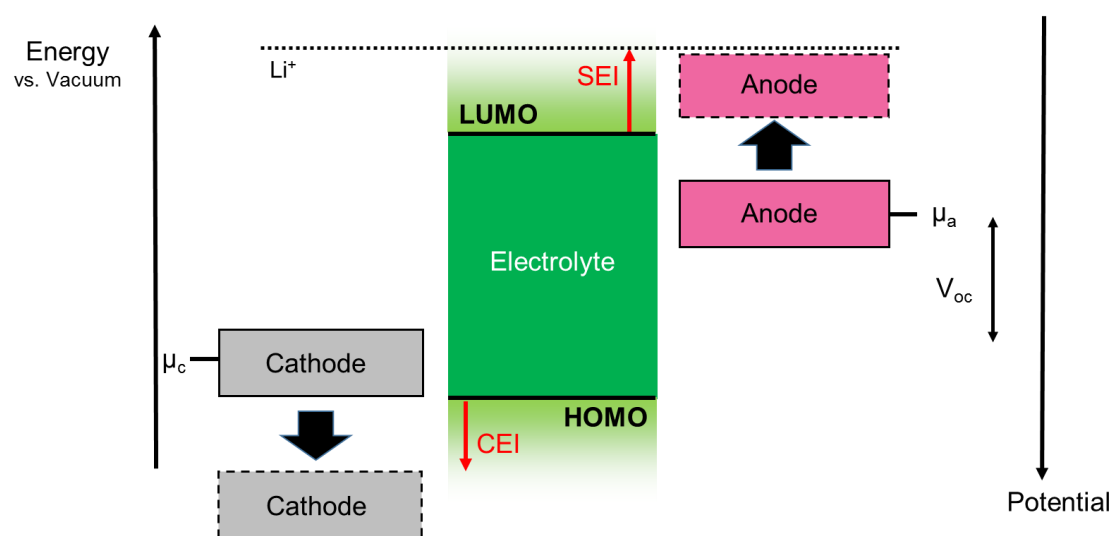
Figure 1.2 Energy diagram of a lithium-ion battery. Figure adapted from reference [3].

graphite anode demonstrates a small volume change that enables precipitation of a compact SEI layer. The good adhesion of SEI layer to the anode leads to a stable cycle performance.[21] Formation of SEI layer is an irreversible reaction that is associated with a loss of cell capacity. Therefore, self-limited SEI formation is highly desirable. Other desired SEI properties include compactness, high ionic conductivity and uniformity.

Practical cathodes such as $LiCoO_2$ operate below 4.5V, and the potentials are within the electrochemical stability window of common electrolyte. Despite some early uncertainty about the validity of the SEI-layer concept for the cathodes, it is soon realized that the surface chemistry is also decisive in determining cycle ability of cathodes.[22] A layer of cathode-electrolyte interphase (CEI) is detectable with impedance spectroscopy, FTIR and XPS.[22-23] It is commonly believed that CEI forms through nucleophilic or oxidation reactions between the oxide (cathode) and solvent molecules (electrolyte), but there also exists a to-be-proved proposal that reduced electrolyte species on anode can saturate electrolyte and reprecipitate on the cathode side[10]. Unlike anode-originated SEI, naturally-formed CEI may not provide complete coverage of cathode and thus grow continuously over cycles.[22, 24] Continuous CEI formation will constitute additional resistance, deplete accessible lithium and thus deteriorate the cathode performance in the long term. It is desirable to develop means to passivate the cathode surface based on good understandings of the properties and formation mechanism of CEI.

1.3 Cathode Material for Lithium-ion Batteries

In view of the current battery technology, capacity of cathode material is a major limiting factor of battery performance. Graphite and silicon anode have theoretical capacity values of 372 and 3579 mAh/g respectively, and for a layered $LiCoO_2$ cathode, the specific capacity is 135 mA.h/g.[25] New technology seeks to improve the capacity and energy density of cathode while not cannibalizing cost and safety. Olivine-structure materials such as $LiFePO_4$ have 1-D lithium-diffusion channels. The $LiFePO_4$ material features high rate-capability, high safety, reduced cost but relatively low potentials (<2.5 V vs. Li/Li^+) and low energy density.[26] Layered-structure cathodes such as Li_xMO_y (M= Mn, Ni, or binary /ternary mixture with Co) have 2-D lithium-intercalation channels and operate at relatively higher voltage.[27-28] Compared with conventional $LiCoO_2$, the introduction of other highly redox active

couples shifts the Fermi energy of the cathode,[5] leading to greatly improved voltage (~ 4.5 V vs. Li/Li$^+$) and capacity (up to 200 mA.h/g) over LiCoO$_2$.[27] A third group of material under study is the spinel-structure material such as Li$_x$Mn$_2$O$_4$, which has 3-D intercalation channels that possess more intercalation sites, but serious structural distortion during cycling limits its accessible capacity.[29-31] One recent approach for developing high-voltage cathode is the synthesis of lithium-rich material xLi$_2$MnO$_3$·(1−x)LiMO$_2$. The material can demonstrate higher than 200 mA.h/g capacity and up to 5 V voltage.[32] However, a serious voltage fade over cycles[33-34] limits its application.

Among a variety of cathode candidate, ternary compound NMC with formula LiNi$_x$Mn$_x$Co$_{1-2x}$O$_2$ has received great attention over the past decade.[28, 35-46] In 2014, sale of NMC came just next to LiCoO$_2$ in 35k tons per year.[47] NMC has a layered rock-salt structure, and its capacity can reach up to 200 mA.h/g.[28, 35-45] One problem of NMC is the relatively large irreversible capacity loss over cycles, especially at high upper cutoff voltages and at high temperature.[36-39] Performance degradation is associated with cathode overcharge due to loss of lithium on the anode side, as well as electrolyte decomposition at the cathode-electrolyte interface that leads to impedance build-up.[48]

1.4 Previous Study on Cathode Coatings

Among the strategies to improve cycle retention of cathode, one is to modify the cathode with organic and inorganic coatings to reduce CEI formation, facilitate ion transport, and suppress material deterioration. Some of the previous literature study is summarized below.

1.4.1 Nanometer-thick ceramics

Thin layers of metal oxides can be applied as cathode coatings, and thickness control is crucial to maintaining conductivity owing to the insulating nature of these coatings. One highly successful example is Al$_2$O$_3$, whose application greatly improves the capacity retention of high-voltage cathode by suppressing interfacial side reactions.[49-58] Other examples include SiO$_2$,[59] MgO,[60] ZrO$_2$,[61] TiO$_2$[60] and ZnO.[62] The thin metal oxides can be applied via so-gel approach, deposition, and direct assembly of colloidal particles,[25, 63] and atomic layer deposition (ALD) stands out as an excellent way to apply homogeneous, conformal coatings with controllable thickness.[64] ALD consists of a series of
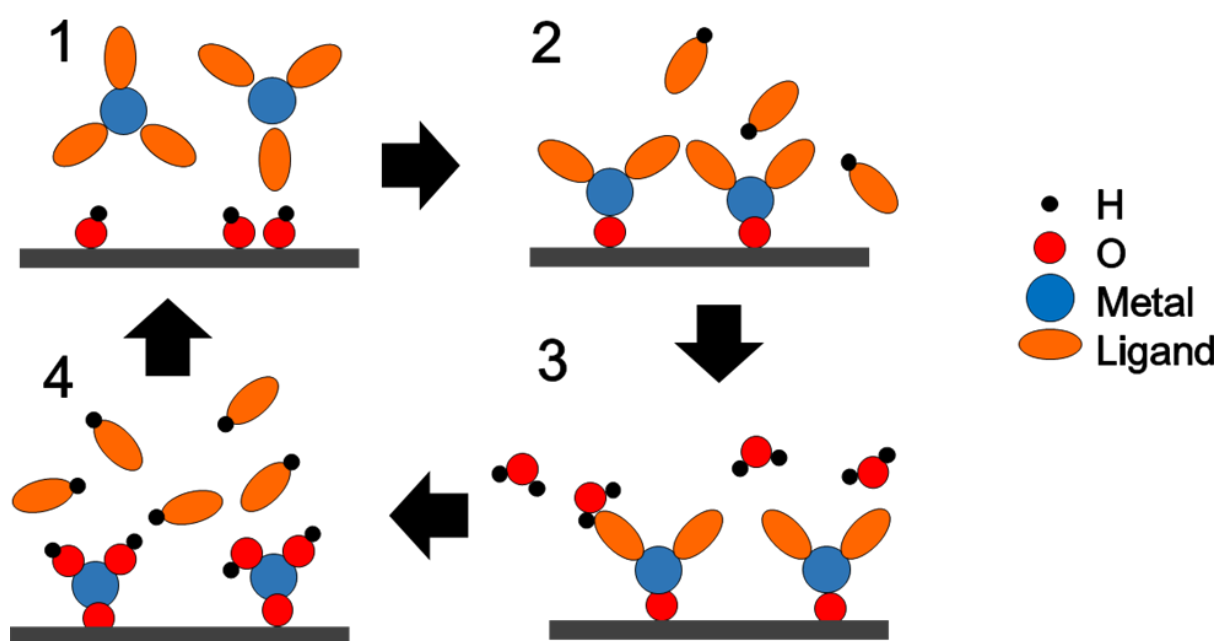
Figure 1.3 A general schematic of an ALD cycle

self-limiting reactions.[65] As shown in Figure 1.3, the first step in ALD involves reaction of a metal precursor with reactive surface sites on the substrate. The reaction self-terminates once all the reactive sites on substrate surface are consumed. Reaction by-products and residue unreacted precursor are purged out. Once this purge is complete, a second precursor is introduced and allowed to react with reactive sites left from the first layer of metal precursor. After completion of the reaction, another purge of by-products and leftover precursors completes an ALD cycle. The reactions can be performed sequentially to obtain a layer with desired thickness. ALD coatings are of superior quality, but there are potential challenges in cost-saving and scaling-up.[25]

Aside from metal oxides, cathode coatings of metal phosphates,[59] fluorides,[66] and lithiated transition metal oxides[67] have also been demonstrated before.

1.4.2 Polymeric Coatings

Conductive polymer is another group of candidates for cathode coatings. The polymer not only can act as a protective barrier between cathode and electrolyte but also can serve as a conductive binder that functions without additional conductivity enhancer (e.g. carbon black). Attachment of the polymer can proceed through direct mixing with the cathode particles,[68] *in situ* oxidation of monomers,[69] and elecochemical polymerization.[70] Poly(3,4-ethylenedioxythiophene) (PEDOT)-coated cathode delivers more stable cycling characteristics than uncoated material owning to the reduced metal dissolution and reduced interfacial impedance.[67-68, 71] Poly(ethylene glycol) has been used in conjunction to enhance ionic conductivity of the coating layer[68]. Polypyrrole with relatively low polymerization potential has been demonstrated as an *in situ*-polymerized coating.[70]

The tunable chemistry of polymer provides rich possibilities through molecular design and polymer combinations. Research on artifacial SEI (on anode) demonstrates the excellent performance with binary blend of polyethyleneglycol tert-octylphenyl ether (PEGPE) and polyallylamine (PAAm) as well as ternay blend of poly (diallydimethyl ammoniumchloride) (PDDA), poly (sodium4-styrenesulfonate) (PSS), and poly (vinyl alchohol) (PVA).[72]

1.4.3 Carbon Coatings

The carbon coating refers to a shell of conductive, graphitized material. The most successful example is carbon-coated $LiFePO_4$. Due to intrinsic low conductivity, the $LiFePO_4$ cathode need to be nano-sized and coated with conductive material to deliver reasonable rate performance.[73-74] Carbon coatings are usually produced from the pyrolysis of precursors such as sucrose[75], glucose[76], block copolymers[77] and ionic liquid.[78] The precursors can be loaded wet[79-80] or dry[81-82]. The produced carbon coatings are normally nanometers-thick.[74, 77, 81-82] The variation in thickness mostly corresponds to the choice of precursor and synthesis conditions (temperature, way of loading, etc.). It is not clear whether fine thickness control is achievable with the current methods. The carbon-coated $LiFePO_4$ has significatnly improved rate performance.[73-82] Electrolyte stability at the cathode-electrolyte interface is not the focus of these studies, possibly due to the intrinsic low reactivity of a low-voltage cathode.

There exists some reports on carbon coatings on high-voltage cathodes. Similar to the case of $LiFePO_4$, carbon coatings on NMC[83-84] and $LiCoO_2$[85] benefacially affects rate performance and improves discharge capacity, but it is not clear whether the carbon coatings can improve capacity retention.[83]

1.5 Scope of This Thesis

This thesis focuses on high-voltage NMC cathode and means to improve its cycle performance through engineering of the cathode-electrolyte interface. Knowledge of cathode-fading process and effective coating strategies is built upon anlytical study of electrochemical processes at the NMC-electrolyte interface and property-performance evaluation of multiple organic and inorganic coating candidates.

Chaper 2 investigates the composition and formation mechanism of CEI layer on NMC cathodes via a novel combination of quantitative correlation analysis of X-ray photoelectron spectra and binder-free cathode formulation. By comparing the CEI formation in NMC-based cells with lithium, graphite and lithium titanate anodes, we demonstrate unpredented experimental evidence for a CEI formation pathway via the migration of anode-originated surface species. Case study of Al_2O_3-coated cathodes further demonstrates that anode-to-cathode migration could be mitigated by cathode coatings. Overall,

this chapter highlights the importance of anode-mediated processes in order to correctly interpret surface phenomenon on the cathode side and to guide further development of surface protection strategies.

Chapter 3 examines silylation treatment of NMC cathode, and investigates the surface coverage-performance correlation by XPS, thermal mass spectrometry, XRD and impedance spectroscopy. Silylated cathodes synthesized under different reaction conditions demonstrate up to 27% higher capacity and 67% slower capacity decay over the course of 100 cycles. Analytical investigation suggests that the Si-containing coatings promote the charge-transfer between cathode and electrolyte, even when applied at low surface coverage that possesses no surface stabilization effect. As the surface coverage increases, performance is further improved due to the stabilization of cathode-electrolyte interface in addition to improved charge-transfer. The dual benefits of Si-containing coatings provide unique opportunities to improve cathode properties with small, non-crosslinking organic molecules.

Chapter 4 presents an opto-electrochemical cell design for *in situ* Raman mapping of Li ion battery materials. The cell parameters are carefully controlled to ensure uniform electric field distribution within the electrode film. Local state-of-charge profiles of NMC particles illustrate the intrinsic inhomogeneity in lithium intercalation process, and the correltion with battery failture is discussed.

Chapter 5 concludes the thesis with a summary as well as outlook for potential future directions.

1.6 Reference

1.   Huggins, R. A., *Advanced batteries : materials science aspects*. New York ; London : Springer, 2009.: 2009.

2.   Scrosati, B., *Lithium batteries advanced technologies and applications*. Hoboken : Wiley, 2013.: 2013.

3.   Xu, K., Nonaqueous liquid electrolytes for lithium-based rechargeable batteries. *Chem. Rev.* **2004,** *104* (10), 4303-4417.

4.   Mizushima, K.; Jones, P. C.; Wiseman, P. J.; Goodenough, J. B., LixCoO$_2$ (0<x<-1): A new cathode material for batteries of high energy density. *Mater. Res. Bull.* **1980,** *15* (6), 783-789.

5.   Goodenough, J. B.; Park, K. S., The Li-Ion Rechargeable Battery: A Perspective. *Journal of the American Chemical Society* **2013,** *135* (4), 1167-1176.

6.   T. Nagaura, K. T., *Prog. Batteries Solar Cells* **1990,** *9*, 209.

7.   Winter, M.; Brodd, R. J., What are batteries, fuel cells, and supercapacitors? *Chem. Rev.* **2004,** *104* (10), 4245-4269.

8.   Tarascon, J. M.; Armand, M., Issues and challenges facing rechargeable lithium batteries. *Nature* **2001,** *414* (6861), 359-367.

9.   Goodenough, J. B.; Kim, Y., Challenges for Rechargeable Li Batteries. *Chemistry of Materials* **2010,** *22* (3), 587-603.

10.   Aurbach, D., Review of selected electrode-solution interactions which determine the performance of Li and Li ion batteries. *Journal of Power Sources* **2000,** *89* (2), 206-218.

11.   Aurbach, D.; Eineli, Y., The Study of Li-Graphite Intercalation Processes in Several Electrolyte Systems Using *In Situ* X-Ray Diffraction. *Journal of the Electrochemical Society* **1995,** *142* (6), 1746-1752.

12.   Aurbach, D.; Eineli, Y.; Markovsky, B.; Zaban, A.; Luski, S.; Carmeli, Y.; Yamin, H., The Study of Electrolyte-Solutions Based on Ethylene and Dimethyl Carbonates for Rechargable Batteries. 2. Graphite-Electrodes *Journal of the Electrochemical Society* **1995,** *142* (9), 2882-2890.

13.   Peled, E., The electrochemical-behavior of alkali and alkaline-earth metals in non-aqueous battery systems - the solid electrolyte interphase model. *Journal of the Electrochemical Society* **1979,** *126* (12), 2047-2051.

14.   Dahn, J. R.; Sleigh, A. K.; Shi, H.; Way, B. M.; Weydanz, W. J.; Reimers, J. N.; Zhong, Q.; Sacken, U. v.; Pistoia, G., Lithium Batteries, New Materials, Developments and Perspectives. **1994**, Chapter 1.

15.   Aurbach, D.; Zaban, A.; Gofer, Y.; Ely, Y. E.; Weissman, I.; Chusid, O.; Abramson, O., Recent studies of the lithium-liquid electrolyte interface Electrochemical, morphological and spectral studies of a few important systems. *Journal of Power Sources* **1995,** *54* (1), 76-84.

16.   Aurbach, D.; Zaban, A.; Ein-Eli, Y.; Weissman, I.; Chusid, O.; Markovsky, B.; Levi, M.; Levi, E.; Schechter, A.; Granot, E., Recent studies on the correlation between surface chemistry, morphology, three-dimensional structures and performance of Li and Li-C intercalation anodes in several important electrolyte systems. *Journal of Power Sources* **1997,** *68* (1), 91-98.

17.   Aurbach, D.; Levi, M.; Levi, E.; Schechter, A., Failure and stabilization mechanisms of graphite electrodes. *JOURNAL OF PHYSICAL CHEMISTRY B* **1997,** *101* (12), 2195-2206.

18.   Aurbach, D.; Markovsky, B.; Levi, M. D.; Levi, E.; Schechter, A.; Moshkovich, M.; Cohen, Y., New insights into the interactions between electrode materials and electrolyte solutions for advanced nonaqueous batteries. *Journal of Power Sources* **1999,** *81*, 95-111.

19.   Schechter, A.; Aurbach, D.; Cohen, H., X-ray photoelectron spectroscopy study of surface films formed on Li electrodes freshly prepared in alkyl carbonate solutions. *Langmuir* **1999,** *15* (9), 3334-3342.

20.   Aurbach, D.; Markovsky, B.; Weissman, I.; Levi, E.; Ein-Eli, Y., On the correlation between surface chemistry and performance of graphite negative electrodes for Li ion batteries. *ELECTROCHIMICA ACTA* **1999,** *45* (1-2), 67-86.

21.   Ein-Eli, Y., A new perspective on the formation and structure of the solid electrolyte interface at the graphite anode of Li-ion cells. *Electrochemical and Solid State Letters* **1999,** *2* (5), 212-214.

22.   Edstrom, K.; Gustafsson, T.; Thomas, J. O., The cathode-electrolyte interface in the Li-ion battery. *Electrochimica Acta* **2004,** *50* (2-3), 397-403.

23.   Aurbach, D.; Gamolsky, K.; Markovsky, B.; Salitra, G.; Gofer, Y.; Heider, U.; Oesten, R.; Schmidt, M., The study of surface phenomena related to electrochemical lithium intercalation into LixMOy host materials (M = Ni, Mn). *Journal of the Electrochemical Society* **2000,** *147* (4), 1322-1331.

24.   Niehoff, P.; Winter, M., Composition and Growth Behavior of the Surface and Electrolyte Decomposition Layer of/on a Commercial Lithium Ion Battery $Li_xNi_{1/3}Mn_{1/3}Co_{1/3}O_2$ Cathode Determined by Sputter Depth Profile X-ray Photoelectron Spectroscopy. *Langmuir* **2013,** *29* (51), 15813-15821.

25.   Hayner, C. M.; Zhao, X.; Kung, H. H., Materials for Rechargeable Lithium-Ion Batteries. In *Annual Review of Chemical and Biomolecular Engineering, Vol 3*, Prausnitz, J. M., Ed. Annual Reviews: Palo Alto, 2012; Vol. 3, pp 445-471.

26.   Padhi, A. K.; Nanjundaswamy, K. S.; Goodenough, J. B., Phospho-olivines as positive-electrode materials for rechargeable lithium batteries. *Journal of the Electrochemical Society* **1997,** *144* (4), 1188-1194.

27.   Makimura, Y.; Ohzuku, T., Lithium insertion material of $LiNi_{1/2}Mn_{1/2}O_2$ for advanced lithium-ion batteries. *Journal of Power Sources* **2003,** *119*, 156-160.

28.   Ohzuku, T.; Makimura, Y., Layered lithium insertion material of $LiCo_{1/3}Ni_{1/3}Mn_{1/3}O_2$ for lithium-ion batteries. *Chemistry Letters* **2001,** (7), 642-643.

29.   Thackeray, M. M.; David, W. I. F.; Bruce, P. G.; Goodenough, J. B., LITHIUM INSERTION INTO MANGANESE SPINELS. *Mater. Res. Bull.* **1983,** *18* (4), 461-472.

30.   Ohzuku, T.; Kitagawa, M.; Hirai, T., Electrochemistry of Manganese Dioxide in Lithium Nonaqueous Cell III . X-Ray Diffractional Study on the Reduction of Spinel-Related Manganese Dioxide. *Journal of the Electrochemical Society* **1990,** *137* (3), 769-775.

31.   Tarascon, J. M.; Wang, E.; Shokoohi, F. K.; McKinnon, W. R.; Colson, S., The Spinel Phase of $LiMN_2O_4$ as a Cathode in Secondary Lithium Cells. *Journal of the Electrochemical Society* **1991,** *138* (10), 2859-2864.

32.   Thackeray, M. M.; Kang, S. H.; Johnson, C. S.; Vaughey, J. T.; Benedek, R.; Hackney, S. A., Li_2MnO_3-stabilized $LiMO_2$ (M = Mn, Ni, Co) electrodes for lithium-ion batteries. *Journal of Materials Chemistry* **2007,** *17* (30), 3112-3125.

33.   Bettge, M.; Li, Y.; Gallagher, K.; Zhu, Y.; Wu, Q. L.; Lu, W. Q.; Bloom, I.; Abraham, D. P., Voltage Fade of Layered Oxides: Its Measurement and Impact on Energy Density. *Journal of the Electrochemical Society* **2013,** *160* (11), A2046-A2055.

34.   Rozier, P.; Tarascon, J. M., Review-Li-Rich Layered Oxide Cathodes for Next-Generation Li-Ion Batteries: Chances and Challenges. *Journal of the Electrochemical Society* **2015,** *162* (14), A2490-A2499.

35.   Hwang, B. J.; Tsai, Y. W.; Carlier, D.; Ceder, G., A combined computational/experimental study on $LiNi_{1/3}Co_{1/3}Mn_{1/3}O_2$. *Chemistry of Materials* **2003,** *15* (19), 3676-3682.

36.   Kim, J. M.; Chung, H. T., The first cycle characteristics of Li $Ni_{1/3}Co_{1/3}Mn_{1/3}O_2$ charged up to 4.7 V. *Electrochimica Acta* **2004,** *49* (6), 937-944.

37.   Wu, Y.; Murugan, A. V.; Manthiram, A., Surface modification of high capacity layered Li Li$_{0.2}$Mn$_{0.54}$Ni$_{0.13}$Co$_{0.13}$O$_2$ cathodes by AlPO$_4$. *Journal of the Electrochemical Society* **2008,** *155* (9), A635-A641.

38.   Shaju, K. M.; Rao, G. V. S.; Chowdari, B. V. R., Influence of Li-ion kinetics in the cathodic performance of layered Li(Ni$_{1/3}$Co$_{1/3}$Mn$_{1/3}$)O$_2$. *Journal of the Electrochemical Society* **2004,** *151* (9), A1324-A1332.

39.   Choi, J.; Manthiram, A., Investigation of the irreversible capacity loss in the layered LiNi$_{1/3}$Mn$_{1/3}$Co$_{1/3}$O$_2$ cathodes. *Electrochemical and Solid State Letters* **2005,** *8* (8), C102-C105.

40.   Wang, J.; Yao, X. Y.; Zhou, X. F.; Liu, Z. P., Synthesis and electrochemical properties of layered lithium transition metal oxides. *Journal of Materials Chemistry* **2011,** *21* (8), 2544-2549.

41.   Dolotko, O.; Senyshyn, A.; Muhlbauer, M. J.; Nikolowski, K.; Ehrenberg, H., Understanding structural changes in NMC Li-ion cells by in situ neutron diffraction. *Journal of Power Sources* **2014,** *255*, 197-203.

42.   Jiang, J.; Buhrmester, T.; Eberman, K. W.; Krause, L. J.; Dahn, J. R., Electrochemical and thermal comparisons of Li Ni$_{0.1}$Co$_{0.8}$Mn$_{0.1}$O$_2$ synthesized at different temperatures (900, 1000, and 1100 degrees C). *Journal of the Electrochemical Society* **2005,** *152* (1), A19-A22.

43.   MacNeil, D. D.; Lu, Z.; Dahn, J. R., Structure and electrochemistry of Li Ni$_x$Co$_{1-2x}$Mn$_x$O$_2$ (0 <= x <= 1/2). *Journal of the Electrochemical Society* **2002,** *149* (10), A1332-A1336.

44.   Lu, Z. H.; MacNeil, D. D.; Dahn, J. R., Layered cathode materials Li Ni$_x$Li$_{1/3-2x/3}$Mn$_{2/3-x/3}$O$_2$ for lithium-ion batteries. *Electrochemical and Solid State Letters* **2001,** *4* (11), A191-A194.

45.   Lu, C. H.; Shen, B. J., Electrochemical characteristics of LiNi$_{1/3}$Co$_{1/3}$Mn$_{1/3}$O$_2$ powders prepared from microwave-hydrothermally derived precursors. *Journal of Alloys and Compounds* **2010,** *497* (1-2), 159-165.

46.   Kim, T.-H.; Park, J.-S.; Chang, S. K.; Choi, S.; Ryu, J. H.; Song, H.-K., The Current Move of Lithium Ion Batteries Towards the Next Phase. *Advanced Energy Materials* **2012,** *2* (7), 860-872.

47.   Pillot, C., Battery market development for consumer electronics, automotive, and industrial: materials requirements and trends. *5th Israeli Power Sources Conference 2015* **2015**.

48.   Hausbrand, R.; Cherkashinin, G.; Ehrenberg, H.; Groting, M.; Albe, K.; Hess, C.; Jaegermann, W., Fundamental degradation mechanisms of layered oxide Li-ion battery cathode materials: Methodology, insights and novel approaches. *Mater. Sci. Eng. B-Adv. Funct. Solid-State Mater.* **2015,** *192*, 3-25.

49.   Li, C.; Zhang, H. P.; Fu, L. J.; Liu, H.; Wu, Y. P.; Ram, E.; Holze, R.; Wu, H. Q., Cathode materials modified by surface coating for lithium ion batteries. *Electrochimica Acta* **2006,** *51* (19), 3872-3883.

50.   Wu, Y.; Manthiram, A., Effect of surface modifications on the layered solid solution cathodes (1-z) Li Li$_{1/3}$Mn$_{2/3}$ O$_2$-(z) Li Mn$_{0.5y}$Ni$_{0.5y}$Co$_{2y}$ O$_2$. *Solid State Ionics* **2009,** *180* (1), 50-56.

51.   Kim, Y. J.; Kim, H.; Kim, B.; Ahn, D.; Lee, J. G.; Kim, T. J.; Son, D.; Cho, J.; Kim, Y. W.; Park, B., Electrochemical stability of thin-film LiCoO$_2$ cathodes by aluminum-oxide coating. *Chemistry of Materials* **2003,** *15* (7), 1505-1511.

52.   Su, Y. T.; Cui, S. H.; Zhuo, Z. Q.; Yang, W. L.; Wang, X. W.; Pan, F., Enhancing the High-Voltage Cycling Performance of $LiNi_{0.5}Mn_{0.3}Co_{0.2}O_2$ by Retarding Its Interfacial Reaction with an Electrolyte by Atomic-Layer-Deposited Al_2O_3. *ACS Appl. Mater. Interfaces* **2015,** *7* (45), 25105-25112.

53.   Myung, S. T.; Izumi, K.; Komaba, S.; Sun, Y. K.; Yashiro, H.; Kumagai, N., Role of alumina coating on Li-Ni-Co-Mn-O particles as positive electrode material for lithium-ion batteries. *Chemistry of Materials* **2005,** *17* (14), 3695-3704.

54.   Shen, D. D.; Zhang, D. W.; Wen, J. W.; Chen, D. M.; He, X. J.; Yao, Y. J.; Li, X. L.; Duger, C., $LiNi_{1/3}Co_{1/3}Mn_{1/3}O_2$ coated by Al_2O_3 from urea homogeneous precipitation method: improved Li storage performance and mechanism exploring. *Journal of Solid State Electrochemistry* **2015,** *19* (5), 1523-1533.

55.   Kim, C. A.; Choi, H. J.; Lee, J. H.; Yoo, S. Y.; Kim, J. W.; Shim, J. H.; Kang, B., Influence of surface modification on electrochemical performance of high voltage spinel ordered-$LiNi_{0.5}Mn_{1.5}O_4$ exposed to 5.3 V for 100 h before and after surface modification with ALD method. *Electrochimica Acta* **2015,** *184*, 134-142.

56.   Verdier, S.; El Ouatani, L.; Dedryvere, R.; Bonhomme, F.; Biensan, P.; Gonbeau, D., XPS study on Al_2O_3- and $AlPO_4$-coated $LiCoO_2$ cathode material for high-capacity li ion batteries. *Journal of the Electrochemical Society* **2007,** *154* (12), A1088-A1099.

57.   Jung, Y. S.; Lu, P.; Cavanagh, A. S.; Ban, C.; Kim, G.-H.; Lee, S.-H.; George, S. M.; Harris, S. J.; Dillon, A. C., Unexpected Improved Performance of ALD Coated $LiCoO_2$/Graphite Li-Ion Batteries. *Advanced Energy Materials* **2013,** *3* (2), 213-219.

58.   Kim, J. W.; Kim, D. H.; Oh, D. Y.; Lee, H.; Kim, J. H.; Lee, J. H.; Jung, Y. S., Surface chemistry of $LiNi_{0.5}Mn_{1.5}O_4$ particles coated by Al_2O_3 using atomic layer deposition for lithium-ion batteries. *Journal of Power Sources* **2015,** *274*, 1254-1262.

59.   Cho, J., Dependence of $AlPO_4$ coating thickness on overcharge behaviour of $LiCoO_2$ cathode material at 1 and 2C rates. *Journal of Power Sources* **2004,** *126* (1-2), 186-189.

60.   Zhao, H. L.; Ling, G.; Qiu, W. H.; Zhang, X. H., Improvement of electrochemical stability of $LiCoO_2$ cathode by a nano-crystalline coating. *Journal of Power Sources* **2004,** *132* (1-2), 195-200.

61.   Kim, J.; Noh, M.; Cho, J.; Kim, H.; Kim, K. B., Controlled nanoparticle metal phosphates (metal = Al, Fe, Ce, and Sr) coatings on $LiCoO_2$ cathode materials. *Journal of the Electrochemical Society* **2005,** *152* (6), A1142-A1148.

62.   Sun, Y. K.; Hong, K. J.; Prakash, J.; Amine, K., Electrochemical performance of nano-sized ZnO-coated $LiNi_{0.5}Mn_{1.5}O_4$ spinel as 5 V materials at elevated temperatures. *Electrochemistry Communications* **2002,** *4* (4), 344-348.

63.   Fu, L. J.; Liu, H.; Li, C.; Wu, Y. P.; Rahm, E.; Holze, R.; Wu, H. Q., Surface modifications of electrode materials for lithium ion batteries. *Solid State Sci. (France)* **2006,** *8* (2), 113-128.

64.   Jung, Y. S.; Cavanagh, A. S.; Riley, L. A.; Kang, S. H.; Dillon, A. C.; Groner, M. D.; George, S. M.; Lee, S. H., Ultrathin Direct Atomic Layer Deposition on Composite Electrodes for Highly Durable and Safe Li-Ion Batteries. *Advanced Materials* **2010,** *22* (19), 2172-2176.

65.   George, S. M.; Ott, A. W.; Klaus, J. W., Surface chemistry for atomic layer growth. *J. Phys. Chem.* **1996,** *100* (31), 13121-13131.

66.   Ylilammi, M.; Rantaaho, T., Metal Fluoride Thin Films Prepared by Atomic Layer Deposition. *Journal of the Electrochemical Society* **1994,** *141* (5), 1278-1284.

67.   Kannan, A. M.; Manthiram, A., Surface/Chemically Modified $LiMn_2O_4$ cathodes for lithium-ion batteries. *Electrochemical and Solid State Letters* **2002,** *5* (7), A167-A169.

68.   Ju, S. H.; Kang, I. S.; Lee, Y. S.; Shin, W. K.; Kim, S.; Shin, K.; Kim, D. W., Improvement of the Cycling Performance of $LiNi_{0.6}Co_{0.2}Mn_{0.2}O_2$ Cathode Active Materials by a Dual-Conductive Polymer Coating. *ACS Appl. Mater. Interfaces* **2014,** *6* (4), 2546-2552.

69.   Nishizawa, M.; Mukai, K.; Kuwabata, S.; Martin, C. R.; Yoneyama, H., Template Synthesis of Polypyrrole-Coated Spinel $LiMn_2O_4$ Nanotubules and Their Properties as Cathode Active Materials for Lithium Batteries. *Journal of The Electrochemical Society* **1997,** *144* (6), 1923-1927.

70.   Boyano, I.; Blazquez, J. A.; de Meatza, I.; Bengoechea, M.; Miguel, O.; Grande, H.; Huang, Y. H.; Goodenough, J. B., Preparation of C-LiFePO4/polypyrrole lithium rechargeable cathode by consecutive potential steps electrodeposition. *Journal of Power Sources* **2010,** *195* (16), 5351-5359.

71.   Arbizzani, C.; Balducci, A.; Mastragostino, M.; Rossi, M.; Soavi, F., $Li_{1.01}Mn_{1.97}O_4$ surface modification by poly (3,4-ethylenedioxythiophene). *Journal of Power Sources* **2003,** *119*, 695-700.

72.   Wu, N. L.; Weng, Y. T.; Li, F. S.; Yang, N. H.; Kuo, C. L.; Li, D. S., Polymeric artificial solid/electrolyte interphases for Li-ion batteries. *Prog. Nat. Sci.* **2015,** *25* (6), 563-571.

73.   Nien, Y. H.; Carey, J. R.; Chen, J. S., Physical and electrochemical properties of LiFePO4/C composite cathode prepared from various polymer-containing precursors. *Journal of Power Sources* **2009,** *193* (2), 822-827.

74.   Wang, Y. G.; He, P.; Zhou, H. S., Olivine LiFePO4: development and future. *Energy Environ. Sci.* **2011,** *4* (3), 805-817.

75.   Wang, Y. G.; Wang, Y. R.; Hosono, E. J.; Wang, K. X.; Zhou, H. S., The design of a LiFePO4/carbon nanocomposite with a core-shell structure and its synthesis by an *in situ* polymerization restriction method. *Angew. Chem.-Int. Edit.* **2008,** *47* (39), 7461-7465.

76.   Sun, X.; Li, Y., Colloidal Carbon Spheres and Their Core/Shell Structures with Noble-Metal Nanoparticles. *Angewandte Chemie International Edition* **2004,** *43* (5), 597-601.

77.   Wu, X. L.; Jiang, L. Y.; Cao, F. F.; Guo, Y. G.; Wan, L. J., LiFePO4 Nanoparticles Embedded in a Nanoporous Carbon Matrix: Superior Cathode Material for Electrochemical Energy-Storage Devices. *Advanced Materials* **2009,** *21* (25-26), 2710-2714.

78.   Li, C. L.; Gu, L.; Tong, J. W.; Maier, J., Carbon Nanotube Wiring of Electrodes for High-Rate Lithium Batteries Using an Imidazolium-Based Ionic Liquid Precursor as Dispersant and Binder: A Case Study on Iron Fluoride Nanoparticles. *ACS Nano* **2011,** *5* (4), 2930-2938.

79.   Wilcox, J. D.; Doeff, M. M.; Marcinek, M.; Kostecki, R., Factors influencing the quality of carbon coatings on LiFePO4. *Journal of the Electrochemical Society* **2007,** *154* (5), A389-A395.

80.   Oh, S. W.; Myung, S. T.; Oh, S. M.; Oh, K. H.; Amine, K.; Scrosati, B.; Sun, Y. K., Double Carbon Coating of LiFePO4 as High Rate Electrode for Rechargeable Lithium Batteries. *Advanced Materials* **2010,** *22* (43), 4842-4845.

81.   Zhi, X. K.; Liang, G. C.; Wang, L.; Ou, X. Q.; Gao, L. M.; Jie, X. F., Optimization of carbon coatings on LiFePO$_4$: Carbonization temperature and carbon content. *Journal of Alloys and Compounds* **2010,** *503* (2), 370-374.

82.   Cho, Y. D.; Fey, G. T. K.; Kao, H. M., The effect of carbon coating thickness on the capacity of LiFePO$_4$/C composite cathodes. *Journal of Power Sources* **2009,** *189* (1), 256-262.

83.   Kim, H. S.; Kong, M.; Kim, K.; Kim, I. J.; Gu, H. B., Effect of carbon coating on LiNi$_{1/3}$Mn$_{1/3}$Co$_{1/3}$O$_2$ cathode material for lithium secondary batteries. *Journal of Power Sources* **2007,** *171* (2), 917-921.

84.   Hashem, A. M. A.; Abdel-Ghany, A. E.; Eid, A. E.; Trottier, J.; Zaghib, K.; Mauger, A.; Julien, C. M., Study of the surface modification of LiNi$_{1/3}$Co$_{1/3}$Mn$_{1/3}$O$_2$ cathode material for lithium ion battery. *Journal of Power Sources* **2011,** *196* (20), 8632-8637.

85.   Cao, Q.; Zhang, H. P.; Wang, G. J.; Xia, Q.; Wu, Y. P.; Wu, H. Q., A novel carbon-coated LiCoO$_2$ as cathode material for lithium ion battery. *Electrochemistry Communications* **2007,** *9* (5), 1228-1232.

Chapter 2

Anode-originated SEI Migration for Formation of Cathode-Electrolyte Interphase

Reprinted with permission from Fang, S., Jackson, D., Dreibelbis, M., Kuech, T., Hamers, R. J.,

Anode-originated SEI Migration for Formation of Cathode-Electrolyte Interphase, submitted to

Journal of Electrochemical Society

2.1   Introduction

The increasing demand for portable electronic devices, electric vehicles, and grid energy storage

motivates the continuous development of Li-ion batteries with reduced cost and improved performance.

In recent years, there has been high interest in the layered $LiNi_xMn_yCo_{1-x-y}O_2$ (NMC) cathode material

due to its higher capacity, lower cost, and enhanced safety compared to the conventional $LiCoO_2$

cathode.[1-10] The NMC material, however, experiences a relatively large irreversible capacity loss during

the first cycle and poor cycle performance, especially at high upper cutoff voltages and at high

temperature.[3-4, 11-12] It is believed that electrolyte decomposition at the electrode-electrolyte interface

accelerates capacity loss over extended cycling.[13] The term cathode-electrolyte interphase (CEI) is

typically used to describe the cathode-side surface layer that is composed of solid-phase electrolyte

decomposition products, while solid-electrolyte interphase (SEI) refers to what forms on the anode side.

The formation of CEI and SEI depletes accessible lithium in the battery and impedes lithium transport

at the electrode-electrolyte interface.[14] Among the efforts to improve NMC cycle life, one is to modify

the cathode surface by coating with thin metal oxides such as alumina[15-18] to reduce irreversible capacity

loss and prevent parasitic reactions on the surface.[15-24] In order to understand the working mechanism

of coatings, it is highly desirable to systematically study the effect of coatings on interfacial

phenomenon such as CEI formation.

CEI formation is generally discussed as an isolated process in terms of cathode-specific electrolyte

decomposition. However, a small number of studies have proposed that there is crosstalk between the reactions occurring at the cathode and anode side in battery systems. Aurbach et al.[14] first described the possibility of reduction products on the anode saturating the electrolyte and re-precipitating on the cathode. Jarry et al. have reported transition metal ion dissolution from the cathode side and migration to the anode surface[21] via shuttling in the form of ligand-metal-complexes.[25] To the best of our knowledge, no literature study has been designed to experimentally validate the migration pathway for anode-mediated CEI formation. For correct conceptualization of CEI formation and correct interpretation of CEI-related phenomenon such as the effect of cathode coatings, it is essential to understanding the potential role of anode-to-cathode SEI migration.

Previous literature has reported the use of X-ray photoelectron spectroscopy (XPS) to identify CEI composition and quantities.[23, 26-28] XPS is a surface-sensitive technique with photoelectron escape depth on the order of a few nanometers, suitable of surface analysis. One challenge of XPS quantification of CEI is to differentiate CEI component in the presence of polyvinylidene difluoride (PVDF) binder, conductive carbon black and other CEI species. For example, in the C 1s region, C-O containing CEI gives rise to peaks between 286.5-287.0 eV, very close to PVDF binder signal at 286.45 eV[23]. The attempts taken to differentiate CEI signal from PVDF vary between studies. Niehoff et al. fit two peaks near 286 eV to represent CF_2 and CH_2 from PVDF and optimized their area to match PVDF stoichiometry.[28] Cherkashinin et al. fit one peak in the 286 eV region and assigned it to PVDF/C=O/C-O mixture.[26] In previous studies, it has been common to assign one broad XPS peak to multiple species due to the lack of clear differentiation among possible carbon-containing species.[23, 26-28] To bring more clarity into CEI assignation, we note the necessity of exploring alternative ways to assign the chemical formulation of CEI.

Presented here is a systematic XPS study of CEI formation pathway on NMC cathodes. The first section focuses on establishing a more definitive identification of CEI species via quantitative correlation analysis and use of a binder-free cathode formulation. The identity and approximate stoichiometry of CEI species were determined both by correlating the changes in elemental content of C, O, Li, F and P at the surface, and by investigating cathode surface species at the absence of PVDF binder. In the second section, we address the theory of anode-mediated CEI formation via SEI migration to the cathode. Two sets of experiments were designed: the first one compared CEI formation in cells constructed with one and three separators, and the increased number of separators were used to increase the cathode-anode physical separation and thereby impede migration between the two electrodes; the second set of experiments compared CEI formation in NMC-Graphite and NMC-Lithium Titanate (LTO) full cells, and the different types of anodes were used to demonstrate dependence of CEI quantities on the SEI formation process. LTO is generally considered SEI-free because its lithiation potential is higher than most electrolyte materials.[29-34] Finally, we discuss the impact of the SEI migration theory on our interpretation of coating functions. Comparative CEI study was conducted on regular NMC cathodes and on cathodes with thin Al_2O_3 coatings produced by atomic layer deposition (ALD).

2.2 Experiment

Fabrication of NMC cathodes. The $LiNi_{0.5}Mn_{0.3}Co_{0.2}O_2$ (NMC532) powder under investigation was supplied by TODA Inc.. The composite NMC electrodes were prepared by mixing the active cathode powder (92% w/w), carbon black (3.5% w/w, Super P C65) and 4.5% of polyvinylidene fluoride (Solef PVDF) binder in N-methylpyrrolidone (NMP) solvent. The mixture was cast on Al foil with a 150 μm doctor blade. The film was dried under vacuum, Carver hydraulic lab press at 3 ton/cm^2, and dried again under vacuum at 150°C overnight before use.

Fabrication of binder-free cathodes. The binder-free electrodes were prepared by mixing the NMC (95% w/w) and carbon black (5%) with NMP solvent. The slurry was cast on Al foil with 50nm doctor blade. The film was dried at 150°C under vacuum overnight.

Half-cell characterization. The half-cells were made from the fabricated NMC cathodes and lithium anodes (Chemetall Foot Corp). The electrolyte was 1M $LiPF_6$ in EC/DEC (1:1 vol%), obtained from UBE Inc. The coin cells were cycled at constant current between 3V and 4.3V vs. Li on an Arbin battery testing unit. For samples cycled 1-4 times, the current was set to be C/10 (~0.23 mA). For long cycling, the first two formation cycles were at C/10, and the subsequent charge and discharge rates were C/3 (~0.8 mA) and 1C (~2.3 mA), respectively. The specific current value depends on the loading of each electrode. For *post mortem* analysis after cycling, the cell was disassembled and the cathode was soaked in fresh 2mL dimethyl carbonate (DMC) three times for 2 minutes each to remove excess salt and electrolyte.

Full-cell characterization. The full cells were made from matched NMC cathode and graphite or lithium titanate (LTO) anode films purchased from Electrodes and More. The electrolyte was 1M $LiPF_6$ in EC/DEC (1:1 vol%), obtained from BASF. The coin cells were cycled at constant current between 3-4.2V vs. graphite, and 1.6-2.8V vs. LTO. The C rates were the same as were used in coin half cells.

X-ray photoelectron spectroscopy. X-ray photoelectron spectroscopy (XPS) of half-cell cathodes was performed using a custom-built XPS system (Physical Electronics Inc., Eden Prairie, MN) consisting of a PHI 10- 610 K_α X-ray source (1486.6 eV photon energy) with a model 10-420 toroidal monochromator and a model 10-360 hemispherical analyzer with a 16-channel detector array. Electrons were collected at an emission angle of 45° from the surface normal. The survey spectra were collected at 186 eV pass energy from 0-1400 eV binding energy. High resolution spectra of the O (1s), P (2p), F

(1s), C (1s) and Li (1s) regions were collected with a 58.7 eV pass energy that yielded an analyzer

energy resolution of 0.88 eV.

XPS analysis of full-cell cathodes and anodes were performed on a Thermo K-Alpha XPS system.

Similarly, the survey spectra were collected at 186 eV pass energy from 0-1400 eV binding energy.

High-resolution spectra of the O (1s), P (2p), F (1s), C (1s) and Li (1s) regions were collected with a

58.7 eV pass energy.

In quantitative analysis, the raw spectra were normalized by a normalization factor (NF) to correct

for the variance in total electron flux due to different alignment and instrument conditions on different

days, and NF is equal to (sum of electron counts between 0-800 eV in the survey spectra $/10^5$).

Rationalization of this normalization procedure can be found in supplementary information Fig. A1.1

and Fig. A1.2.

Fabrication of Al_2O_3 coated NMC cathodes. Atomic layer deposition (ALD) on cathode powders

was carried out in a horizontal flow-tube quartz reactor ALD system heated by a tube furnace. All the

depositions were carried out at 200 °C, at a pressure of ~0.5 Torr. The NMC powder was held in an

aluminum tray and placed inside the heated zone of the reactor with no agitation applied to the powders

during deposition. Trimethylaluminum (TMA, Sigma-Aldrich, 97%) and deionized water (H_2O) were

used as precursors for Al and O, respectively, with nitrogen (N_2) used as purge gas. Powders were coated

with five cycles consisting of the pulse sequence: TMA – purge – H_2O – purge. Bubbler outlets were

connected to the carrier line through a metering valve which controls the precursor flow rate. A residual

gas analyzer (SRS RGA 200) mass spectrometer connected to the downstream end of the reactor was

used to monitor the reactor effluent before it exited the reactor into a roughing pump. The pulse times

and purge times of the precursors were selected based on the completion of a half-cycle surface reactions,

that is, the decrease in the RGA signal intensity. The Al_2O_3-coated powder was used to fabricate coated NMC electrodes.

2.3   Results

2.3.1   Identification of CEI Composition

2.3.1.1 CEI identification and elemental correlation on composite NMC cathodes

Fig. 2.1 shows the Li (1s), F (1s), C (1s) and O (1s) XPS spectra of NMC cathodes after cycling in coin half cells for 1 to 200 times. The reference sample refers to cathode taken out from a coin cell without electrochemical cycling. All samples were rinsed with DMC to remove electrolyte residue and other volatile species, and CEI layer was defined as what remained on the surface after rinsing.

In the F (1s) region (Fig. 2.1a), the 688 eV peak arises from the F atoms in the PVDF binder and/or in $LiP_mO_nF_p$ species originating from $LiPF_6$ decomposition,[23-24] and the shoulder peak at 685 eV arises from LiF and/or transition metal fluorides.[18, 23, 35-36] As the number of charge-discharge cycles increases, the intensity of the 688 eV PVDF peak decreases because the growth of CEI layer attenuates signals from the underlying bulk electrode containing binder. Fig. 2.1b shows XPS data for the Li(1s) region. The Li region is dominated by one peak at 54.5eV. Referring to previous literature, possible contributing species to the Li peak include LiF, Li_2CO_3, LiOH and the NMC cathode itself.[24] Fig. 2.1c shows the evolution of C (1s) spectra. The 284 eV signal arises from carbon black; the 291 eV peak is assigned to PVDF binder based on both literature reports[28] and our own observation of good quantitative correlation of the 291 eV C 1s peak with 688 eV F 1s peak from PVDF (discussed in detail later); the 287 eV peak is assigned to mixture of PVDF signal and signal from CEI species coming from carbonate electrolyte;[18, 23-24, 28] the 289 eV peak appearing after over 100 cycles is assigned Li_2CO_3.[23-24, 37] Fig. 2.1d shows the O (1s) region. The 529 eV peak is attributed to oxygen in bulk NMC[28]; the 533 peak has been reported

previously to come from a mixture of CEI species including $LiP_mO_nF_p$, $(Li)C_xH_yO_z$, and MO_xF_y (M= Co, Mn, Ni).[26, 28]

To remove some ambiguity in the peak assignment, we quantitatively correlated the emission intensities of different elemental peaks. This approach can shed light on which elemental peaks are positively correlated (indicating that they most likely come from the same CEI species or a group of CEI species that form simultaneously) or not correlated (indicating that the peaks come from different CEI species).

Three quantitative correlations were established upon careful examination of the F, C, O and Li peaks. Fig.2.2a demonstrates linear correlation of the 688 eV F(1s) peak with the integrated C (1s) peak at 291 eV. This correlation strongly supports the assignment of both peaks to PVDF binder. Even though CEI species such as $LiP_mO_nF_p$ are expected to arise at 688 eV, they form in such subtle quantities that they do not significantly impact the overall correlation. Fig. 2b depicts the correlation between the 54.5 eV Li(1s) peak and the 685 eV F(1s) peak. The Li(1s) and F(1s) intensities were normalized by their respective atomic sensitivity factors so that the slope gives the Li/F atomic ratio. The linear correlation with 0.95±0.17 Li/F atomic ratio demonstrates simultaneous formation of the detected Li-containing species at 53 eV and the F-containing species at 685 eV in 1:1 stoichiometry. The most likely interpretation of this result is that both peaks come from LiF which has 1:1 Li:F ratio. There remains a possibility that this correlation arises from stoichiometric mixture of LiX (Li_2CO_3, bulk NMC, etc.) and MF (M=Ni, Mn, Co, etc.). However, further examination disfavors the latter interpretation. If the Li signal comes majorly from species like Li_2CO_3 or $(Li)C_xH_yO_z$, we would reasonably expect to see Li-O or Li-C correlation, which in fact is lacking (shown in Fig. S3). The NMC can also give rise to a Li signal from the intercalated Li, but as shown by the dotted curve in Fig. 2.1b, pristine non-cycled NMC

electrode shows almost no identifiable lithium peak. The low intensity of Li from the (lithiated) NMC electrode is reasonable considering the relatively small sensitivity factor of Li in XPS (0.025 compared with 3.255 for Co 2p); the higher Li intensity in Fig. 2.2 strongly suggests that nearly all the observed Li arises from surface species. By ruling out the possibility of $LiCO_3$ or NMC giving rise to the 53 eV Li 1s signal, the attribution of Li-F correlation to mixture of LiX and metal fluoride is less favored. Therefore, we assign both the Li 53 eV and F 685 eV peaks to LiF and conclude that contribution from other species is insignificant and possibly buried in the error bar of the correlation plot. According to Fig 2.1, LiF forms as soon as NMC is put into contact with electrolyte. We have not seen significant growth of LiF over cycles. There are several possible explanations: (1) LiF forms early and the growth is self-terminating; (2) LiF grows but we cannot see a clear trend due to the error bar associated with the measurement; (3) Formed LiF dissolves, migrates, or transforms into other compounds, and new LiF continues to form to keep the stable total content. There is presently not enough information to assert which one is a more accurate description.

Fig. 2.2c demonstrates correlation between the total C and O emission intensity. The O(1s) signal was quantified by direct fitting of the peak at 532 eV. In the C(1s) region, there is a strong peak at 286 eV peak that arises from overlapping signals from the CH_2 group of PVDF and species from the CEI and decreases in intensity as the CEI grows. In order to isolate the contribution of the CEI layer, we note that PVDF consists of repeating ($-CH_2-CF_2-$) groups, and therefore should give rise to two equal-intensity C(1s) peaks at 286 eV (from the $-CH_2-$ groups) and at 291 eV (from the $-CF_2-$ groups). Since we can measure the 291 eV peak accurately, we can obtain the C-containing CEI using the following equation:

(a) F 1s

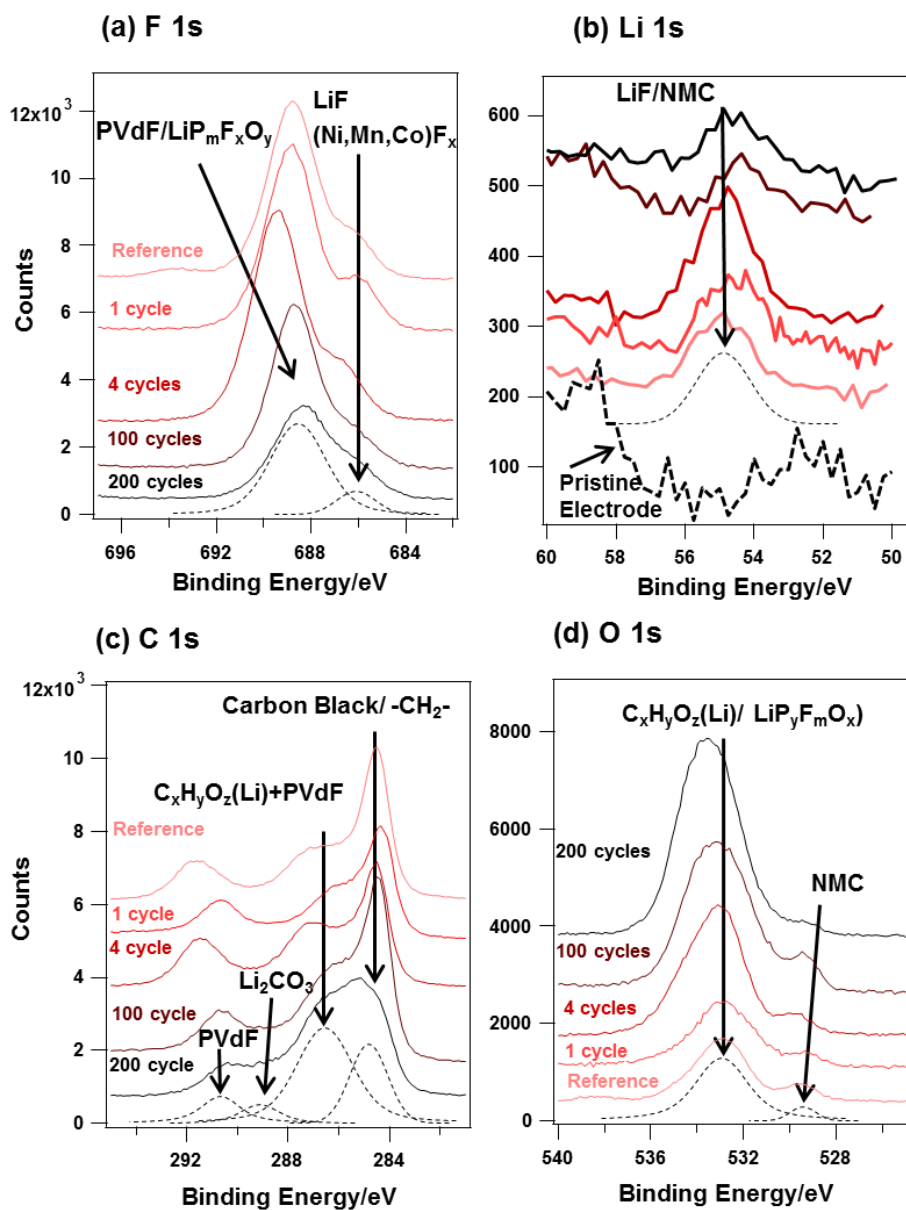**(b) Li 1s**

(c) C 1s

(d) O 1s

Figure 2.1 XPS spectra of F 1s (a), Li 1s (b), C 1s (c) and O 1s (d) over 200 cycles and their quantitative correlation (c). The dotted lines represent peak fittings of the bottom spectra on each graph.
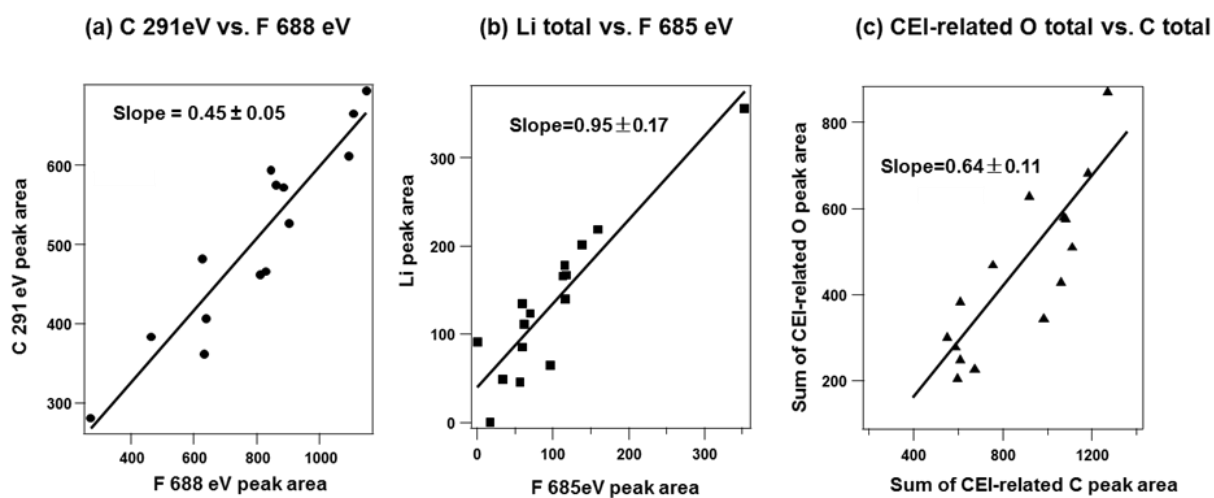
(a) C 291eV vs. F 688 eV

Slope = 0.45 ± 0.05

C 291 eV peak area

F 688 eV peak area

(b) Li total vs. F 685 eV

Slope=0.95±0.17

Li peak area

F 685eV peak area

(c) CEI-related O total vs. C total

Slope=0.64±0.11

Sum of CEI-related O peak area

Sum of CEI-related C peak area

Figure 2.2 Quantitative correlation of XPS peaks. The peak area was normalized by atomic sensitivity factor and the normalization factor described in experimental

$$A_{\text{C-containing CEI}} = A_{286eV} + A_{289eV} - A_{291\ eV}$$

where *A* symbolizes XPS peak area, and the 289 eV peak for Li_2CO_3 is only present after over 100 cycles.

Fig. 2c demonstrates the correlation between $A_{\text{C-containing CEI}}$ and $A_{O\ 532\ eV}$. The estimated O/C ratio is 0.64±0.11, which is reasonable considering that it represents a mixture of EC (O/C=1) and DEC (O/C=0.6) decomposition products.

2.3.1.2 CEI identification with binder-free electrodes

In both the C and F regions, XPS emission from PVDF overlaps with that from the CEI, making it difficult to quantify CEI species such as $LiP_mF_pO_n$ and $(Li)C_xH_yO_z$ (if present in low quantities). To remove interference from PVDF, we developed a "binder-free" electrode preparation process (details described in experimental section). The fabricated "binder-free" cathodes contained NMC and carbon black, but no PVDF binder. Fig. 2.3 shows the charge-discharge profile of a binder-free cathode. The cell shows a stable capacity at approximately 160 mAh/g, proving that removing the binder does not adversely impact the electrochemical behavior for the limited number of cycles investigated.

Fig. 2.4 shows the F (1s) and P (2p) spectra of binder-free electrodes after cycling for 1 to 4 times. The cycled cathodes were carefully rinsed with DMC three times before characterization. The F (1s) region is composed of two peaks: the 685 eV peak is assigned to LiF and the 688 eV peak is assigned to $LiP_mO_nF_p$ from $LiPF_6$ decomposition[18, 23]. Since the binder-free cathode has not PVDF present, it is now clear that the 688 eV peak arises purely from CEI species. The P (2p) region is composed of two peaks at 132 eV and 136 eV. The $2p_{1/2}$ and $2p_{3/2}$ spin-orbit components of P(2p) are separated by only 0.83 eV and are not separable under the conditions of these experiments. With the PVDF interference

removed, the peaks associated with $LiP_mF_pO_n$ species can now be quantified and correlations established. Fig. 2.3c shows a quantitive correlation of 688 eV F(1s) peak with the P (2p) peaks. As shown in Fig. 2.3c, a slope of 6.03±1.18 implies that one component of CEI layer contains F and P elements with F/P ratio of 6. Because there are multiple peaks in the P(2p) region, this component represents a mixture of decomposition products from $LiPF_6$ decomposition.

Fig. A1.4 displays the C (1s) and O (1s) spectra of the binder-free cathodes. The only significant peak in the C region belongs to carbon black, which indicates that $(Li)C_xH_yO_z$ species do not form in significant quantities during the initial four cycles. This observation is consistent with the results on composite electrodes shown in Fig. 2.1c, where significant growth of the 286 eV peak (assigned to PVDF+$(Li)C_xH_yO_z$) is only observed after relatively long cycling (100 cycle and 200 cycles). Therefore, the formation of $(Li)C_xH_yO_z$ species is identified as a relatively slow process, and cathodes during the initial few cycles possess only very small amounts of $(Li)C_xH_yO_z$.

From the studies of composite and binder-free cathode, there are several important conclusions that can be made: First, the quantitative correlations studies allow identification of three distinct components of the CEI layer: (1) LiF, (2) $LiP_mO_nF_p$ with P/F≈6, and (3) $(Li)C_xH_yO_z$ with O/C≈0.8. Besides LiF, the other two components represent a group of compounds that form simultaneously, and the elemental ratio estimate the averaged stoichiometry. LiF and $LiP_mF_pO_n$ form immediately at the onset of cycling, and their quantities did not grow significantly over cycles; $(Li)C_xH_yO_z$ does not form immediately, but grows slowly and continuously as evidenced by spectra obtained after 100 to 200 charge-discharge cycles.
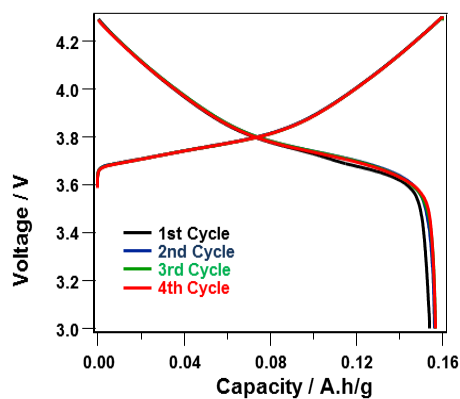
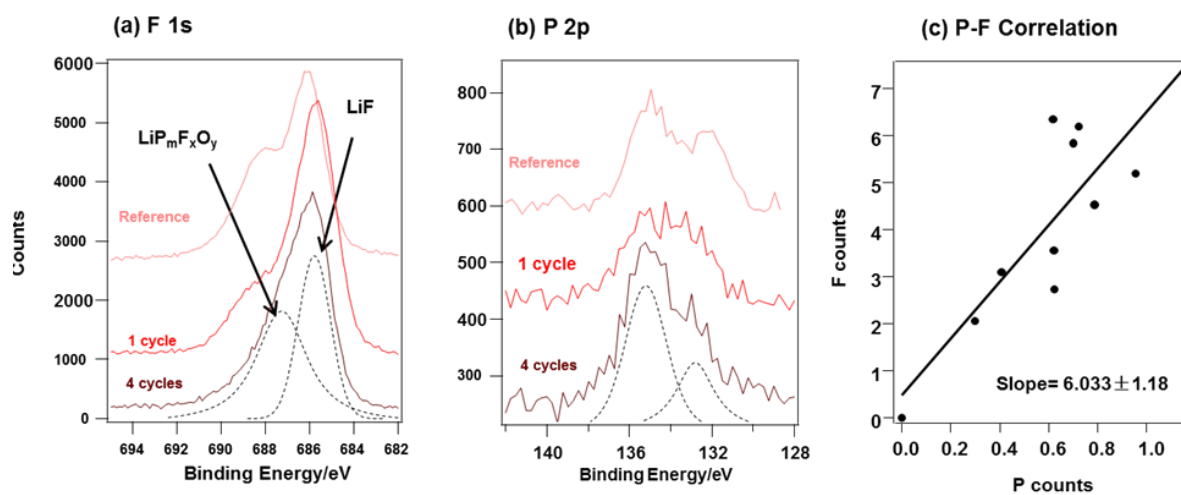**Figure 2.3 Charge-discharge profile of a binder-free NMC electrode- Li anode cell**

Figure 2.4 XPS spectra of F 1s (a) and P 1s (b) of binder-free electrodes and their quantitative

2.3.2 Identification of Anode SEI Migration Pathway

Following the establishment of proper CEI identification method, we designed two sets of experiments to validate the presence of an anode SEI migration pathway to form CEI species. The first one compares CEI formation in cells constructed with one separator vs. three separators. The increased number of separators would increase physical separation between cathode and anode and thus impede substance exchange between the two electrodes. The second set of experiments compares CEI formation in cells using NMC-Graphite vs. NMC-Lithium Titanate (LTO) cathode-anode pairs. LTO anodes are generally considered to be free of SEI-layer formation because the electrochemical potential (1.5 V vs. Li/Li$^+$) at which lithiation falls within the intrinsic stability window of carbonate electrolytes.[31-33] We hypothesize that if CEI layers are formed primarily by migration of species from anode to cathode, then when comparing cells that are charged such that the cathode reaches the same electrochemical potential in the charged state, we should see less formation of CEI species when using the LTO anode than when using the graphite anode.

2.3.2.1 CEI formation in one-separator and three-separator cells

Fig. 2.5 displays the electrochemical performance of half-cells made using 1 separator and using 3 separators. The half-cells were constructed from NMC cathodes, lithium anodes, 1M LiPF$_6$ (EC/DEC) electrolyte and one or three polypropylene separators. The first two cycles were formation cycles at C/10 charge-discharge. The remaining 3-100 cycles were at a charge rate of C/3 and discharge rate of 1C. In order for this comparison to be valid, the cathode must be cycled at the same current and over the same range of absolute electrochemcal potentials. One potential concern is whether the addition of more separators will lead to a small voltage drop across the battery, artificially lowering the potential
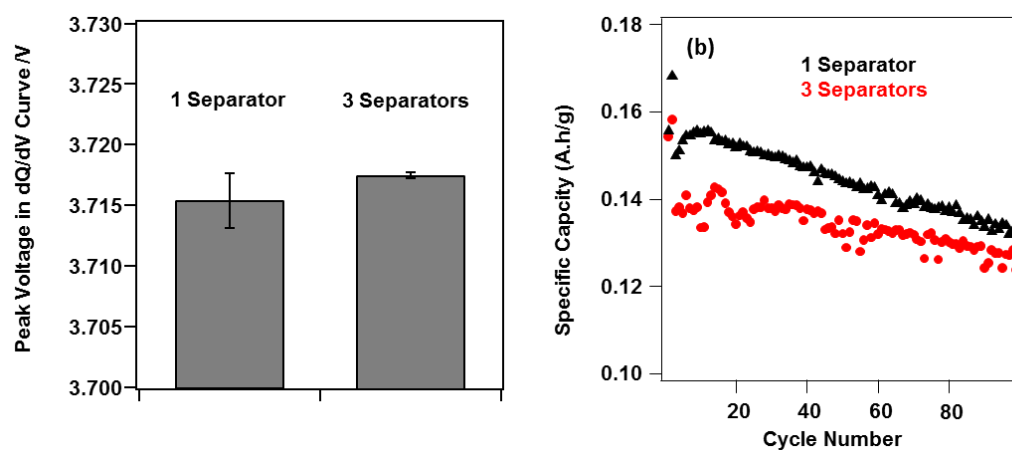
Fig. 2.5 (a) Lithium intercalation voltage calculated from differential capacity during charging (b) Cycling performance of one and three separator cells. The one separator cells are tested at 4.3V cut-off, and the three separator cells are tested at 4.305 V cut-off to compensate for small IR drops due to addition of separators.
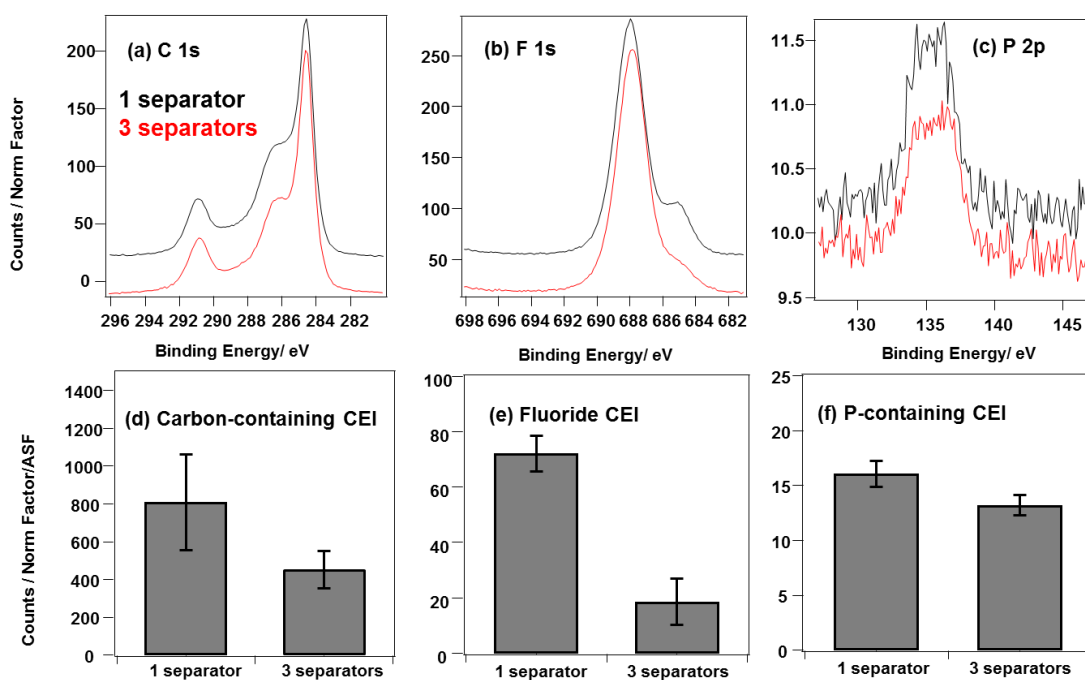
Figure 2.6 CEI formation comparison in one and three separator half cells. (a), (b) and (c) show example spectra in the C, F and P region. The counts are corrected with the normalization factor based on 0-800eV total electron counts. (d), (e) and (f) quantify the amount of CEI species that contains C, F and P. Average is taken of triplicate cells for one-separator case, and replicate cells in the three-separator case. Error bar shows one standard deviation. The counts for C, F and P have been normalized by atomic sensitivity factor and the normalization factor.

posed on cathodes. To test this, we differentiated the charging curves to obtain the differential capacity and then extracted the value of the lithium intercalation voltage $V_{lithiation}$; $V_{lithiation}$ is defined as the voltage at which the differential capacity reaches its maximum value (further details are in Fig. A1.5). Fig. 2.5a shows the lithium intercalation/deintercalation voltages obtained on 1-separator and 3-separator cells when the cells were operated at same current and voltage cut-off. The voltage drop caused by separators was estimated from $V_{lithiation}$. The comparison between cells indicate a slight 0.0045V at C/3. To compensate for the voltage drops, the three-separator cells were cycled at 4.305V cut-off during the remaining C/3-1C cycles. The resulting electrochemical performance is displayed in Fig. 2.5b. The three-separator cells show reversible charge-discharge capacity between 120-140 mA.h/g.

Fig. 2.6 summarizes the C (1s), F (1s) and P (2p) XPS spectra of NMC cathodes cycled in 1-separator and 3-separator cells for 100 times. These three elements were chosen to represent the three CEI components -$(Li)C_xH_yO_z$, LiF, and $LiP_mO_nF_p$. In Fig. 2.6a, a significant decrease of 286 eV peak intensity is observed after addition of more separators, indicating reduced formation of C-containing CEI. Similarly, Fig. 2.6b and Fig 6d show reduced formation of LiF and $LiP_mF_pO_n$. To check the reproducibility of this observation, triplicate cells were run and analyzed. Fig. 2.6c, 6d, and 6e summarizes the photoelectron emission peak area associated with C, F, and P, with error bars representing standard deviation of triplicate measurements. The peak areas were normalized by the appropriate atomic sensitivity factor and a normalization factor that corrects for total electron flux on different days (described in more detail in experimental session). Results from repeated measurements clearly indicate reduced CEI quantities as a function of increased anode-to-cathode separation. Since cathode-originated processes are expected to be independent of anode-cathode separation, it is evident that anode has taken part in CEI formation. Migration of SEI species from anode to cathode is the most

reasonable pathway.

To further confirm the SEI migration pathway, further experiments were conducted with coin full cells. Previously, researchers have occasionally reported different electrochemical performance or processes in full and half cells made with the same cathodes[38-39]. The differences have been attributed to lithium and graphite's different abilities to compensate for lithium loss[38], or their different surface area that lead to varied interaction with gas-phase decomposition products[39]. It is thus important to understand the impact of SEI migration in realistic full cell systems that are widely used in battery applications.

Fig. 2.7 shows the electrochemical performance of NMC-graphite full cells. Commercial matched anode (graphite)-cathode (NMC) electrodes were used, and the batteries were cycled between 3 V and 4.2 V. Based on the IR drop estimate in Fig. 2.7a, we expect that addition of more separators should not alter the lithiation voltages on NMC, and there was no sign of an IR drop caused by separators. Therefore, the same cut-off voltages were kept for the 3-separator full cells. Fig. 2.7b shows the cycling performance over 100 charge-discharge cycles. Both 1-separator and 3-separator full cells show similar discharge capacity and rate of capacity decay.

Fig. 2.8 displays the integrated C (1s), F (1s) and P (2p) XPS spectra. Addition of more separators reduced the CEI quantities on the cathode side. Triplicate measurements demonstrate statistical differences. The migration of anodic SEI species is validated in full cells.

2.3.2.2 SEI migration study with NMC-LTO full cells

In sections 3.2.1, SEI migration was evidenced by the dependence of CEI quantities on the physical separation between anode and cathode. Alternatively, if the amount of SEI formation could be modulated without altering the cathode cycling conditions, one would expect to the amount of CEI
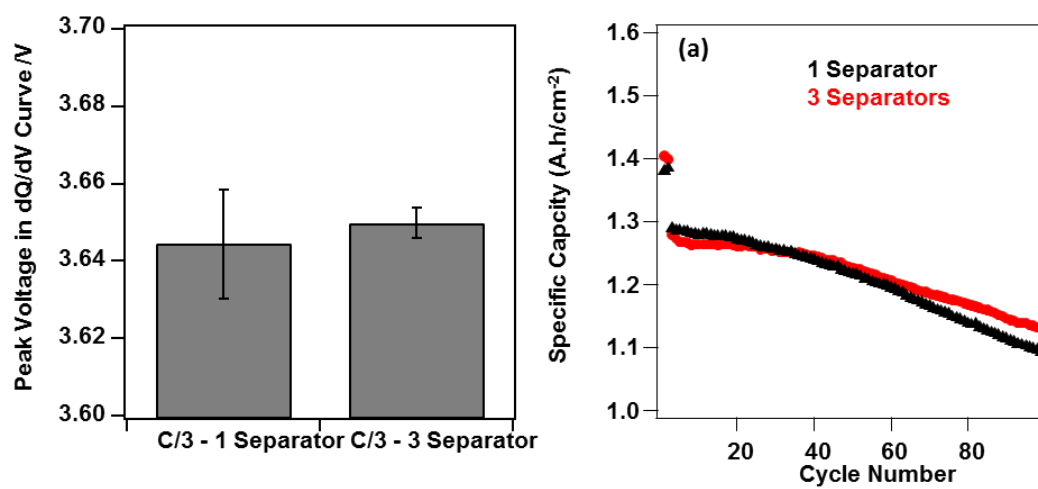
Fig. 2.7 (a) Lithium intercalation voltage calculated from differential capacity during charge (b) Cycling performance of one and three separator full cells
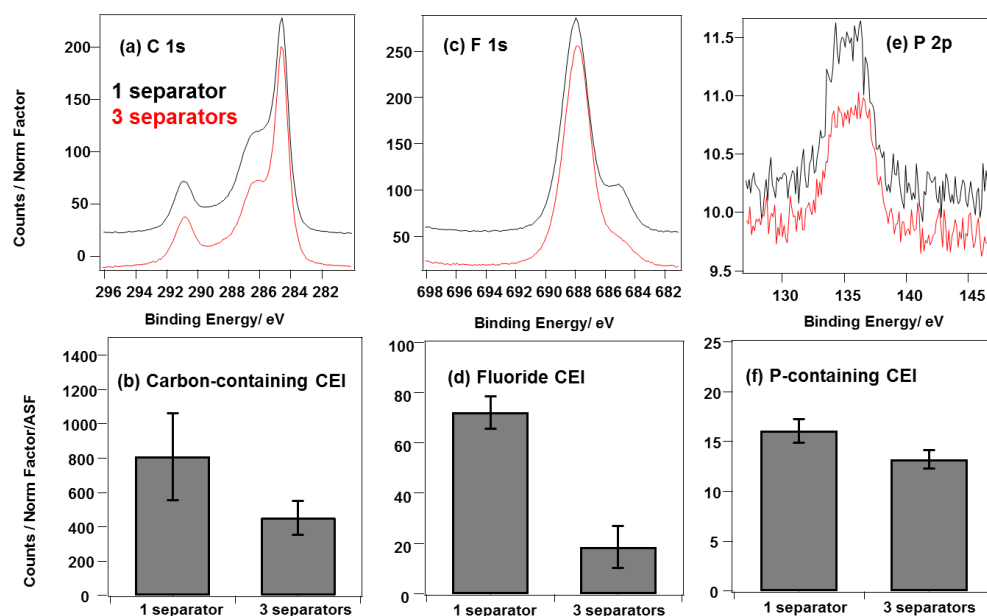
Figure 2.8 CEI formation comparison in one and three separator NMC-graphite full cells. (a), (c) and (f) show example spectra in the C, F and P region. ((b), (d) and (f) quantify the amount of CEI species that contains C, F and P. Average is taken of triplet cells. Error bar shows one standard deviation. The counts have been normalized by atomic sensitivity factor and the normalization factor.

species observed on the cathode depend on the amount of SEI species formed at the anode. To testify

this hypothesis, a series of NMC-Lithium Titanate(LTO) cells were constructed using the NMC

electrodes identical to those used in the NMC-graphite full cells. LTO is a well-performing anode

material that is oftentimes considered SEI-free.[29] Unlike graphite anode (~0.1V vs. Li/Li$^+$), LTO does

not form rich SEI layer because its lithium intercalation voltage of 1.5 V vs. Li is in a region where

most electrolyte materials are electrochemically stable [29-34]. That makes NMC-LTO a suitable model

system for study SEI migration. NMC-LTO cells were cycled between 2.8 V and 1.6 V because the

lithium intercalation voltage at the graphite (0.1 V vs. Li/Li$^+$) and LTO (1.5 V vs. Li/Li$^+$) anodes differs

by 1.4 V. Thus, when cycling between 2.8 V and 1.6 V vs. LTO, the cathode reaches the same potentials

as it does when cycling between 3.0 and 4.2 V vs. graphite. The cycling performance of NMC-LTO

cells is shown in Fig. A1.6. Fig. A1.7 analyzes the differential capacity plots obtained from our full cell

data, and the results further confirm that the high cut-off potential of NMC cathode in NMC-LTO cells

is at least equal to, if not even slightly higher than that in the NMC-graphite cells. Any observation of

reduced CEI formation in NMC-LTO cells would not be related to a change in cathode-originated

processes.

Fig. 2.9 shows XPS data characterizing CEI formation on NMC-graphite and NMC-LTO full cells.

Following the switch to the less reactive LTO anodes, the data in Fig. 2.9a, 9b, and 9c show a significant

decrease in the 286 eV C(1s) peak from (Li)$C_xH_yO_z$, the 685 eV F(1s) peak from LiF, and the 135 eV

P(2p) peak from $LiP_mO_nF_p$. Fig. 2.9d, 9e, and 9f summarizes the photoelectron emission peak area

associated with C, F, and P with error bars representing standard deviation of triplicate measurements.

It is evident that CEI quantities decrease as a function of decreased anode-electrolyte reactivity. Anode-

to-cathode SEI migration is reduced after switching from reactive graphite anode to a less reactive LTO.
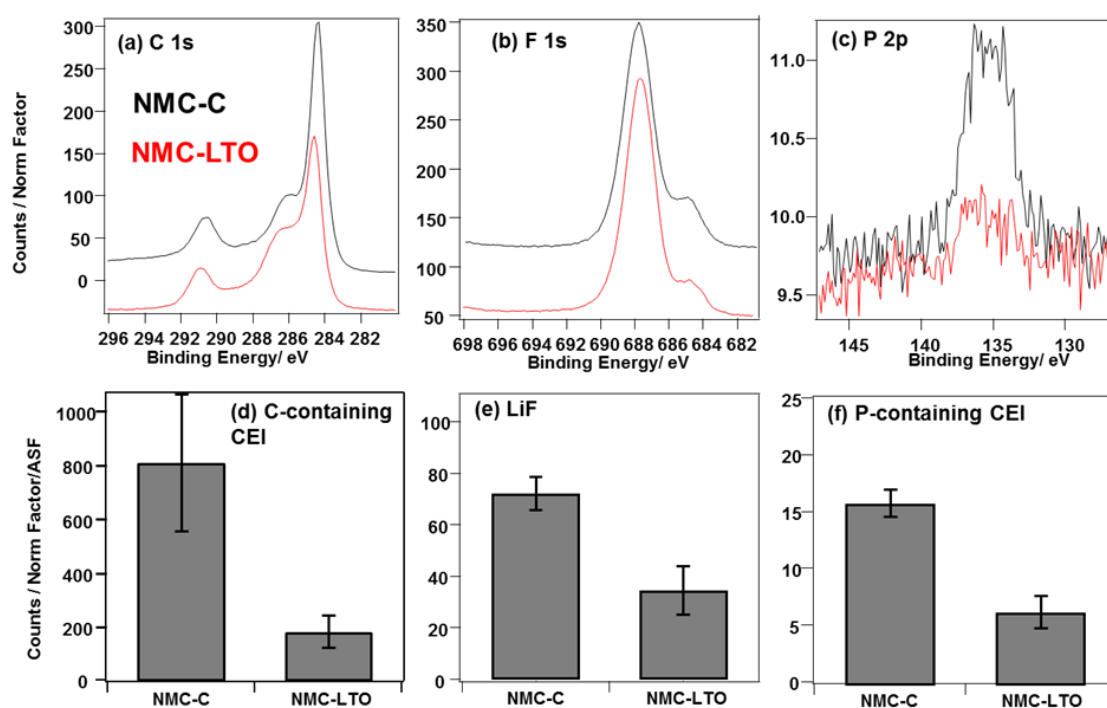
Figure 2.9 CEI formation comparison in NMC-Graphite and NMC-LTO full cells. NMC-C is short for NMC-Graphite. (a), (b) and (c) show example spectra in the C, F and P region. (d), (e) and (f) quantify the amount of CEI species that contains C, F and P. Average is taken of triplet cells. Error bar shows one standard deviation. The counts for C, F and P have been normalized by sensitivity factor and the normalization factor. The NMC-graphite results are reproduced from Fig.2.7.

2.3.3 Migration Study with Al₂O₃-coated NMC

The above results demonstrate that migration from anode to cathode is an important contributor to CEI formation. To improve the performance of cathodes, researchers have developed coatings such as Al₂O₃ to reduce the formation cathode-electrolyte interphase.[15, 17-18] It becomes important to examine the interaction of coatings with anode migrants to better interpret their working mechanisms.

Fig. 2.10 shows the electrochemical performance of NMC-Li half cells with an Al₂O₃ ALD coating compared with uncoated cathodes. The Al₂O₃ coatings under study were deposited by five cycles of atomic layer deposition. These data show that the coated cathodes have an in initial loss in capacity but greatly increased stability and increased Coulombic efficiency. Previous studies have shown that the reduced initial capacity is associated with the increased cell resistance due to the presence of the Al₂O₃.

Fig. 2.11 shows a comparison of the F(1s) and C(1s) photoemission peak areas obtained on Al₂O₃-coated NMC and bare NMC, both cycled after 100 times. Fig. 2.11a shows that LiF formation is reduced by approximately 62% after introduction of Al₂O₃ coatings. However, unlike our observation on bare NMC cathodes, addition of more separators did not further reduce the quantities of LiF species on Al₂O₃-coated NMC, as the average fluoride quantities from one- and three-separator cells are within error bars of each other. Fig. 2.11b summarizes the photoemission peak area from the C-containing species ($A_{\text{C-containing CEI}} = A_{286eV} + A_{289eV} - A_{291\ eV}$). Al₂O₃ coatings have reduced the amount of C-containing CEI by approximately 28%. Al₂O₃ coatings reduced the amount of C-containing CEI by approximately 28%. Cells with 3 separators shows on average less C-containing CEI. Overall, our results indicate that SEI migration from anode to cathode is not as significant when using cathodes that have been coated with Al₂O₃, especially in regard of F-containing species.

Based on Fig. 2.6, incorporation of three separators reduced fluoride-containing CEI by 56% and

C-containing CEI by 27%, and those numbers give a rough estimation of portion of CEI originating from SEI migrants. Notably, that Al_2O_3 coatings reduced total LiF quantity by 63% and C-containing CEI decreases by 28%, and both numbers are close to the portion of CEI originating from SEI migrants. While these similarities may be coincidental, it is also quite possible that part of the improvement observed from coating the cathode material is to reduce the migration of species from the anode side.

We propose two possible mechanisms that could explain how coatings reduce migrated SEI. First, the adhesion of migrated species could be affected by factors such as the surface charge and/or presence of specific chemical groups. Thus, differences in the chemical or physical interaction between the migrating species and the NMC or Al_2O_3-NMC materials could impact the adhesion and subsequent build-up of the CEI. A second mechanism is based on prior literature reports suggesting that Al_2O_3 can dissolve in the electrolyte and migrate to the anode to form an anodic coating;[24, 36] if Al_2O_3 forms a coating on the anode, then it may impact subsequent anode reactions and, in turn, the migration of anode SEI species to the cathode.

Scheme 2.1 and Scheme 2.2 summarize the observations related to the SEI migration. Scheme 2.1 is based on data in section 2.3.2.1 and 2.3.2.2. CEI quantities were comparatively studied in one and three separator half/full cells as well as in NMC-graphite and NMC-LTO cells. In both sets of comparisons, the potential window and current on NMC cathodes remained unchanged while the distance of anode to cathode or SEI formation on anode were modulated. The results consistently show that CEI formation strongly depends on anode-based processes, namely migration of SEI components to the surface of cathode. Scheme 2.2 demonstrates the role of Al_2O_3 coatings based on experimental results in section 2.3.2.3. We propose that Al_2O_3 can reduce CEI formation via preventing adhesion of SEI to the cathode and/or via reducing SEI formation on anode through coating migration.
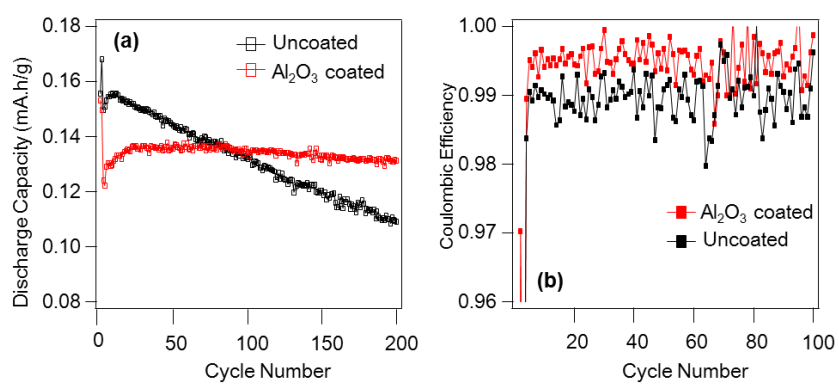
Figure 2.10 Electrochemical performance of uncoated and Al$_2$O$_3$ coated

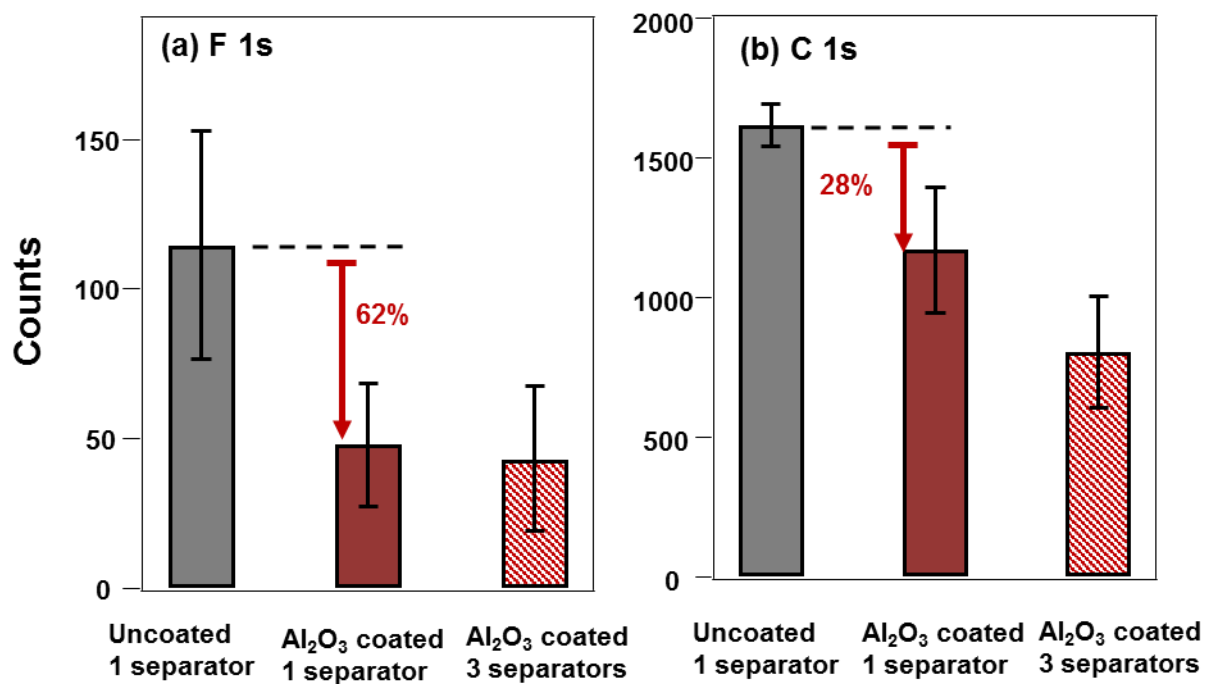**NMC (a) Specific discharge capacity (b) Columbic Efficiency**

Figure 2.11 Migration study of Al₂O₃ coated NMC (a) LiF content based on F 1s spectra (b) Content of C-containing CEI based on C 1s spectra. Error bar of the main figure is based of standard deviation, and error bars of the intersect marks the standard deviation of the mean.

2.4   Summary

In this article, the composition and stoichiometry of cathode-electrolyte interphase (CEI) were studied by quantitative XPS. Three major components of CEI species were identified with elemental correlations in regular and binder-free electrode, which include $CH(Li)_zO_{0.6}$, $Li_xPF_6O_y$ and LiF. Migration studies in NMC-Li, NMC-graphite and NMC-LTO cells show that CEI not only formed by electrolyte decomposition on the cathode, but also by migration of anodic decomposition products. In the case study with atomically-thin Al_2O_3, we found indications that the cathode coatings reduced the deposition of anodic migrants on the cathode. Overall, the inclusion of anode-assisted process is essential to correctly interpret surface phenomenon on the cathode side and conceptualize cathode-electrolyte interface formation.
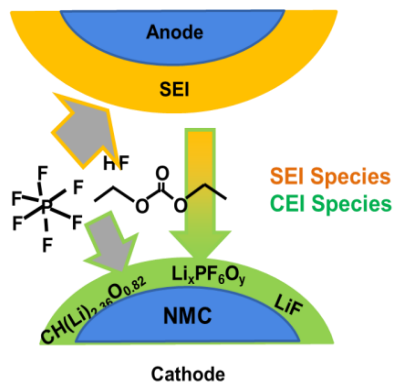
Scheme 2.1 Illustration of CEI formation pathway via migration
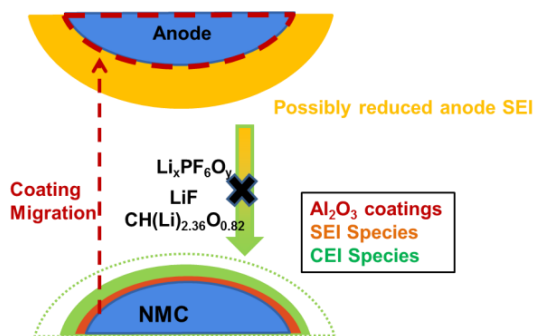
Scheme 2.2 Electrochemical processes in Al$_2$O$_3$ coated NMC cells

2.5 Reference

1.   Ohzuku, T.; Makimura, Y., Layered lithium insertion material of LiCo$_{1/3}$Ni$_{1/3}$Mn$_{1/3}$O$_2$ for lithium-ion batteries. *Chemistry Letters* **2001,**   (7), 642-643.

2.   Hwang, B. J.; Tsai, Y. W.; Carlier, D.; Ceder, G., A combined computational/experimental study on LiNi$_{1/3}$Co$_{1/3}$Mn$_{1/3}$O$_2$. *Chemistry of Materials* **2003,** *15* (19), 3676-3682.

3.   Kim, J. M.; Chung, H. T., The first cycle characteristics of Li Ni$_{1/3}$Co$_{1/3}$Mn$_{1/3}$O$_2$ charged up to 4.7 V. *Electrochimica Acta* **2004,** *49* (6), 937-944.

4.   Choi, J.; Manthiram, A., Investigation of the irreversible capacity loss in the layered LiNi$_{1/3}$Mn$_{1/3}$Co$_{1/3}$O$_2$ cathodes. *Electrochemical and Solid State Letters* **2005,** *8* (8), C102-C105.

5.   Wang, J.; Yao, X. Y.; Zhou, X. F.; Liu, Z. P., Synthesis and electrochemical properties of layered lithium transition metal oxides. *Journal of Materials Chemistry* **2011,** *21* (8), 2544-2549.

6.   Dolotko, O.; Senyshyn, A.; Muhlbauer, M. J.; Nikolowski, K.; Ehrenberg, H., Understanding structural changes in NMC Li-ion cells by in situ neutron diffraction. *Journal of Power Sources* **2014,** *255*, 197-203.

7.   Jiang, J.; Buhrmester, T.; Eberman, K. W.; Krause, L. J.; Dahn, J. R., Electrochemical and thermal comparisons of Li Ni$_{0.1}$Co$_{0.8}$Mn$_{0.1}$O$_2$ synthesized at different temperatures (900, 1000, and 1100 degrees C). *Journal of the Electrochemical Society* **2005,** *152* (1), A19-A22.

8.   MacNeil, D. D.; Lu, Z.; Dahn, J. R., Structure and electrochemistry of Li Ni$_x$Co$_{1-2x}$Mn$_x$O$_2$ (0 <= x <= 1/2). *Journal of the Electrochemical Society* **2002,** *149* (10), A1332-A1336.

9.   Lu, Z. H.; MacNeil, D. D.; Dahn, J. R., Layered cathode materials Li Ni$_x$Li$_{1/3-2x/3}$Mn$_{2/3-x/3}$O$_2$ for lithium-ion batteries. *Electrochemical and Solid State Letters* **2001,** *4* (11), A191-A194.

10. Lu, C. H.; Shen, B. J., Electrochemical characteristics of LiNi$_{1/3}$Co$_{1/3}$Mn$_{1/3}$O$_2$ powders prepared from microwave-hydrothermally derived precursors. *Journal of Alloys and Compounds* **2010,** *497* (1-2), 159-165.

11. Shaju, K. M.; Rao, G. V. S.; Chowdari, B. V. R., Influence of Li-ion kinetics in the cathodic performance of layered Li(Ni$_{1/3}$Co$_{1/3}$Mn$_{1/3}$)O$_2$. *Journal of the Electrochemical Society* **2004,** *151* (9), A1324-A1332.

12. Wu, Y.; Murugan, A. V.; Manthiram, A., Surface modification of high capacity layered Li Li$_{0.2}$Mn$_{0.54}$Ni$_{0.13}$Co$_{0.13}$O$_2$ cathodes by AlPO$_4$. *Journal of the Electrochemical Society* **2008,** *155* (9), A635-A641.

13. Armand, M.; Tarascon, J. M., Building better batteries. *Nature* **2008,** *451* (7179), 652-657.

14. Aurbach, D., Review of selected electrode-solution interactions which determine the performance of Li and Li ion batteries. *Journal of Power Sources* **2000,** *89* (2), 206-218.

15. Shen, D. D.; Zhang, D. W.; Wen, J. W.; Chen, D. M.; He, X. J.; Yao, Y. J.; Li, X. L.; Duger, C., LiNi$_{1/3}$Co$_{1/3}$Mn$_{1/3}$O$_2$ coated by Al$_2$O$_3$ from urea homogeneous precipitation method: improved Li storage performance and mechanism exploring. *Journal of Solid State Electrochemistry* **2015,** *19* (5), 1523-1533.

16. Su, Y. T.; Cui, S. H.; Zhuo, Z. Q.; Yang, W. L.; Wang, X. W.; Pan, F., Enhancing the High-Voltage Cycling Performance of   LiNi$_{0.5}$Mn$_{0.3}$Co$_{0.2}$O$_2$ by Retarding Its Interfacial Reaction with an Electrolyte

by Atomic-Layer-Deposited Al_2O_3. *ACS Appl. Mater. Interfaces* **2015,** *7* (45), 25105-25112.

17. Myung, S. T.; Izumi, K.; Komaba, S.; Sun, Y. K.; Yashiro, H.; Kumagai, N., Role of alumina coating on Li-Ni-Co-Mn-O particles as positive electrode material for lithium-ion batteries. *Chemistry of Materials* **2005,** *17* (14), 3695-3704.

18. Kim, J. W.; Kim, D. H.; Oh, D. Y.; Lee, H.; Kim, J. H.; Lee, J. H.; Jung, Y. S., Surface chemistry of $LiNi_{0.5}Mn_{1.5}O_4$ particles coated by Al_2O_3 using atomic layer deposition for lithium-ion batteries. *Journal of Power Sources* **2015,** *274*, 1254-1262.

19. Li, C.; Zhang, H. P.; Fu, L. J.; Liu, H.; Wu, Y. P.; Ram, E.; Holze, R.; Wu, H. Q., Cathode materials modified by surface coating for lithium ion batteries. *Electrochimica Acta* **2006,** *51* (19), 3872-3883.

20. Wu, Y.; Manthiram, A., Effect of surface modifications on the layered solid solution cathodes (1-z) Li $Li_{1/3}Mn_{2/3}$ O_2-(z) Li $Mn_{0.5y}Ni_{0.5y}Co_{2y}$ O_2. *Solid State Ionics* **2009,** *180* (1), 50-56.

21. Kim, Y. J.; Kim, H.; Kim, B.; Ahn, D.; Lee, J. G.; Kim, T. J.; Son, D.; Cho, J.; Kim, Y. W.; Park, B., Electrochemical stability of thin-film $LiCoO_2$ cathodes by aluminum-oxide coating. *Chemistry of Materials* **2003,** *15* (7), 1505-1511.

22. Kim, C. A.; Choi, H. J.; Lee, J. H.; Yoo, S. Y.; Kim, J. W.; Shim, J. H.; Kang, B., Influence of surface modification on electrochemical performance of high voltage spinel ordered-$LiNi_{0.5}Mn_{1.5}O_4$ exposed to 5.3 V for 100 h before and after surface modification with ALD method. *Electrochimica Acta* **2015,** *184*, 134-142.

23. Verdier, S.; El Ouatani, L.; Dedryvere, R.; Bonhomme, F.; Biensan, P.; Gonbeau, D., XPS study on Al_2O_3- and $AlPO_4$-coated $LiCoO_2$ cathode material for high-capacity li ion batteries. *Journal of the Electrochemical Society* **2007,** *154* (12), A1088-A1099.

24. Jung, Y. S.; Lu, P.; Cavanagh, A. S.; Ban, C.; Kim, G.-H.; Lee, S.-H.; George, S. M.; Harris, S. J.; Dillon, A. C., Unexpected Improved Performance of ALD Coated $LiCoO_2$/Graphite Li-Ion Batteries. *Advanced Energy Materials* **2013,** *3* (2), 213-219.

25. Jarry, A.; Gottis, S.; Yu, Y. S.; Roque-Rosell, J.; Kim, C.; Cabana, J.; Kerr, J.; Kostecki, R., The Formation Mechanism of Fluorescent Metal Complexes at the $Li_xNi_{0.5}Mn_{1.5}O_{4-\delta}$/Carbonate Ester Electrolyte Interface. *Journal of the American Chemical Society* **2015,** *137* (10), 3533-3539.

26. Cherkashinin, G.; Nikolowski, K.; Ehrenberg, H.; Jacke, S.; Dimesso, L.; Jaegermann, W., The stability of the SEI layer, surface composition and the oxidation state of transition metals at the electrolyte-cathode interface impacted by the electrochemical cycling: X-ray photoelectron spectroscopy investigation. *Physical Chemistry Chemical Physics* **2012,** *14* (35), 12321-12331.

27. Dedryvere, R.; Laruelle, S.; Grugeon, S.; Gireaud, L.; Tarascon, J. M.; Gonbeau, D., XPS identification of the organic and inorganic components of the electrode/electrolyte interface formed on a metallic cathode. *Journal of the Electrochemical Society* **2005,** *152* (4), A689-A696.

28. Niehoff, P.; Winter, M., Composition and Growth Behavior of the Surface and Electrolyte Decomposition Layer of/on a Commercial Lithium Ion Battery $Li_xNi_{1/3}Mn_{1/3}Co_{1/3}O_2$ Cathode Determined by Sputter Depth Profile X-ray Photoelectron Spectroscopy. *Langmuir* **2013,** *29* (51), 15813-15821.

29. Ferg, E.; Gummow, R. J.; Dekock, A.; Thackeray, M. M., Spinel Anodes for Lithium-Ion Batteries. *Journal of the Electrochemical Society* **1994,** *141* (11), L147-L150.

30. Ohzuku, T.; Ueda, A.; Yamamoto, N., Zero-Strain Insertion Material of Li [$Li_{1/3}Ti_{5/3}$]O_4 for

Rechargeable Lithium Cells. *Journal of the Electrochemical Society* **1995,** *142* (5), 1431-1435.

31. Zhang, S. S.; Xu, K.; Jow, T. R., Optimization of the forming conditions of the solid-state interface in the Li-ion batteries. *Journal of Power Sources* **2004,** *130* (1-2), 281-285.

32. Schranzhofer, H.; Bugajski, J.; Santner, H. J.; Korepp, C.; Moller, K. C.; Besenhard, J. O.; Winter, M.; Sitte, W., Electrochemical impedance spectroscopy study of the SEI formation on graphite and metal electrodes. *Journal of Power Sources* **2006,** *153* (2), 391-395.

33. Bernhard, R.; Metzger, M.; Gasteiger, H. A., Gas Evolution at Graphite Anodes Depending on Electrolyte Water Content and SEI Quality Studied by On-Line Electrochemical Mass Spectrometry. *Journal of the Electrochemical Society* **2015,** *162* (10), A1984-A1989.

34. Zhao, B.; Ran, R.; Liu, M. L.; Shao, Z. P., A comprehensive review of $Li_4Ti_5O_{12}$-based electrodes for lithium-ion batteries: The latest advancements and future perspectives. *Mater. Sci. Eng. R-Rep.* **2015,** *98*, 1-71.

35. Liu, W.; Wang, M.; Gao, X. L.; Zhang, W. D.; Chen, J. T.; Zhou, H. H.; Zhang, X. X., Improvement of the high-temperature, high-voltage cycling performance of $LiNi_{0.5}Co_{0.2}Mn_{0.3}O_2$ cathode with TiO_2 coating. *Journal of Alloys and Compounds* **2012,** *543*, 181-188.

36. Bettge, M.; Li, Y.; Sankaran, B.; Rago, N. D.; Spila, T.; Haasch, R. T.; Petrov, I.; Abraham, D. P., Improving high-capacity $Li_{1.2}Ni_{0.15}Mn_{0.55}Co_{0.1}O_2$-based lithium-ion cells by modifiying the positive electrode with alumina. *Journal of Power Sources* **2013,** *233*, 346-357.

37. Briggs, D., Handbook of X-ray Photoelectron Spectroscopy C. D. Wanger, W. M. Riggs, L. E. Davis, J. F. Moulder and G. E.Muilenberg Perkin-Elmer Corp., Physical Electronics Division, Eden Prairie, Minnesota, USA, 1979.

38. Kim, J. H.; Pieczonka, N. P. W.; Li, Z. C.; Wu, Y.; Harris, S.; Powell, B. R., Understanding the capacity fading mechanism in $LiNi_{0.5}Mn_{1.5}O_4$/graphite Li-ion batteries. *Electrochimica Acta* **2013,** *90*, 556-562.

39. Streich, D.; Gueguen, A.; Mendez, M.; Chesneau, F.; Novak, P.; Berg, E. J., Online Electrochemical Mass Spectrometry of High Energy Lithium Nickel Cobalt Manganese Oxide/Graphite Half- and Full-Cells with Ethylene Carbonate and Fluoroethylene Carbonate Based Electrolytes. *Journal of the Electrochemical Society* **2016,** *163* (6), A964-A970.

Chapter 3

Improving Performance of $LiNi_{0.5}Mn_{0.3}Co_{0.2}O_2$ Cathode

with Surface Silylation

Reprint with permission from Fang, S., Dreibelbis, M., Hamers, R. J., Improving performance of

$LiNi_{0.5}Mn_{0.3}Co_{0.2}O_2$ cathode with surface silylation, *in preparation*

3.1 Introduction

Layered cathode material $LiNi_xMn_yCo_{1-x-y}O_2$ (NMC) is promising for HEV and EV applications

because of its high capacity, high operational voltage, low cost, and enhanced safety compared to the

conventional $LiCoO_2$ cathode.[1-7] To overcome the relatively high capacity decay at high cut-off

voltages,[4, 8-9] efforts were taken to improve the cycle retention of NMC cathodes via surface

modification. Previous research has shown that metal oxide[10-14] and polymeric coatings[15-18] can reduce

irreversible capacity loss, improve rate capability, and improve cycle life. The proposed mechanisms

include suppression of lattice stress,[19] reduced electrolyte breakdown,[20-21] suppression of transition

metal dissolution,[22] and scavenging of HF from the electrolyte.[23]

Small and non-crosslinking molecules are not commonly used for coating of cathodes. A couple of

literature reported on anode treatment with diazonium[24-25] or through silylation,[26] but such investigation

in cathodes is quite limited. In view of the current literature, we believe that well-established study of

cathode treatment with small organic groups will provide good alternative solutions for improving

cathode design and add to the current knowledge on surface modification strategies. Hexamethyl

disilazane (HMDS) is a reagent that reacts quickly with water and hydroxyls.[27] Previous work on

silylated graphite anode proposes the removal of surface hydroxyl and water as the main reason for

reduced irreversible capacity loss.[26] On the other hand, work on HMDS-containing $LiPF_6$ electrolyte

has identified HMDS as an HF scavenger.[28] While the different mechanisms may be rationalized by the authors' different application methods, it is clearly beneficial to further investigate that the working mechanism of HMDS, especially if it is going to be used for cathode treatment.

In this work, we performed silylation of $LiNi_xMn_yCo_{1-x-y}O_2$ (NMC) cathodes with HMDS, chlorotrimethylsilane (TMCS), and polysilazane. The samples were probed with XPS, *in situ* mass spectrometry, and impedance spectroscopy to determine the surface coverage-performance relationship and examine processes including CEI formation, transition metal dissolution and interfacial lithium-ion transport. The observed effects were further discussed in relation to HF scavenging, surface hydroxyl removal and hydrophobicity modulation induced by the Si-containing coatings.

3.2 Experiment

Functionalization of $LiNi_{0.5}Mn_{0.3}Co_{0.2}O_2$ (NMC) Treatment of NMC (TODA America) was conducted in Argon glovebox (LC Technologies) that was maintained at <1ppm oxygen and water. a) **HM** sample was obtained by overnight stirring of 2g NMC with 2mL toluene (Sigma-Aldrich) that contained 13mg hexamethyl disilazane (HMDS,Sigma-Aldrich) at room temperature. b) **SILY** sample was obtained by stirring 2g NMC with 2mL 10:1 (w/w) mixture of HMDS and chlorotrimethylsilane (TMCS, Sigma-Aldrich) at 70 ˚C overnight. This procedure was adapted from previous literature.[26] c) **PS** sample was obtained by stirring 2g NMC with 2mL toluene that contained 150 mg polysilazane resin at room temperature for overnight. The resin was obtained by Kadko Inc. and contained 4.5% polysilzane solids in isopropyl acetate solvent. After treatment, NMC powder was separated from the reaction mixture, rinsed with 2mL of toluene for three times, and dried at 150 ˚C overnight before cathode fabrication.

Fabrication of Cathode Film The cathode slurry was prepared by mixing 92% w/w NMC powder

(silylated or untreated), 3.5% w/w carbon black (Timical Super C65) and 4.5% w/w PVDF (Solef) in N-Methyl-2-porrolidone (NMP, Sigma-Aldrich) solvent. The slurry was cast on Al foil (MTI) with 150 nm doctor blade. The film was dried under vacuum, calendared with a Carver hydraulic lab press at 3 ton/cm^2, and dried again under vacuum at 150°C overnight before use.

Coin Cell Characterization. The coin cells were assembled using the fabricated NMC cathode film, Li metal anode (Chemetall Foot Corp.), polypropylene separator (Celgard 2500) and 1M LiPF$_6$ in EC/DEC electrolyte (BASF). The cycle retention was characterized by constant current cycling between 3V and 4.3V (vs. Li) on an Arbin BT-2000 battery tester. For the first two formation cycles, the charge-discharge rate was set to C/10 (~0.23mA). From the third cycle on, the charge rate was C/3 (~0.8mV) and discharge rate was 1C (~2.3mA). Triplicate cells were tested to ensure reproducibility.

Thermal Mass Spectrometry The thermal mass spectroscopy was conducted with a SRS UGA200 gas analyzer. A custom-built sampling system was shown in the Fig. 3.1. 1mL electrolyte with 0.05g treated or untreated NMC powder were placed into glass sample vial. A programmable temperature controller (PTC 10, Stanford Research Systems) was used to control the temperature of the reaction mixture. Argon gas at a flow rate of 3 sccm at atmospheric pressure (controlled by mass flow controller) passed over the sample and carried gaseous electrolyte decomposition products to the gas analyzer. The mass spectra of the gas-phase species were recorded averaging 5 scans taken from 1 to 200 amu. This set up was a modified version of a set-up described in previous publication.[29] Gas-phase decomposition was detected *real time* as they formed in the reaction vial.

X-ray Photoelectron Spectroscopy (XPS) XPS was performed with Thermo Fisher K-Alpha XPS system. For powders, the sample was loaded on a carbon tape. The survey spectra were collected at 200
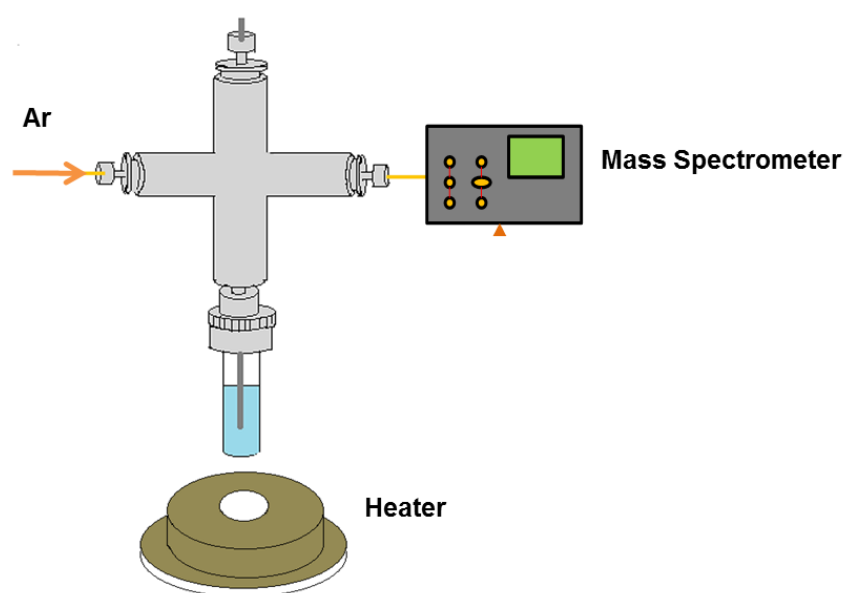
Fig. 3.1 Set up for thermal mass spectrometry

eV pass energy, and the high-resolution Si (2s) and Co (2p) spectra were collected at 50 eV pass energy. To characterize cathode-electrolyte interphase (CEI) formation, coin cells were disassembled in Argon glovebox and the cathode film was soaked in 2mL dimethyl carbonate (DMC, Sigma-Aldrich) for 1 minute for 3 times. The O(1s), P(2p), F(1s), C(1s) and Li(1s) high resolution spectra were collected with 58.7 eV pass energy.

Inductively Coupled Plasma Optical Emission Spectroscopy (ICP-OES) ICP was performance with a PerkinElmer Optima 2000 ICPOES system to determine transition metal dissolution from NMC cathodes. Coin cells cycled after 20 times were disassembled in Argon glovebox. The cathode was rinsed with DMC for three times, and the DMC was collected and combined with the separator and all other stainless steel cell parts. After soaking overnight, the cell parts were removed from the vial and DMC was dried out under vacuum overnight. The remaining solid substance in the vial was re-digested with 1mL 69% nitric acid (electrolyte digest). Nitric acid for trace analysis (Fluka Analytical) was used to avoid metal contamination during digestion. Lithium anode was collected in a separate container during coin cell disassembly and dissolved with 1mL 18MΩ water inside the fume hood. The solution was further digested with 1mL concentrated nitric acid (anode digest). The electrolyte digest and anode digest were separately diluted to 10mL with 18MΩ water and tested with ICP-OES.

Electrochemical Impedance Spectroscopy (EIS) EIS were performed with Metrohm Autolab potentiostat. Freshly-assembled coin cells were characterized between 0.1 and 10000 Hz frequency with 10 mV magnitude, and the cell were held at 50 mV higher than their open circuit potential (~3V). Cycled coin cells were characterized the same way and the voltage was held at 4.3 V for charged battery and 3.7 V for discharged battery.

Diffused Reflectance Infrared Fourier Transform Spectroscopy (DRIFTS) IR spectra were

collected with Bruker Vertex70 FTIR spectrometer. The treated and untreated NMC powders were grinded with KBr with a mortar and pestle inside the glovebox. The ratio of NMC to KBr was 1:1000 w:w. The powder was transferred to the spectrometer without air exposure using a sealed chamber (Praying Mantis high temperature reaction chamber). IR spectra were collected in the range of 3600-600 cm^{-1} using 0.1% untreated NMC in KBr as the background spectra.

Contact Angle Measurement Contact angle measurements were performed with OCA 15 plus contact angle measurement system to determine hydrophobicity of the treated NMC. Flat surface of NMC powder was prepared by pressing powder into indium foil under 10 ton pressure for 1 minute. Water was dispensed at 0.5 µL/s, and contact angle was measured for the sessile drop formed right after break of droplet from the needle top. The contact angle was also measured of calendared composite NMC cathodes. For measuring the water contact angle on NMC composite cathode, 8 µL water was dispensed onto a flat session of the cathode, and contact angle was measured for both pendant and sessile droplets. In an attempt to measure contact angle of EC/DEC (1:1 w/w mixture with no $LiPF_6$) with NMC composite electrodes, 3 µL solvent was dispensed at 1 µL/s. Due to fast absorption of solvent into NMC electrodes, the contact angle was measured of pendant droplet as soon as the dispense stopped.

3.3 Results and Discussion

3.3.1 Coverage-Performance Relationship of Silylated Cathodes

3.3.1.1 Surface coverage of silylated cathodes

Fig. 3.2 demonstrates XPS characterization of the Si coverage on HM, SILY and PS samples. Si (2s) was used instead of Si (2p) because Co (3s) peak was very close to Si (2p) signal (Si (2p) ~ 103 eV, Co (3s) ~101 eV. The presence of Si confirms successful grafting of Si-containing groups to NMC surface. The Si/Co ratios are 0.32 for HM, 0.79 for SILY and 4.97 for PS. Based on bulk Co density Co
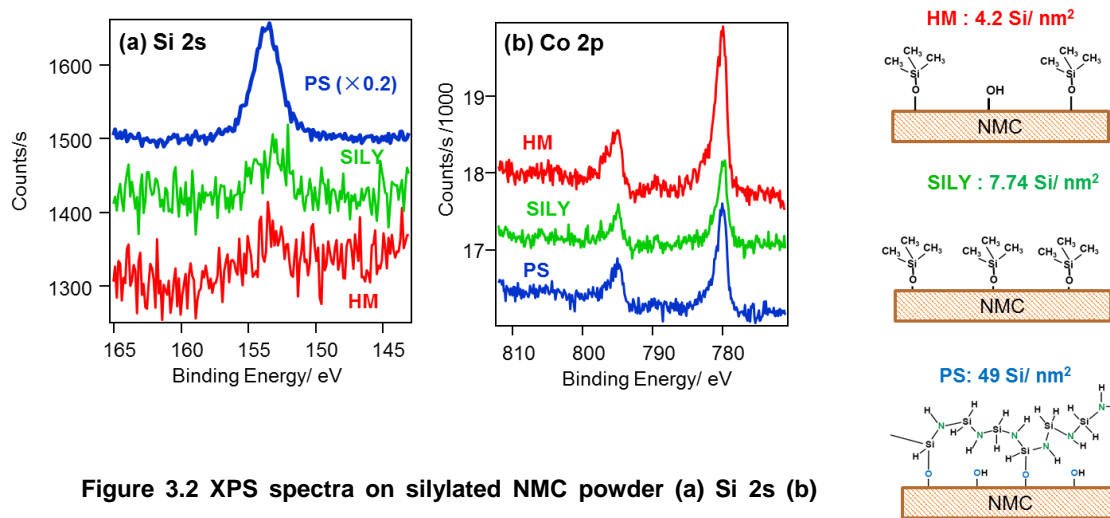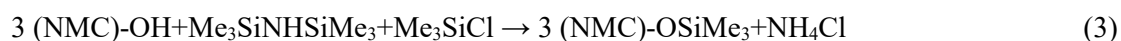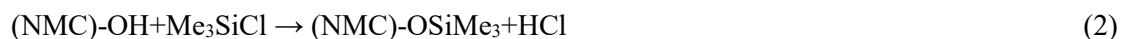
Figure 3.2 XPS spectra on silylated NMC powder (a) Si 2s (b) Co2p. The Si spectrum of PS sample was scaled by 0.2 for display purposes. The spectra were vertically shifted for demonstration.

and electron penetration depth, the Si coverage is estimated to be 4.2 atoms / nm^2 for HM, 7.7 atoms / nm^2 for SILY, and 49 atoms/nm^2 for PS. Details of this calculation can be found in the Appendix A2.1.

It is known that HMDS readily reacts with surface hydroxyls, forming trimethylsilyl(TMS) terminations.[27] For the HM sample, the reaction follows:

$$2 \text{ (NMC)-OH} + Me_3SiNHSiMe_3 \rightarrow 2 \text{ (NMC)-OSiMe}_3 + NH_3 \tag{1}$$

In preparation of SILY sample, the degree of silylation was improved with the addition of chlorotrimetheylsilane and the application of elevated temperature and neat reagents. In addition to the reaction in Eq. (1), the following reactions also happen:

$$\text{(NMC)-OH} + Me_3SiCl \rightarrow \text{(NMC)-OSiMe}_3 + HCl \tag{2}$$

$$3 \text{ (NMC)-OH} + Me_3SiNHSiMe_3 + Me_3SiCl \rightarrow 3 \text{ (NMC)-OSiMe}_3 + NH_4Cl \tag{3}$$

The PS sample was used to demonstrate the performance of a crosslinked with similar functional groups to compare with SILY and HM. The NMC was wrapped with polysilazane, and the schematic structure can be found in Fig. 3.2. Based on the coverage estimation, PS has the highest surface coverage of trimethylsilyl (TMS) groups among the three samples.

3.3.1.2 Electrochemical performance of silylated cathodes

Fig. 3.3 demonstrates the cycle performance of HM, SILY, PS, and untreated NMC. Silylation treatment significantly improved the discharge capacity and cycle retention. After two formation cycles, the starting 1C discharge capacity was 156mA.h/g (Untreated), 165mA.h/g (HM), 165mA.h/g (SILY), and 159mA.h/g (PS) respectively. Over the course of 100 cycles, untreated sample shows a capacity decay of 0.41 mAh.g^{-1} per cycle. The rate of capacity decay of silylated cathodes follows: PS (0.13 mAh.g^{-1}/cycle) < SILY (0.17 mAh.g^{-1}/cycle) < HM (0.29 mAh.g^{-1}/cycle). One can conclude that the capacity retention improves as the surface coverage increases. The slowest decay rate is observed of PS
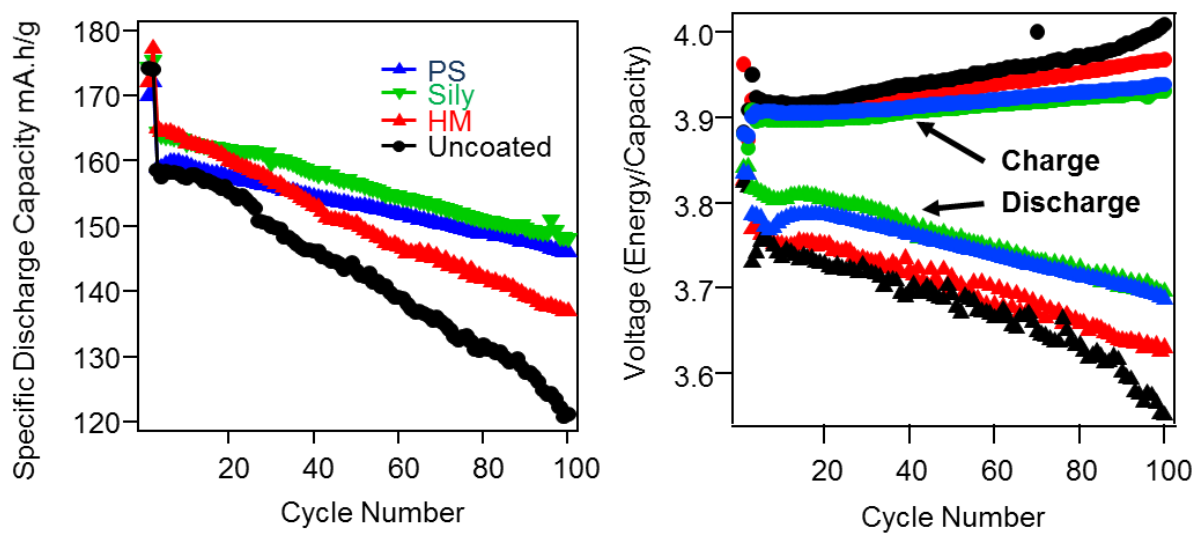
Figure 3.3 Comparison of electrochemical performance of HM, SILY, PS with performance of untreated NMC (a) Discharge capacity (b) Average operational capacity over cycles. The cells were tested between 3 V and 4.3 V, and the results were the average of triplicate cells.

sample, which is 67% slower than untreated NMC. During the 100th cycle, the average discharge capacity follows: SILY (148 mAh.g^{-1}) > PS (146 mAh.g^{-1}) > HM (137mAh.g^{-1}) > Untreated (117mAh.g^{-1}). The highest capacity is observed of SILY sample, which demonstrates 27% higher capacity than untreated sample.

In view of the overall electrochemical performance, silylated cathodes possess both higher capacity and higher capacity retention compared with untreated cathode. Between SILY and PS, it is difficult to ascertain which performs better: SILY shows slightly higher capacity after 100 cycles, while PS shows slightly higher capacity decay. In fact, the capacity retention of PS and SILY becomes quite comparable at the tail of the 100 cycles. Calculation based on 80th to 100th cycle demonstrates that both PS and SILY have a capacity drop rate around 0.14 mA.h/g. Overall, the cycle performance follows: PS≈SILY > HM > Untreated. That is a consistent order with surface coverage, but increase of TMS coverage from 7.7 atoms/nm^2 (SILY) to 49 atoms/nm^2 (PS) does not bring significant further performance improvement.

Fig. 3.3b examines the average operational voltage during charge and discharge. The operational voltage was calculated by dividing the charge/discharge energy by charge-discharge capacity, as adapted from literature procedures.[30] The voltage continuously increases over repeated charge-discharge and the discharging voltage shifts down. That is due to continuous build-up of cell impedance and fatigues developed within the active material. Previous study illustrates that voltage drop observed for a layered NMC material is almost entirely due to IR drop.[30] Upon surface silylation, significant decrease of IR drop is evidenced by lowered charge voltage and increased discharge voltage. The order of IR drop follows: PS ≈ SILY < HM < Untreated. This is clearly linked to the observed cycle retention in Fig. 3.3a. Since all samples are cycled within the same 3 V to 4.3 V voltage window, smaller IR drop on surface leads to less thermal loss and wider voltage window "felt" by the NMC active material.

Those can straightforwardly explain the observed IR drop-capacity correlation.

3.3.1.3 Electrochemical impedance spectroscopy

Reduced IR drop can be further linked to reduced charge-transfer impedance at the cathode-electrolyte interface. Electrochemical impedance spectra were collected both before and after cycling to study the interfacial charge-transfer properties. Fig. 3.4 compares the Nyquist plots of NMC-lithium half cells. In the high frequency region to the left, the spectra are composed of one to two semicircles, which correpond to interfacial charge-transfer processes, including double layer capacitance, charge-transfer resistance and RC associated with SEI and CEI layer.[23, 31] In the high frequency region in Fig. 3.4a and Fig. 3.4c, the spectra are dominated by an inclined line at around 45˚, which is associated with Warburg impedance.[32] The Warburg impedance represents ion diffusion inside the active particles. The magnitude of charge-transfer resistance and Warburg impedance depends on the cell voltage[9], and that is why semicircle diameter differs significantly between charged and discharged battery. In Fig. 3.4b, the Warburg region is not identifiable within the experimental frequency window, and we only detect the charge-transfer resistances.

From Fig. 3.4a, one can conclude that the three silylated samples have less charge-transfer impedance across the interface. This observation is consistent with the IR drop analysis in previous session. Fig. 3.4a was obtained before any electrochemical cycling was conducted. Since CEI formation takes place over the process of charge-discharge cycles, little CEI is expected to have formed in a freshly-assembled coin cell. Therefore, the reduced impedance indicates unique function of the Si-containing coatings in assisting lithium-ion transport across the interface. Fig. 3.4b and 4c were taken after some galvanostatic cycling. After the first charging process (0.5 cycles), the three silylated samples continue to demonstrate reduced charge-transfer impedance that is around 10Ω lower than untreated
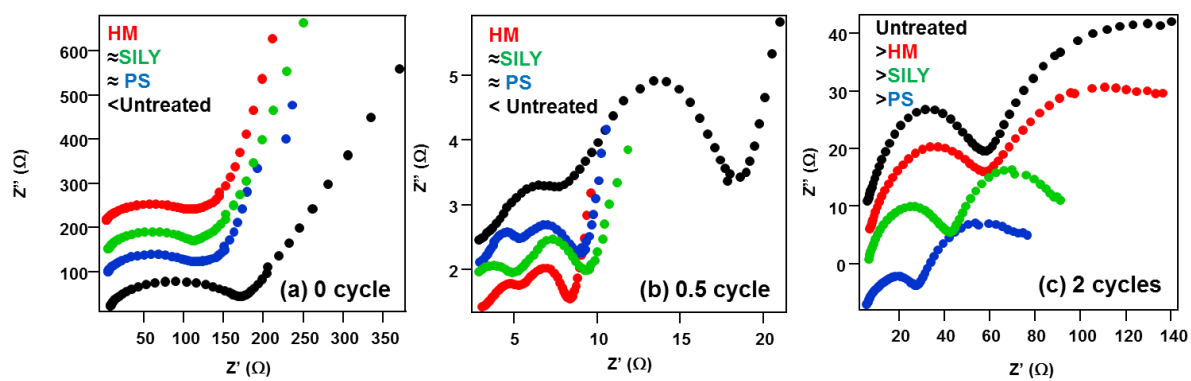
Figure 3.4 Impedance spectra of silylated and untreated NMC (a) before cycling at 3.0 V (b) after first C/10 charging at 4.3V (c) after two C/10 formation cycles at 3.6 V
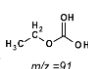
case. There no observable differences among the PS, SILY and HM samples. After two C/10 formation

cycles, the spectra in Fig. 3.4c start to demonstrate a coverage-impedance correlation. The order of

charge-transfer impedance follows: PS<SILY<HM. As coating coverage increases, the lithium-ion

transfer kinetics improves. The appearance of this correlation is partially attributed to the CEI formation

process - after two formation cycles, CEI layer forms at a detectable quantity, and one would expect a

impedance-surface coverage correlation if the amount of CEI decreases with the increasing surface

coverage. Overall, impedance analysis demonstrates possible dual functions of the Si-containing

coatings: facilitation of interfacial lithium-ion transport with the help of the organic moieties, and

suppression of CEI formation through surface protection, which scales with TMS coverage. Certainly,

the latter is to be further testified with careful CEI formation and surface reactivity evaluations.

3.3.1.4 Surface reactivity evaluation with thermal mass spectrometry

Fig. 3.5 quantifies the thermally-induced gas-phase decomposition products of electrolyte when in

contact with silylated and untreated NMC. The electrolyte contains EC/DEC with 1M $LiPF_6$. Fragments

of electrolyte decomposition products were detected *real-time* at 35, 50, 75, 100, 125 and 150 ˚C. Fig.

3.5a and Fig. 3.5b demonstrate the thermal mass spectra and detailed assignment of peaks. Each peak

in the mass spectra quantifies a decomposition product or its fragments.

In order to compare the reactivity of treated and untreated NMC material, the activation energy was

estimated from Arrenehnius equation:

$$\ln(k) = -\frac{E_a}{R}\left(\frac{1}{T}\right) + \ln(A)$$

Where T was taken as the temperature at which the spectra were collected and k as the detected

quantity (in unit of pressure) of m/z=91 fragment ($\underset{m/z=91}{}$). That fragment was chosen because

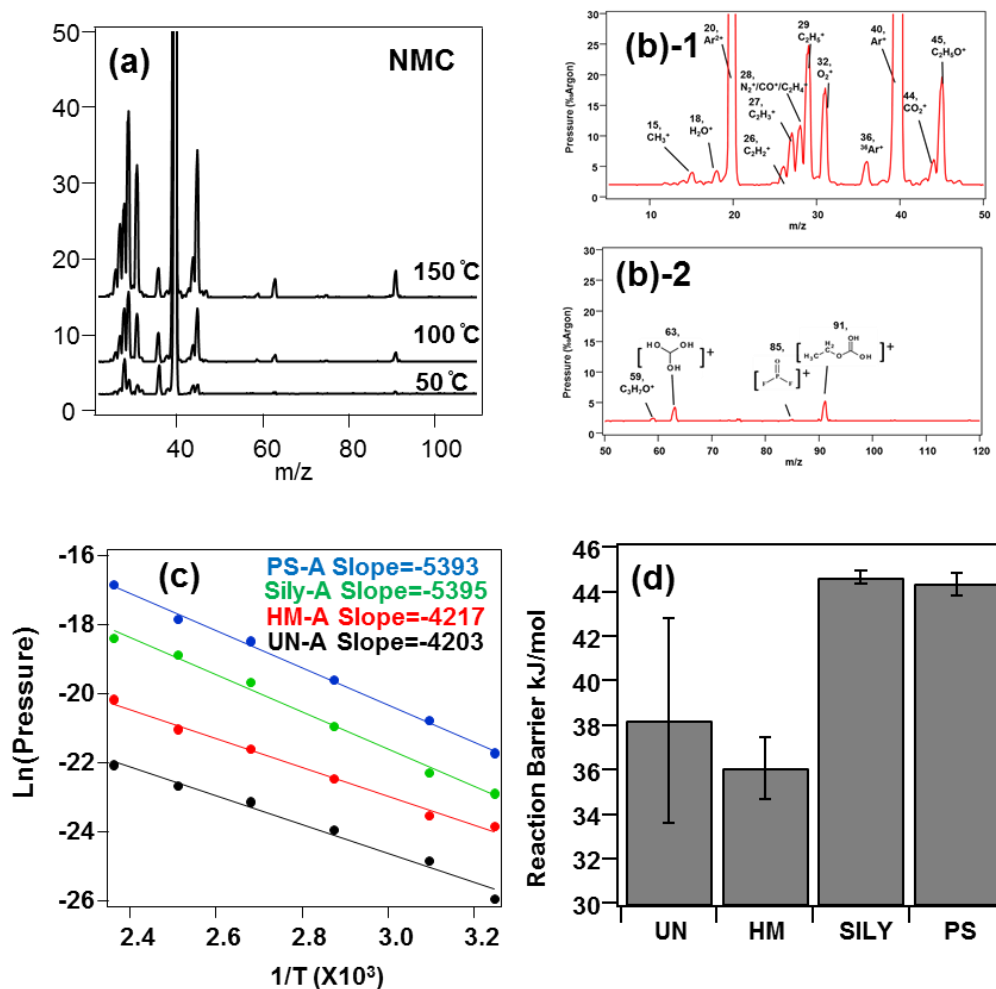fragments below m/e=44 were mostly residues of air,[29] or otherwise non-specific to a certain

Figure 3.5 Thermal mass spectrometry characterization of gas-phase decomposition products. (a) Example thermal mass spectra tested at 50 ℃, 100 ℃ and 150 ℃ in the presence of 0.05g Untreated NMC. The spectra were normalized to Ar signal, and vertically shifted for display. (b) Peak Assignment (c) Ln (Pressure of m/e=91 peak) vs. 1/T curves for estimation of activation energy (d) Estimated activation barrier with error bars obtained from triplicate measurement.

decomposition product of electrolyte. Among the peaks above m/e=44, the m/e=91 peak was highest in intensity. Fig. 3.5c displays the ln (k) vs. 1/T curves for the m/e=91 fragment. PS and SILY samples have higher slopes than HM and untreated samples, indicating higher reaction barrier. The slopes of triplicate measurements are quantified in Fig. 3.5d. The average reaction barriers E_a are 44.3 ($\pm$0.5) kJ/mol for PS and 44.6 ($\pm$0.3) kJ/mol for SILY, higher than the 36.0 ($\pm$1.4) kJ/mol and 38.2 ($\pm$4.6) kJ/mol for HM and untreated NMC. That means that the HM sample, with relatively low surface coverage, demonstrates similar reaction barrier with untreated material, and the treatment does not stabilize the cathode-electrolyte interface. As the coverage increases, SILY and PS has similar high barrier to electrolyte decomposition, stabilizing the cathode-electrolyte interface. Going from SILY to PS, the improvement of surface coverage does not further reduce the electrolyte decomposition reactivity. This observation can explain observed performance similarity between SILY and PS. It also indicates existence of a maximally-effective coverage, and that cross-linking is not a necessity in achieving good surface protection.

3.3.1.5 XPS analysis of cathode-electrolyte interphase (CEI) formation

To examine the extent of electrolyte decomposition during electrochemical cycling, XPS spectra of cathodes were collected after 100 cycles. Fig. 3.6 shows the F (1s) and P (2p) regions. The F spectra are composed of two features: the higher binding energy peak at around 688eV is mainly attributed to PVDF binder, and the peak at 685eV is assigned to LiF, decomposition product of $LiPF_6$ salts. Significant amount of LiF is detected on both silylated and untreated NMC cathodes, and the quantities are not statistically different (Fig. 3.6b). In the P (2p) region, the relatively broad peaks are assigned to $LiPF_xO_y$ and $LiPO_x$, which are decomposition products of $LiPF_6$ salts. In Fig. 3.6c, SILY and PS samples
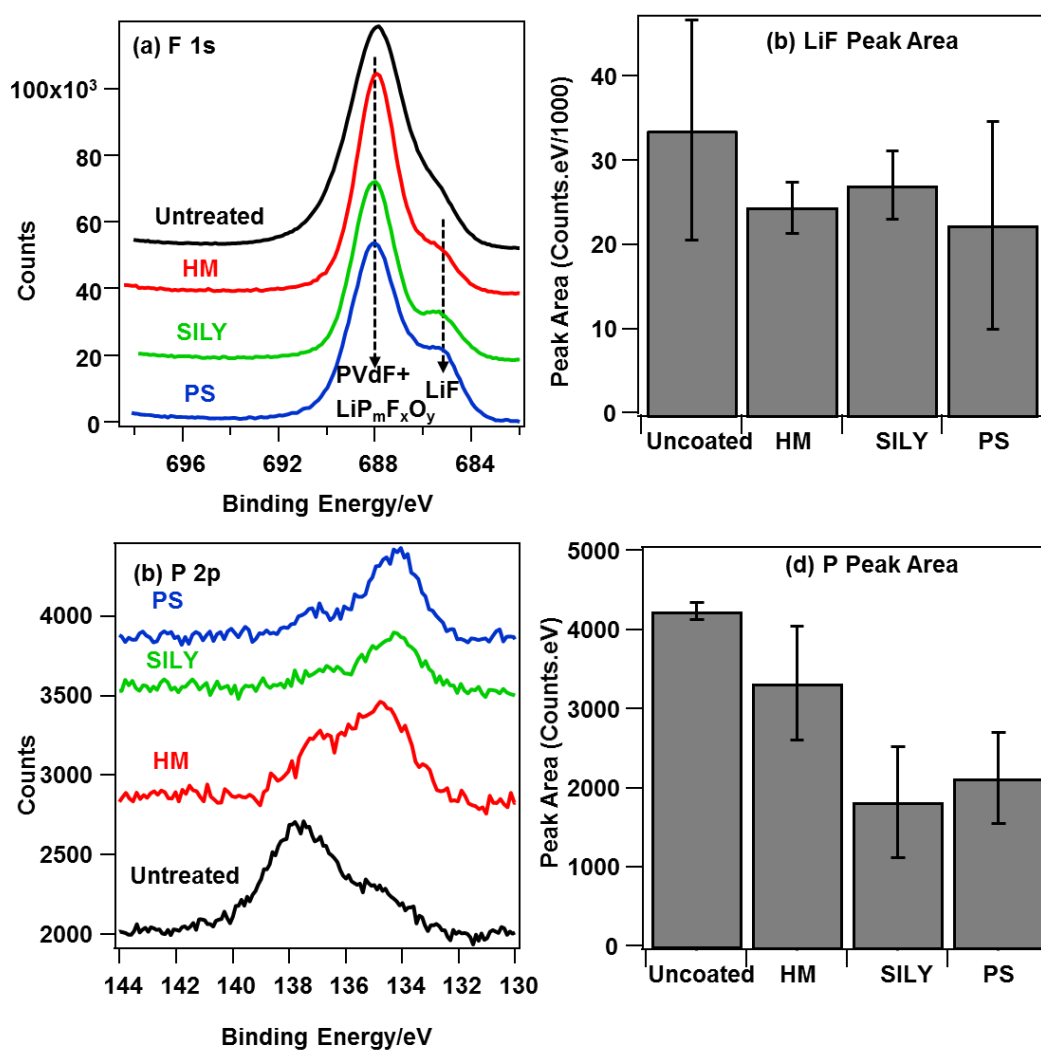
Figure 3.6 XPS spectra of cathodes after 100 cycles (a) Comparison of representative F 1s spectra (b) Average peak area of F 685 eV peak (assigned to LiF) (c) Representative P 2p spectra (d) Average peak area of P 2p peaks (sum of peak area at 138 and 134 eV)

demonstrate lower P (2p) peak area than HM and untreated samples. Fig. 3.6d summarizes the total peak area of P-containing CEI. The quantities of P-containing CEI follows: Untreated > HM > SILY ≈ PS. As surface coverage goes up, the quantity of P-containing CEI decreases. The similar CEI quantities on SILY and PS sample is in good agreement with the previous thermal MS results. HM also demonstrates slight less CEI than untreated sample after long cycling.

The C (1s) and O (1s) spectra are shown in Fig. A2.2. It is not convincing to conclude CEI formation trends based on C and O spectra because, in addition to CEI growth, the C-containing groups in the silylated coating itself and surface water/hydroxyl content can also lead to changes in the C and O region.

3.3.1.6 ICP analysis of transition metal dissolution

Transition metal dissolution oftentimes accompanies side reactions on cathode surface.[33] ICP analysis of transition metal elements in electrolyte and anode is another good way to analyze cathode-electrolyte reactivity. Fig. 3.7 quantifies the Co and Mn dissolution after 20 charge-discharge cycles Co dissolution is quantified in Fig. 3.7a. The amount of dissoluted Co follows: UN≈HM>SILY≈PS. Fig. 3.7b quantifies Mn dissolution. The overall trend agrees with results from Co dissolution. . Ni is not used for dissolution study because the experimental procedure involves soaking of SS coin cell parts which also contains nickel. Overall, the ICP analysis is consistent with both XPS and thermal MS in regard of the coverage-reactivity correlation. Low-coverage HM sample is not quite protective of cathode surface; SILY and PS demonstrate significantly improved interfacial stability and, among themselves, performance similarity despite the significantly different TMS coverage.

Overall, results in 3.1 leads to several key observations regarding the silylated cathodes: First, the coverage-performance correlation can be rationalized by surface protection mechanism.
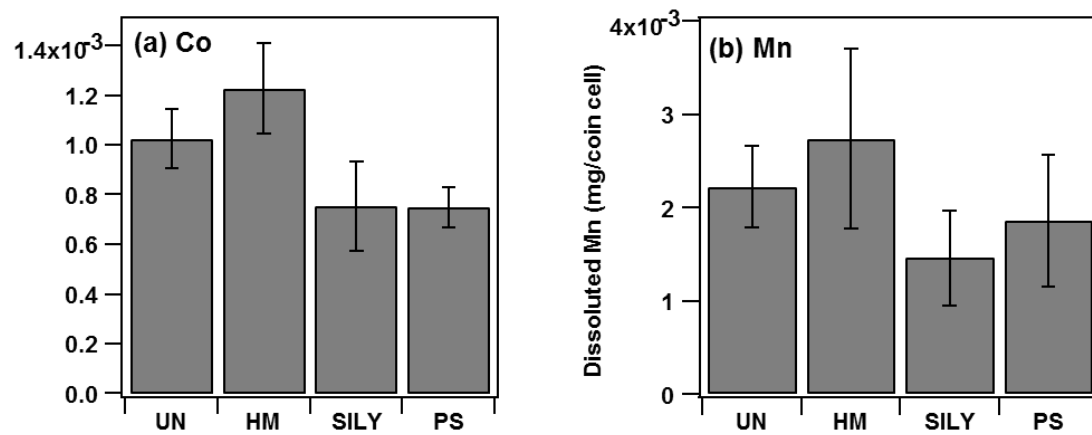
Figure 3.7 ICP results on Co and Mn dissolution

As coverage increases, degree of interfacial side-reactions goes down; Second, threshold of effective coverage is observed. From non-crosslinking SILY sample with monolayer coverage to crosslinked PS sample, significant improvement of TMS-coverage leads to no further performance improvement; Third, the observed facilitation of interfacial lithium-ion transport is not purely a natural outcome of suppressed CEI formation, but also a result of coatings' own properties. This is supported because lower impedance is observed before major CEI formation, and of HM sample which shows insignificant or no surface stabilization effect. One can conclude that the 20% to 30% performance elevation comes from two factors: reduced interfacial reactivity (true for SILY and PS) and charge-transfer facilitation with the grafted organic moieties (true for HM, SILY and PS).

3.3.2 Discussion on Working Mechanism of Silylated Cathodes

Summarizing the above observations, it is desirable to further track down molecular properties of Si-containing coatings that lead to the suppressed electrolyte decomposition and facilitated charge-transfer. Those characteristics can be used to shed light upon desirable coating design features. The following discussion explores a few most probable working mechanisms in our perspectives.

3.3.2.1 Hydrophobicity modulation that modifies cathode-electrolyte interaction

In Fig. 3.4, we demonstrate that the silylation treatment enhances interfacial charge-transfer. In previous literature, Abe et al. demonstrated that desolvation of lithium-ion is the rate-limiting step of the interfacial lithium-ion transfer at graphite-electrolyte interface.[34] Further, it is shown the ion transfer is affected by the nature of SEI layer formed.[35] To assist the interfacial ion transfer, Christopher et al. demonstrated that copper coating on graphite can assist the desolvation of Li from Li-PC.[36] We believe that one function of the grafted TMS groups is to assist the desolvation of lithium-ion and thus to
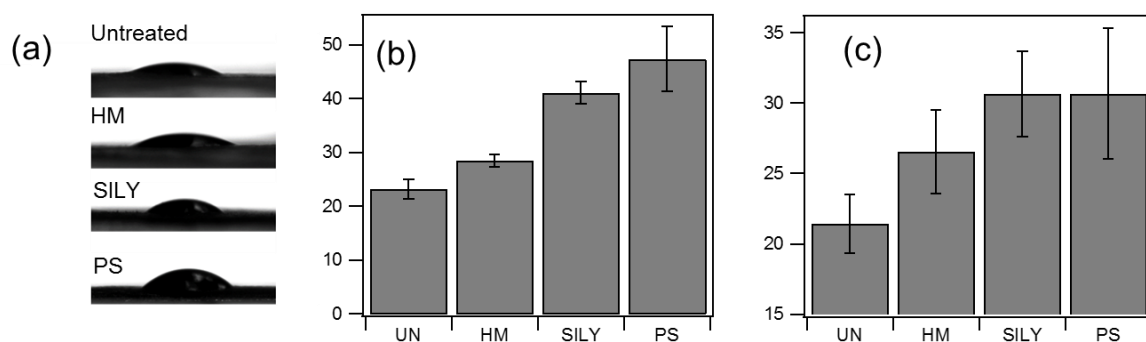
Figure 3.8 Contact angle measurement (a) Sessile droplets of water on indium-supported-powder substrate (b) Water contact angle on indium-supported-powder substrate (c) EC/DEC contact angle on composite NMC film (angle based of pendant droplet)

facilitate interfacial charge-transfer.

To identify the difference between silylated NMC-electrolyte interactions and the bare NMC-electrolyte interaction, contact angle measurement was conducted to examine the impact of hydrophobicity by different treatment. Fig. 3.8 demonstrates the results from flat surface of pressed NMC powder into indium foil. As demonstrated in Fig. 3.8b, the water contact angle increases as TMS coverage goes up, and the surface becomes more hydrophobic. Similar measurement on composite cathode film demonstrates a consistent trend, and the results can be found in Fig. A2.3. In previous literature, HMDS treatment was reported to produce hydrophobic surfaces[37-38], and our result is consistent with that.

In battery running conditions, the electrodes are in contact with EC/DEC electrolyte. An attempt to evaluate EC/DEC miscibility with treated surface was made by measuring DEC/DEC contact angle. Averaged contact angle indicates that the treated surface is more EC/DEC-phobic as coverage goes up.

In electrolyte, lithium-ions exist in the form of $[Li(EC)_n]^+$ or $[Li(EC)_n(DEC)_m]^+$ complexes[39-40]. As the surface hydrophobicity and EC/DEC-phobicity increase, it becomes more difficult for the solvent molecules to migrate close to the surface, while lithium-ion intercalation can still be driven by the electric field. If that happens, a hydrophobic surface can motivate earlier desolvation of lithium-ion from the li-solvent complexes. The TMS group may work as a molecular shuttle that helps lithium migration across the interface. Bad reactors in the electrolyte such as HF can also be repelled from the surface, leading to reduced interfacial reactivity.

The reduced IR drop and improved ion transport kinetics are well justified under this mechanism. However, the performance similarity between SILY and PS is still not very well explained. For an absolute hydrophobicity-reactivity correlation, PS is expected to have higher performance than SILY

due to the higher hydrophobicity. Considering results in Fig. 3.8, some possible explanations include:

(a) EC/DEC-phobicity is actually similar while hydrophobicity differs between SILY and PS. Error bar in Fig. 3.8c is big enough that one cannot conclude about the degree of EC/DEC-phobicity of PS; (b) Hydrophobicity modulation is not the only mechanism that contributes to the observed coverage-performance relationship. Other factors also play a role in tuning the cathode-electrolyte interaction.

3.3.2.2 HF Scavenging

In the work of Wu et al., the authors propose that the HMDS molecules in electrolyte react with HF following the reaction: [28]

$$(CH_3)_3SiN(CH_3)Si(CH_3)_3 + HF \rightarrow [(CH_3)_3SiNH(CH_3)Si(CH_3)_3]^+F^-$$
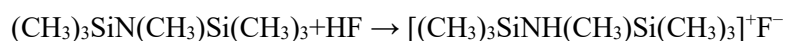
Through HF removal, further transition metal leaching and other side reactions can be suppressed. In the case of silylated cathode, the TMS groups are chemically grafted to NMC, and it is not clear whether the reactivity with HF retains. The quantity of HMDS used in the published article is 2 vol.% of electrolyte, which is significantly higher compared with the amount we applied during cathode grafting (calculation found in Appendix A2.5). To testify the possible correlation between HF scavenging and surface protection, control experiments were conducted where equal amount of HMDS as grafted on the HM or SILY sample was added directly to the electrolyte (calculation of dosage described in Appendix A2.5). If TMS reaction with HF is the main mechanism, one can expect similar improvement by putting HMDS directly in electrolyte. The schematics to the left of Fig. 3.9 illustrates the interaction of grafted / ungrafted HMDS with HF. It is assumed that a TMS group on free HMDS in electrolyte is at least equally reactive with HF compared with a TMS group grafted on NMC. This is a reasonable assumption considering that the Si-O bond strength is expected to be stronger than Si-N bond strength, and that free-standing molecules have less steric hindrance.

Fig. 3.9 examines the cycling performance of the in-electrolyte vs. grafted HMDS. At the same dosage, HMDS-containing electrolyte is not nearly as effective as direct HMDS grafting. This clearly distinguishes working mechanism of Si-containing coatings from Si-containing electrolyte. Consequently, HF scavenging is not considered the main working mechanism of silylated cathodes.

Fig. 3.10 examines the CEI species formed when HMDS is used as an HF scavenger in electrolyte. The 685 eV LiF peak is quite small on an electrode cycled with free-standing HMDS. The result in Li(1s) region agrees with that of the F(1s) region. Since HF is a main reactant leading to formation of LiF, this conclusion agrees with HF scavenging mechanism when HMDS is applied in electrolyte. On contrary, both untreated and silylated cathodes demonstrate substantial amount of LiF formation, which further supports that the HF scavenging is not the main working mechanism for silylated cathodes.

3.3.2.3 Surface hydroxyl/water removal with HMDS

It is well-recognized that moisture is detrimental to battery performance and can accelerate decomposition of electrolytes.[41] HMDS is known for its high reactivity with water and surface hydroxyls.[27] It is therefore important to understand whether the suppressed reactivity at high coverage bares any correlation with the surface hydroxyl concentrations.

The assumption of a general surface hydroxyl concentration-reactivity correlation is first validated experimentally, and the result is shown in Appendix A2.6. Fig. 3.11a displays the FTIR spectra of HM, SILY and PS sample. The spectra were referenced to KBr that contains untreated NMC powder, and magnitude of the broad peak in the range of 3300- 3600 cm^{-1} represents the difference in hydroxyl concentrations between treated and untreated. HM and PS sample show positive OH peaks, indicating higher amount of surface hydroxyls than untreated material. This is somewhat counter-intuitive because the reaction of HMDS with NMC involves grafting through hydroxyl group binding. It is not clear what
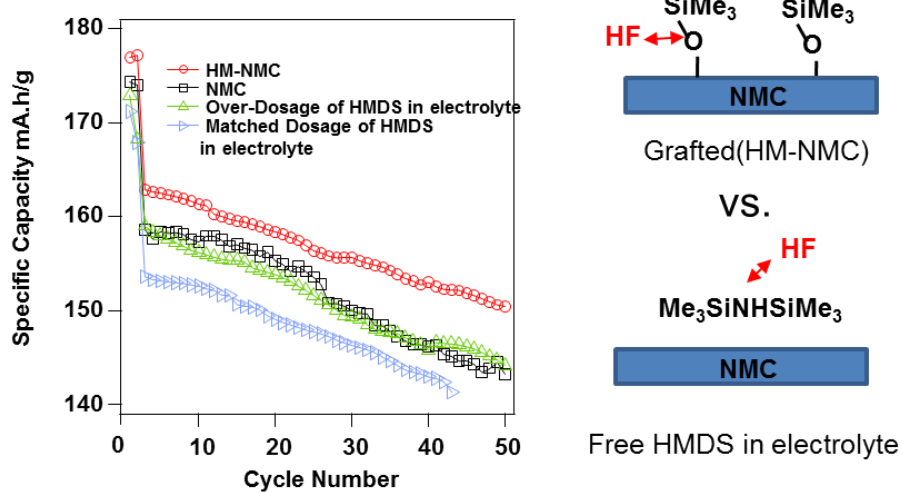
Figure 3.9 Cycle performance of HM-NMC (red), NMC (black) and NMC cycled with different dosage of HMDS in electrolyte (green and blue)
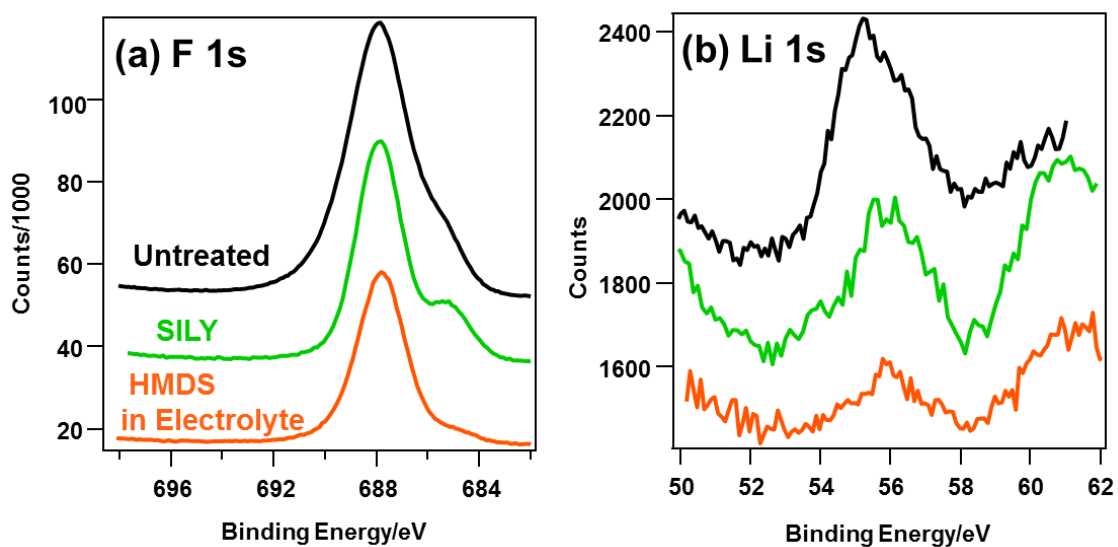
Figure 3.10 XPS spectra of cathodes cycled in HMDS-containing electrolyte. Green and black curves are results from SILY and Untreated electrode for comparison. The spectra have been vertically shifted for display.
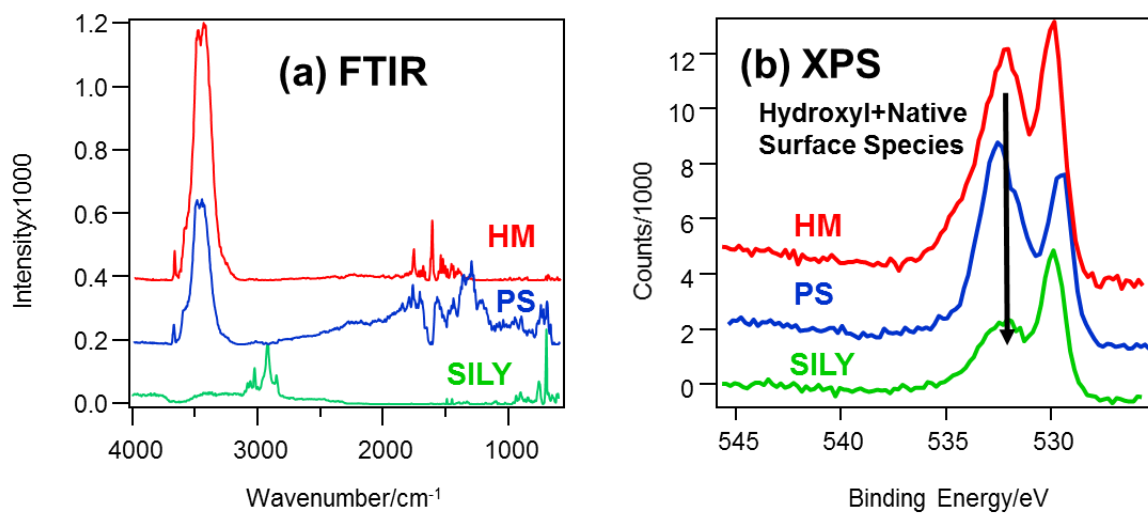
Figure 3.11 (a) Diffused reflectance FTIR spectra of treated NMC powder collected at 0.1%w in KBr (b) O 1s XPS spectra of treated NMC powder

reactions lead to this change. SILY sample demonstrates the lowest amount of hydroxyls among the three treated samples. There is no detectable peak in the range of 3300-3600 cm^{-1}. The FTIR results are further supported by XPS results in the O 1s region. In Fig. 3.11b, the O region is composed of two peaks: the peak at 529 eV is assigned to oxygen in NMC lattice, and the peak around 532 eV is assigned to surface oxygen-containing species which include hydroxyls. SILY sample demonstrates the lowest intensity of the hydroxyl-originated peak among the three samples. Combined FTIR and XPS characterization places the hydroxyl concentration in the order of SILY< PS ≈ HM.

Clearly, the order of hydroxyl concentration is not the same with electrochemical performance or cathode-electrolyte reactivity. However, the comparison between SILY and PS leads to some interesting insight on the interplay between coverage and surface protectivity. With SILY sample, low hydroxyl concentration is achieved at medium coverage of TMS groups; with PS sample, less effective hydroxyl blockage is observed with high surface coverage. Previous electrochemical/reactivity evaluation shows that PS is not more protective than SILY despite the improved surface coverage. A plausible explanation is that the SILY treatment targets the more reactive surface sites (hydroxyls) other than generally covers the surface (PS). Thus, one can rationalize the SILY and PS performance similarity with following theory: while the reactivity decreases with increasing hydrophobicity, the SILY sample demonstrates better than expected performance due to effective removal of surface hydroxyls.

3.4 Conclusion

In this work, we investigated silylation treatment of layered LiNi$_{0.5}$Mn$_{0.3}$Co$_{0.2}$O$_2$ cathode, and demonstrated up to 27% higher capacity (SILY) and 67% slower capacity decay per cycle (PS) over the course of 100 charge-discharge cycles. EIS demonstrates that the grafted organic moieties can facilitate charge-transfer across the interface. Analytical investigation with XPS, thermal mass spectrometry and

ICP illustrates an overall surface coverage-reactivity-performance correlation, and a threshold of this correlation is observed between SILY (7.9 Si/nm^2) and PS (49 Si/nm^2) sample. It is believed that silylation benefits performance through a two-fold mechanism: facilitation of interfacial charge-transfer is achieved by facilitation of lithium-ion desolvation with the hydrophobic TMS moieties; the surface protection effect can be due to combined hydroxyl removal and hydrophobicity modulation, but not HF scavenging. The benefits of Si-containing coatings provide unique opportunities to improve cathode properties with small, non-crosslinking organic molecules.

Acknowledgement

3.5 Reference

1. Ohzuku, T.; Makimura, Y., Layered lithium insertion material of $LiCo_{1/3}Ni_{1/3}Mn_{1/3}O_2$ for lithium-ion batteries. *Chemistry Letters* **2001,** (7), 642-643.

2. Hwang, B. J.; Tsai, Y. W.; Carlier, D.; Ceder, G., A combined computational/experimental study on $LiNi_{1/3}Co_{1/3}Mn_{1/3}O_2$. *Chemistry of Materials* **2003,** *15* (19), 3676-3682.

3. Kim, J. M.; Chung, H. T., The first cycle characteristics of Li $Ni_{1/3}Co_{1/3}Mn_{1/3}O_2$ charged up to 4.7 V. *Electrochimica Acta* **2004,** *49* (6), 937-944.

4. Choi, J.; Manthiram, A., Investigation of the irreversible capacity loss in the layered $LiNi_{1/3}Mn_{1/3}Co_{1/3}O_2$ cathodes. *Electrochemical and Solid State Letters* **2005,** *8* (8), C102-C105.

5. Wang, J.; Yao, X. Y.; Zhou, X. F.; Liu, Z. P., Synthesis and electrochemical properties of layered lithium transition metal oxides. *Journal of Materials Chemistry* **2011,** *21* (8), 2544-2549.

6. Dolotko, O.; Senyshyn, A.; Muhlbauer, M. J.; Nikolowski, K.; Ehrenberg, H., Understanding structural changes in NMC Li-ion cells by in situ neutron diffraction. *Journal of Power Sources* **2014,** *255*, 197-203.

7. Makimura, Y.; Ohzuku, T., Lithium insertion material of $LiNi_{1/2}Mn_{1/2}O_2$ for advanced lithium-ion batteries. *Journal of Power Sources* **2003,** *119*, 156-160.

8.   Lu, C. H.; Shen, B. J., Electrochemical characteristics of $LiNi_{1/3}Co_{1/3}Mn_{1/3}O_2$ powders prepared from microwave-hydrothermally derived precursors. *Journal of Alloys and Compounds* **2010,** *497* (1-2), 159-165.

9.   Shaju, K. M.; Rao, G. V. S.; Chowdari, B. V. R., Influence of Li-ion kinetics in the cathodic performance of layered $Li(Ni_{1/3}Co_{1/3}Mn_{1/3})O_2$. *Journal of the Electrochemical Society* **2004,** *151* (9), A1324-A1332.

10.   Li, C.; Zhang, H. P.; Fu, L. J.; Liu, H.; Wu, Y. P.; Ram, E.; Holze, R.; Wu, H. Q., Cathode materials modified by surface coating for lithium ion batteries. *Electrochimica Acta* **2006,** *51* (19), 3872-3883.

11.   Wu, Y.; Manthiram, A., Effect of surface modifications on the layered solid solution cathodes (1-z) Li $Li_{1/3}Mn_{2/3}$ O_2-(z) Li $Mn_{0.5y}Ni_{0.5y}Co_{2y}$ O_2. *Solid State Ionics* **2009,** *180* (1), 50-56.

12.   Kim, Y. J.; Kim, H.; Kim, B.; Ahn, D.; Lee, J. G.; Kim, T. J.; Son, D.; Cho, J.; Kim, Y. W.; Park, B., Electrochemical stability of thin-film $LiCoO_2$ cathodes by aluminum-oxide coating. *Chemistry of Materials* **2003,** *15* (7), 1505-1511.

13.   Wise, A. M.; Ban, C. M.; Weker, J. N.; Misra, S.; Cavanagh, A. S.; Wu, Z. C.; Li, Z.; Whittingham, M. S.; Xu, K.; George, S. M.; Toney, M. F., Effect of Al_2O_3 Coating on Stabilizing $LiNi_{0.4}Mn_{0.4}Co_{0.2}O_2$ Cathodes. *Chemistry of Materials* **2015,** *27* (17), 6146-6154.

14.   Jung, Y. S.; Cavanagh, A. S.; Riley, L. A.; Kang, S. H.; Dillon, A. C.; Groner, M. D.; George, S. M.; Lee, S. H., Ultrathin Direct Atomic Layer Deposition on Composite Electrodes for Highly Durable and Safe Li-Ion Batteries. *Advanced Materials* **2010,** *22* (19), 2172-2176.

15.   Holze, R.; Fu, L. J.; Liu, H.; Li, C.; Wu, Y. P.; Rahm, E.; Wu, H. Q., Surface modifications of electrode materials for lithium ion batteries. *Solid State Sci. (France)* **2006,** *8* (2), 113-128.

16.   Li, F. S.; Wu, Y. S.; Chou, J.; Winter, M.; Wu, N. L., A Mechanically Robust and Highly Ion-Conductive Polymer-Blend Coating for High-Power and Long-Life Lithium-Ion Battery Anodes. *Advanced Materials* **2015,** *27* (1), 130-137.

17. Kang, I. S.; Lee, Y. S.; Kim, D. W., Improved Cycling Stability of Lithium Electrodes in Rechargeable Lithium Batteries. *Journal of the Electrochemical Society* **2014,** *161* (1), A53-A57.

18.   Huang, Y. H.; Park, K. S.; Goodenough, J. B., Improving lithium batteries by tethering carbon-coated $LiFePO_4$ to polypyrrole. *Journal of the Electrochemical Society* **2006,** *153* (12), A2282-A2286.

19.   Cherkashinin, G.; Nikolowski, K.; Ehrenberg, H.; Jacke, S.; Dimesso, L.; Jaegermann, W., The stability of the SEI layer, surface composition and the oxidation state of transition metals at the electrolyte-cathode interface impacted by the electrochemical cycling: X-ray photoelectron spectroscopy investigation. *Physical Chemistry Chemical Physics* **2012,** *14* (35), 12321-12331.

20.   Ying, J. R.; Wan, C. R.; Jiang, C. Y., Surface treatment of $LiNi_{0.8}Co_{0.2}O_2$ cathode material for lithium secondary batteries. *Journal of Power Sources* **2001,** *102* (1-2), 162-166.

21. Shen, D. D.; Zhang, D. W.; Wen, J. W.; Chen, D. M.; He, X. J.; Yao, Y. J.; Li, X. L.; Duger, C., $LiNi_{1/3}Co_{1/3}Mn_{1/3}O_2$ coated by Al_2O_3 from urea homogeneous precipitation method: improved Li storage performance and mechanism exploring. *Journal of Solid State Electrochemistry* **2015,** *19* (5), 1523-1533.

22. Verdier, S.; El Ouatani, L.; Dedryvere, R.; Bonhomme, F.; Biensan, P.; Gonbeau, D., XPS study on Al_2O_3- and $AlPO_4$-coated $LiCoO_2$ cathode material for high-capacity li ion batteries. *Journal of the Electrochemical Society* **2007,** *154* (12), A1088-A1099.

23. Myung, S. T.; Izumi, K.; Komaba, S.; Sun, Y. K.; Yashiro, H.; Kumagai, N., Role of alumina coating on Li-Ni-Co-Mn-O particles as positive electrode material for lithium-ion batteries. *Chemistry of Materials* **2005,** *17* (14), 3695-3704.

24. Assresahegn, B. D.; Brousse, T.; Belanger, D., Advances on the use of diazonium chemistry for functionalization of materials used in energy storage systems. *Carbon* **2015,** *92*, 362-381.

25. Dalla Corte, D. A.; Gouget-Laemme, A. C.; Lahlil, K.; Caillon, G.; Jordy, C.; Chazalviel, J. N.; Gacoin, T.; Rosso, M.; Ozanam, F., Molecular grafting on silicon anodes: artificial Solid-Electrolyte Interphase and surface stabilization. *Electrochimica Acta* **2016,** *201*, 70-77.

26. Buqa, H.; Grogger, C.; Alvarez, M. V. S.; Besenhard, J. O.; Winter, M., Surface modification of graphite anodes by combination of high temperature gas treatment and silylation in nonaqueous solution. *Journal of Power Sources* **2001,** *97-8*, 126-128.

27. Hertl, W.; Hair, M. L., Reaction of hexamethyldisilazane with silica. *J. Phys. Chem.* **1971,** *75* (14), 2181-2185.

28. Wu, X. W.; Wang, Z. X.; Li, X. H.; Guo, H. J.; Zhang, Y. H.; Xiao, W., Effect of lithium difluoro(oxalato)borate and heptamethyldisilazane with different concentrations on cycling performance of $LiMn_2O_4$. *Journal of Power Sources* **2012,** *204*, 133-138.

29. Chen, X.; Usrey, M.; Pena-Hueso, A.; West, R.; Hamers, R. J., Thermal and electrochemical stability of organosilicon electrolytes for lithium-ion batteries. *Journal of Power Sources* **2013,** *241*, 311-319.

30. Bettge, M.; Li, Y.; Gallagher, K.; Zhu, Y.; Wu, Q. L.; Lu, W. Q.; Bloom, I.; Abraham, D. P., Voltage Fade of Layered Oxides: Its Measurement and Impact on Energy Density. *Journal of the Electrochemical Society* **2013,** *160* (11), A2046-A2055.

31. Sclar, H.; Kovacheva, D.; Zhecheva, E.; Stoyanova, R.; Lavi, R.; Kimmel, G.; Grinblat, J.; Girshevitz, O.; Amalraj, F.; Haik, O.; Zinigrad, E.; Markovsky, B.; Aurbach, D., On the Performance of $LiNi_{1/3}Mn_{1/3}Co_{1/3}O_2$ Nanoparticles as a Cathode Material for Lithium-Ion Batteries. *Journal of the Electrochemical Society* **2009,** *156* (11), A938-A948.

32. Chou, S. L.; Wang, J. Z.; Liu, H. K.; Dou, S. X., Rapid Synthesis of Li4Ti5O12 Microspheres as Anode Materials and Its Binder Effect for Lithium-Ion Battery. *Journal of Physical Chemistry C* **2011,** *115* (32), 16220-16227.

33. Fu, L. J.; Liu, H.; Li, C.; Wu, Y. P.; Rahm, E.; Holze, R.; Wu, H. Q., Surface modifications of electrode materials for lithium ion batteries. *Solid State Sci. (France)* **2006,** *8* (2), 113-128.

34. Abe, T.; Fukuda, H.; Iriyama, Y.; Ogumi, Z., Solvated Li-ion transfer at interface between graphite and electrolyte. *Journal of the Electrochemical Society* **2004,** *151* (8), A1120-A1123.

35. Yamada, Y.; Iriyama, Y.; Abe, T.; Ogumi, Z., Kinetics of Lithium Ion Transfer at the Interface between Graphite and Liquid Electrolytes: Effects of Solvent and Surface Film. *Langmuir* **2009,** *25* (21), 12766-12770.

36. Johnson, C. S.; Lauzze, K.; Kanakaris, N.; Kahaian, A.; Thackeray, M. M.; Amine, K.; Sandi-Tapia, G.; Hackney, S. A.; Rigney, R. O., *Electrochemical performance of Ni/Cu-metallized & carbon-coated graphites for lithium batteries*. Springer: Dordrecht, 2006; Vol. 229, p 357-376.

37. Kisler, J. M.; Gee, M. L.; Stevens, G. W.; O'Connor, A. J., Comparative study of silylation methods to improve the stability of silicate MCM-41 in aqueous solutions. *Chemistry of Materials* **2003,** *15* (3), 619-624.

38. Kartal, A. M.; Erkey, C., Surface modification of silica aerogels by hexamethyldisilazane-carbon dioxide mixtures and their phase behavior. *J. Supercrit. Fluids* **2010,** *53* (1-3), 115-120.

39. Jeong, S. K.; Inaba, M.; Iriyama, Y.; Abe, T.; Ogumi, Z., Surface film formation on a graphite negative electrode in lithium-ion batteries: AFM study on the effects of co-solvents in ethylene carbonate-based solutions. *Electrochimica Acta* **2002,** *47* (12), 1975-1982.

40. Fukushima, T.; Matsuda, Y.; Hashimoto, H.; Arakawa, R., Studies on solvation of lithium ions in organic electrolyte solutions by electrospray ionization-mass spectroscopy. *Electrochemical and Solid State Letters* **2001,** *4* (8), A127-A128.

41. Saharan, V.; Roberts, J.; Manev, V.; Chia, Y. H.; MacLean, G.; McMullen, S. R., Moisture-uptake by the positive active material from the casting solvent and the ambient environment. *Journal of Power Sources* **2005,** *146* (1-2), 809-812.

Chapter 4

Cell design for *in situ* Raman Mapping of Inhomogeneous

State-of-Charge Profiles in Lithium-ion Batteries

Reprinted with permission from Fang, S., Yan, M., Hamers, R. J., Cell design for *in situ* Raman

mapping of inhomogeneous state-of-charge profiles in lithium-ion batteries, submitted to *Journal of*

Power Sources

4.1 Introduction

Li-ion batteries are one of the most popular types of rechargeable batteries for portable electronics. Yet, a persistent problem limiting the use of lithium-ion batteries is the loss of capacity and consequent degradation of performance over the lifetime of the battery.[1-3] Recent studies show that the failure of battery cells is largely associated with inhomogeneous deterioration of the composite electrodes.[4-7] Uneven state-of-charge (SOC) distribution has been studied previously by calorimetry,[8] neutron diffraction,[4] Raman spectroscopy,[9-11] scanning transmission X-ray microscopy (STXM)[12] and soft X-ray emission spectroscopy.[13] The SOC inhomogeneity is believed to cause local overcharge or overdischarge[7, 10] and accelerate detrimental processes such as metal dissolution,[4] electrolyte decomposition,[9] and oxygen release from active materials.[14] In order to perform accurate failure analysis, we need proper spectroscopic tools with high spatial resolution and *in situ* visualization to capture the inhomogeneous material degradations in a working battery.

Raman spectroscopy is a useful tool for characterizing inhomogeneity in batteries because its relatively high spatial resolution (hundreds of nanometers) is smaller than the typical particle size used in lithium-ion battery cathode materials.[14-15] However, Raman mapping has not been widely used to

characterize lithium-ion batteries *in situ* for a number of reasons, including the low sensitivity thus long collection time, the potential for light-induced alteration of the battery materials and surface layers, and the difficulty in constructing an optical cell that will provide a uniform electric field distribution between the electrodes. Most prior Raman studies have conducted experiments *ex situ* [6, 16-17] or have focused on *in situ* but single-point characterizations of cathode and anode material due to these limitations.[18-24]

Recently, advances in high-sensitivity CCD arrays have made it possible to perform Raman mapping experiments under low-intensity conditions with reasonable collection time. This enables *in situ* mapping of state-of-charge distribution of battery electrodes. Nishi et al. demonstrated successful *in situ* Raman imaging of $LiCoO_2$ cathode,[5] but have not discussed the cell design and imaging set-up in sufficient detail to be adopted by broader scientific audience. Other previous reports on *in situ* Raman cells [5, 15, 18-19, 21-26] for single-point measurements have typically used specially-designed cells that may not be structurally similar to conventional coin cells or may require substantial lead-time for machinery and cell parameter optimization. In our work, we seek to build from commercially available coin cell kits to demonstrate an *in situ* cell design that requires minimal optimization while maintaining the operating characteristics of commonly used coin cells.

In this work, we describe a simple approach to *in situ* Raman mapping based on industry-standard coin cells and a commercially available Raman spectrometer with an electron-multiplying charge-coupled devices (EMCCD) detector. . $LiNi_{0.5}Mn_{0.3}Co_{0.2}O_2$ (NMC) cathode is used to demonstrate cell performance. NMC gains popularity in recent years due to its superior performance compared with $LiCoO_2$, and its characterization *with in situ* Raman imaging has not been reported before.*In situ* Raman images of NMC cathodes were collected and both the spectral and electrochemical response

were compared with *ex situ* results to validate the performance. The collected maps were carefully examined to demonstrate the inhomogeneity in local charge-discharge profiles and the impact on battery cycle performance.

4.2 Experiment

2032 SS coin cell parts were purchased from Pred Materials International. A 1/8" diameter hole was drilled at the center of the coin cell top; this opening was covered with a MgO window that was bonded to the coin cell using 5-minute epoxy. The MgO substrates (1 cm×1 cm×2 mm) were purchased from SPI Supplies. To fit coin cell dimensions, we cut them into 5 mm×5 mm×2 mm pieces with a diamond cutter. A 300 nm aluminum film was deposited by electron-beam evaporation onto the window to act as a conductive layer. The central 2 mm diameter area of the window was covered with Kapton tape during evaporation to remain free of Al layer. After removal of the Kapton tape, we determined that the resistivity between the SS top and the Al-coated window was <3 Ω-cm, which was low enough to be considered conductive.

The cathode slurry contained 92 wt.% $LiNi_{0.5}Mn_{0.3}Co_{0.2}O_2$ (Toda, Inc., Particle Size 10±2 μm), 3.5% Carbon Black (Timcal Super C65) and 4.5% Polyvinylidene Fluoride (PVDF) (Solef), which were dispersed in N-methyl-2-pyrrolidone (NMP). The slurry was applied onto the Al layer by rolling a glass capillary, covering the central aperture on the MgO window. The cathode thickness was around 20-40 μm after drying, as measured by a Mitutoyo upright gage. The density of cathode film is estimated to be around 2.5-2.7g/cm³, corresponding to 40%-44% porosity. The NMC-coated cell top was heated at 150 °C overnight before assembly of the coin cell using an automated crimper (Hohsen).

Assembly of the *in situ* cell was done in an Argon glovebox maintained at < 1 ppm oxygen and water levels. The electrolyte containing 1M $LiPF_6$ in a 1:1 volumetric mixture of ethylene carbonate (EC) and

diethyl carbonate (DEC) were purchased from BASF Corporation. Celgard 2500 separators were obtained from Celgard, Inc and presoaked in electrolyte before use. Lithium anode was punched from lithium foil from Chemetall Foot Corp. The remainder of the cell was the same as a standard 2032 coin cell. The cell was crimped using the automated battery crimper. To test cells for their electrochemical performance, we used an Arbin BT2000 battery tester for cycling. The first two cycles were performed at a rate of C/10, and all subsequent cycles were performed at a charge-discharge rate at C/5. The current was calculated from the loading. In the example shown in Fig. 3 in the results session, the current was set to 35 µA for the first two cycles, and 70 uA for the rest. To test the performance at higher charge-discharge current, the cell was first cycled at C/10 for two times, and then charged at C/3 and discharged at different C-rates.

A Confocal Raman Imaging Microscope DXRxi from Thermo Fisher Scientific Inc. was used for Raman spectroscopy. The spectrometer utilized an electron-multiplying charge-coupled devices (EMCCD) detector for maximum sensitivity, allowing rapid collection and the use of low laser power below the damage threshold for the cathode materials. The cell was rigidly mounted to an automatic x-y scanning stage. A 532 nm laser was focused on the back of electrode with a 50X long-working-distance objective. The focal spot size was approximately 1 µm, smaller than one NMC particle (average particle size 10 µm). The laser was set at 3 mW power to avoid laser damage of NMC particles due to thermal heating. In one control experiment, we've continuously mapped the surface for 24 hours and observed no change in the spectral features using the 3 mW laser. In the data shown in the paper, a 35×35 µm area was chosen for mapping collection. During collection, the automatic sample stage moved the cell along X and Y directions in 1 µm steps. Each spectrum took 8 s to collect, and each mapping took 50 min. For the data we show in Fig. 4.5 to Fig. 4.7, the cell was cycled at 0.08 mA

between 3 V and 4.3 V using a Keithley 2400 sourcemeter, and it took 8 hours to charge and discharge during the first cycle. After completion of the experiment, the cell potential for each mapping was determined by matching the elapsed time on the charge-discharge curve.

For comparison with batteries fabricated under more typical, industry-standard fabrication techniques, *ex situ* spectra were also collected with electrodes from disassembled coin cells. The coin cells contain the same electrolyte and anode as in the *in situ* case. The cathode was slurry coated on an Al current-collector, and calendared at a pressure of 1 ton/cm^2 before cycling. The loading was 10.9 mg/cm^2, and density was 3.17 g/cm^3. The cell was charged to different voltages at C/10, and the cathodes were taken from disassembled coin cells. A 50X objective was used to focus the beam on the front surface of the electrode, and the laser power was 10 mW.

4.3 Results and Discussions

4.3.1   Design Considerations of the *in situ* Cell

The most important design consideration of the *in situ* cell is to incorporate an optically transparent window while maintaining functional similarity with the regular coin cells. Fig. 4.1 shows the cross-sectional and top-down view of the *in situ* cell. One key design element is that the Al current collector and active material are deposited directly onto the window used for Raman excitation and collection. An ideal window material would be both conductive and would not generate its own Raman or fluorescence features. After evaluating several materials, we chose MgO as the window material because it produced no detectable fluorescence background or Raman signal in the 200-3500 cm^{-1} range [27]. We have tried a few other commonly-used window materials and included their spectra in Fig. A3.1. None of those material outperforms MgO. The central region of the MgO window was left without an

Al layer during deposition and the cathode slurry was directly applied on top of it. Therefore, it became necessary to ensure that the voltage drop across this piece of electrode was sufficiently small and negligible. The following calculation was done to determine the relationship of voltage drop across the film and the size of the aperture on the MgO window. To illustrate the basic assumptions, Fig.4.1b summarizes the geometry of the $LiNi_{0.5}Mn_{0.3}Co_{0.2}O_2$ cathode film on the Al support.

Our analysis assumes that the Li intercalation current from electrolyte to the front surface of cathode is homogeneous. The current density (j) at the electrolyte-electrode interface is estimated to be 0.0032 mA/mm^2, based on 0.08 mA current and 25 mm^2 MgO surface area. The resistivity of the film is assumed to be 10 Ω.cm based on literature data for composite $LiCoO_2$ cathode that contains carbon black and PVDF.[28] To estimate the maximum potential difference within the circular aperture area, we used a simple analysis assuming that the current into the center of the aperture must come in radially through the NMC films. For an aperture of radius R, the volume of the unsupported electrode is $4\pi R^2 h$, where h is the thickness of the cathode film. The measured value of h is 20-30 μm, and the value used in the calculation is 20 μm. For a given point inside this volume, along cylinder of radius r (marked in Fig. 4.1b), the current flowing from the electrolyte to the cylinder equals $j*\pi r^2$. For an infinitesimally thin hollow cylinder with internal diameter of r, and outer diameter of r+dr, the resistivity can be calculated as follows:

$$R = \frac{\rho L}{A}$$

$$dR = \frac{\rho dL}{A} = \frac{\rho dr}{2\pi rh}$$

The predicted voltage drop cross this infinitely thin cylinder can be calculated:

$$dV = IdR = j\pi r^2 . \frac{\rho dr}{2\pi rh} = \frac{j\rho}{4h}dr^2$$
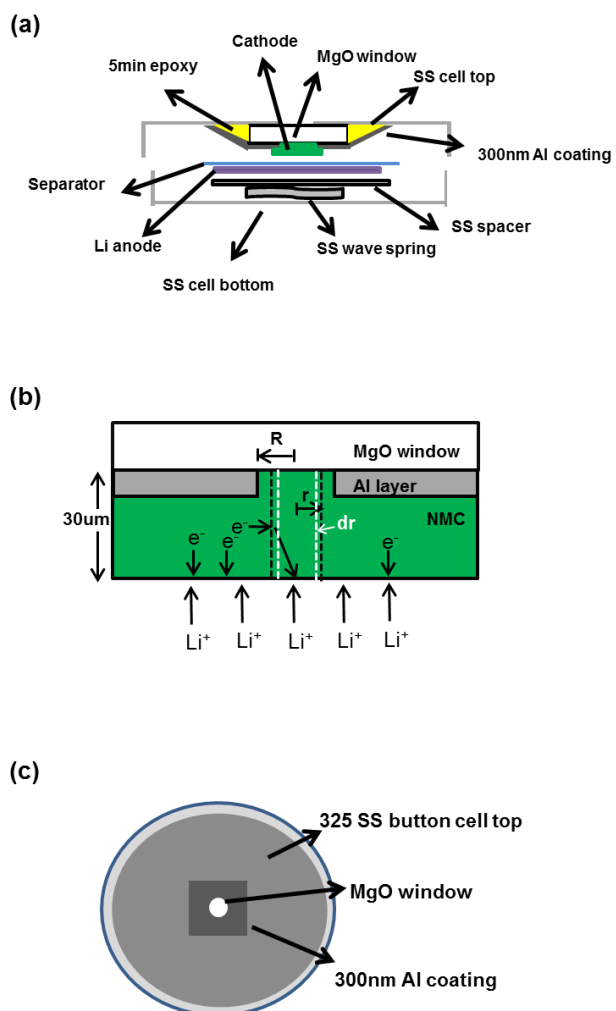
(a)

(b)

(c)

Figure 4.1 (a) Cross-section view of *in situ* cell (b) Enlarged cross-sectional view of cell top (c) Bottom-up view of cell top. Marked dimensions are intended to illustrate parameters used in resistance estimation.

For an unsupported film with radius R, the total voltage drop is:

$$V = \int dV = \int_0^R \frac{j\rho}{4h} dr^2 = \frac{j\rho}{4h} R^2$$

For an NMC film,

$$\rho = 10\Omega - cm$$

$$j = \frac{0.0032mA}{mm^2}$$

$$h = 20um$$

$$R = 1mm$$

Therefore

$$V = 0.004 \ V$$

Based on the calculation, the voltage drop equals 0.004 V for the dimension in our cell (unsupported area of 2 mm in diameter). As comparison, kT/e equals 0.0256 V at room temperature. The voltage drop is smaller than the thermal energy of an electron, and we can neglect the voltage variance across the unsupported cathode film. Any observation of significantly different local potential would be due to intrinsic inhomogeneity of the electrode instead of an artifact in cell design.

4.3.2 Performance Validation of the *in situ* Raman Cell

We characterized the electrochemical performance of the *in situ* cell by investigating the intercalation and de-intercalation of $LiNi_{0.5}Mn_{0.3}Co_{0.2}O_2$ cathodes. Fig. 4.2a compares the voltage-capacity curve of one *in situ* cell and one regular coin cell. Both cells a clear plateaus starting at 3.7 V, corresponding to the onset of lithium intercalation. Comparable charge and discharge capacity is obtainable with the modified *in situ* geometry. The values also match literature-reported capacity of 150-200 mAh/g for NMC.[29-31] Fig. 4.2b shows the capacity retention of the *in situ* cell cycled at C/5

between 3 V and 4.3 V. The cell shows no failure over 20 repeated cycles, demonstrating good electrochemical performance.

In repeated measurements with the *in situ* cell, we observe capacities ranging from 150 to 200 mAh/g capacity for the first cycle; sample-to-sample variations arise because a small amount of the slurry coated on the vertical side of the MgO window will not be electrochemically active due to lack of contact with electrolyte but will still be included in the active mass calculation. We extract first-cycle efficiency of 88%±3%, which matches the value of 84%-90% in our regular coin half cells. The stable electrochemical characteristics show that the overall geometric configuration of our *in situ* Raman cell is similar to that of an unaltered coin cell.

Prior studies have established that the NMC as a layered α-NaFeO$_2$-type structure, with a Raman active mode of A$_{1g}$ symmetry arising from M–O stretching vibrations and a mode with E$_g$ symmetry arising from O–M–O bending vibrations, and the intensity and frequency of the Raman bands will change with the degree of lithiation.[32-33] To further verify that the cathode particles cycled in the *in situ* cell had the same charge-discharge characteristics as electrodes in regular coin cells, we compared *in situ* Raman single-point spectra during the first charging process with both literature reports and *ex situ* results. Fig. 4.3 shows the spectral evolution during charging in both the *in situ* (Fig. 4.3a) and *ex situ* (Fig. 4.3b) case. We focus first on the features below 1000 cm^{-1}, which are associated with the lattice vibrations of NMC. The *in situ* spectrum in Fig. 4.3a exhibits a strong peak at 592 cm^{-1} and a shoulder-like peak at 478 cm^{-1} at fully lithiated state. The precise frequencies of these modes vary with both the composition of the oxide and with the state of lithiation. For LiCoO$_2$, these bands lie at 595 cm^{-1} (A$_{1g}$) and 485cm^{-1} (E$_g$) at fully lithiated state.[32-35] Since NMC has three transition metal ions, the A$_{1g}$ and E$_g$ modes are both split into multiplets. Previous reported values are at approximately 467, 483, 510, 547,
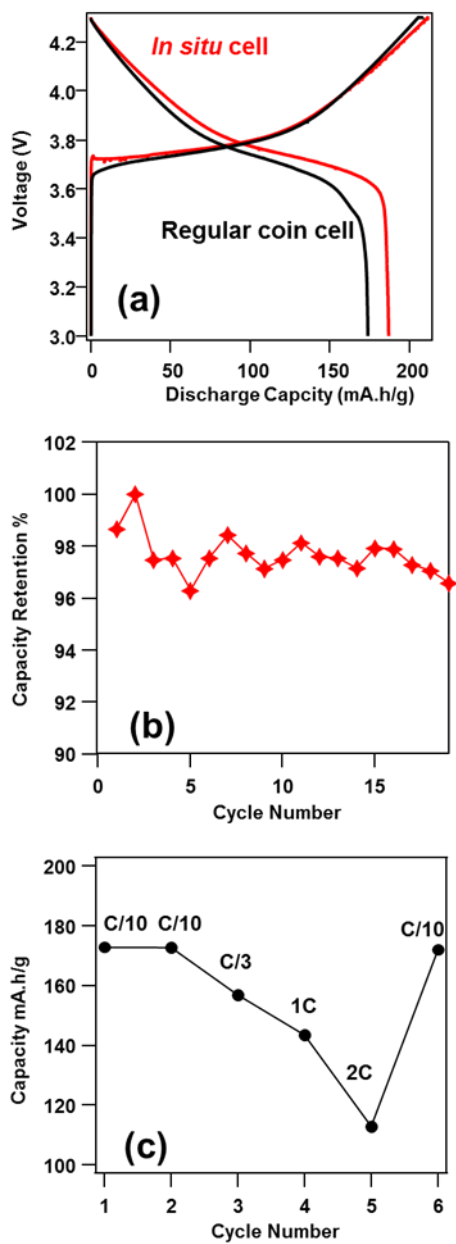
Figure 4.2 *In situ* **cell performance (a) Charge and discharge curve compared with regular coin cell (b) Retention of discharge capacity over the first 20 cycles (c) Rate test of the** *in situ* **cell**
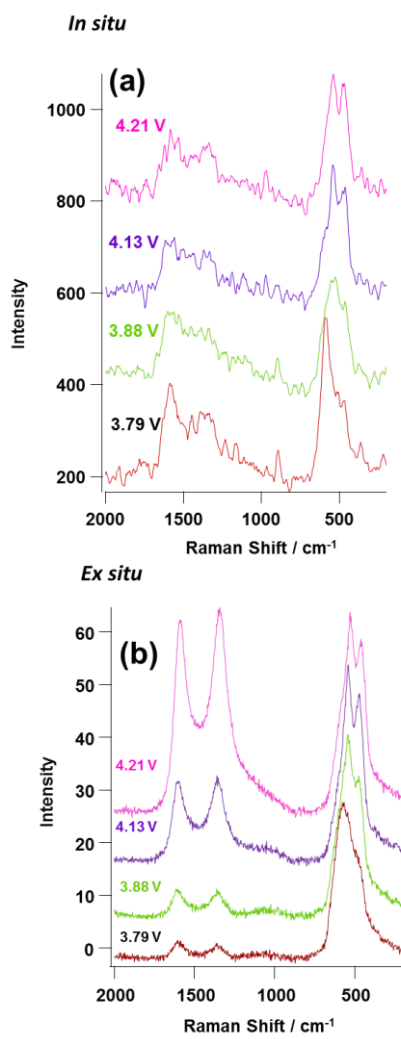
Figure 4.3 a) *In situ* **and b)** *ex situ* **Raman spectra during first charging process**

591 and 625 cm^{-1} with the specific frequencies depending on the stoichiometry of the mixed oxide.[36-37] To simplify the discussion, we assign our 592 cm^{-1} band to A_{1g} and 488 cm^{-1} band to E_g without further deconvolution into six fine bands. During the charging process, after the onset of cathode de-lithiation around 3.8V, the Raman bands downshift in frequency. In the *in situ* spectra, the A_{1g} bands downshift from 592 to 530 cm^{-1}, and E_g from 488 to 459 cm^{-1}. In the *ex situ* spectra, the A_{1g} bands downshift from 574 to 538 cm^{-1}, and E_g from 471 to 466 cm^{-1}. The slight differences in absolute frequencies are attributed to the shift in the degree of lithiation when an electrode loses contact with electrolyte. In the *ex situ* case, we have taken the electrode from disassembled coin cells and it is reasonable to expect slight self-charge or self-discharge during the transport to spectrometer. Literature has attributed the band downshift to the expansion of the c-axis caused by lithium deintercalation [34]. Our observation is consistent with the literature- for example, the $LiCoO_2$ peaks at 596 and 486 cm^{-1} shift downward to 584 and 480 cm^{-1} as the material is delithiated [34]. In addition to the band downshift, we also observed a slight decrease in A_{1g} vibration intensity in both the *in situ* and *ex situ* spectra. The decrease in intensities is explained in terms of decreased optical skin depth due to increased electrical conductivity upon delithiation [18]. The consistency between *in situ* and *ex situ* spectra demonstrates good electrical contact within the film and good activity of the NMC particles, which further validates the functional similarities between the *in situ* cell and regular coin cells. Fig. 2c shows the rate capability test of the in situ cell. The cell demonstrates reasonable capacity at up to 2C.

Fig. 4.3 also shows two broad bands at 1580 cm^{-1} and 1335 cm^{-1}, which matches well with the frequencies of pure carbon black at 1575 cm^{-1} and 1340 cm^{-1} (See Fig. A3.2). Finally, we attribute the peak at 892 cm^{-1} to the C=O bending of the ethylene carbonate solvent, and the bands near 3000 cm^{-1} (shown in Fig. A3.5) to C-H stretch of EC/DEC electrolyte, based on prior literature reports [38] and our

own experimental spectra of these components in Fig. A3.2. The visible appearance of the electrolyte peak indicates that the back of the cathode is in good contact with the electrolyte during Li intercalation. Overall, the *in situ* cell provides satisfactory electrochemical performance and a clear spectroscopic window for the characterization of active particles during cycling.

4.3.3 Raman Mapping with the *in situ* Cell

State-of-charge mappings were constructed of a 35×35 µm region on the NMC cathode. Two spectral features have been used to represent the local state-of-charge: peak intensity and peak position. As shown in previous discussion, the delithiation process is characterized by the downshift of A_{1g} and E_g bands, the decrease of A_{1g} peak intensity and increase of E_g peak intensity. The spectral evolution is reversed during lithiation process.

Fig. 4.4 shows the peak intensity mapping of the A_{1g} band. A similar set of mappings made from E_g Raman peak is shown in Fig. A3.3. As discussed previously, the peak maximum of A_{1g} shifts with the degree of lithiation. Therefore, the A_{1g} intensity was taken at different wavenumber for each image and these were marked in figure caption. In Fig. 4.4, three NMC particles are highlighted. The diameter of the particles are around 5-10 um with inter-particle distance around 5um, and the size and distribution are consistent with SEM images of composite cathode shown in Fig. A3.4. As the cathode potential is increased from 2.3 V (Fig. 4.4a) to 4.2 V (Fig. 4.4c), all three particles show attenuated A_{1g} vibrations; as the voltage is decreased to 3.16 V, the A_{1g} intensity increases again. It is challenging to build a direct relationship between absolute peak intensity and the state-of-charge (SOC) because peak intensity also depends on factors such as particle's vertical distance to the focus point. However, we can still use the recoverability of the peak intensity to obtain meaningful interpretations. In Fig. 4.4a, the three marked

particles have comparable A_{1g} intensities. Comparison with Fig. 4.4f shows that Particle #1 and Particle #2 almost reverts back to the original intensity after one cycle, but the intensity of Particle #3 remains low compared with the other two particles. We interpret the incomplete intensity recovery as an early sign of particle deterioration: Particle #3 does not fully lithiate during the charging process though it is still active.

As discussed previously, the peak position is another indicator of the local state of charge. Unlike peak intensity, the peak position is unaffected by particle's relative location to the focus point. Therefore, it is a more suitable indicator of the local state-of-charge. We extracted peak position from each single-point spectrum by fitting the NMC bands with two Lorentzian peaks, and constructed the contour mapping in Fig. 4.5. The black area is where no NMC particles are present. From Fig. 4.5a, 5b and 5c, we can see the downshift of A_{1g} from around 590 cm^{-1} to around 540 cm^{-1} as the cathode is discharged of lithium. We can clearly identify inhomogeneity in state-of-charge distribution. At 3.88 V, most of particle #1 sit at around 540 cm^{-1}, but the upper region sits at 590 cm^{-1}, indicating delayed delithiation. When the electrode is charged further to 4.21 V, we can see that the same region has higher wavenumber than the rest of the particle. We mark the region in discussion as "under-delithiated". By contrast, the pointed region on particle #3 is "over-delithiated" as indicated by the lower wavenumber. This observation is consistent with Fig. 4.4 where low peak intensity indicates incomplete lithiation of Particle #3.

In Fig. 4.6, we examined the single-point spectra on Particle #1 and #3. Fig. 4.6a and Fig. 4.6b shows two representative spots, A and C, during first charging process. The arrow in each plot marks the voltage at which significant A_{1g} frequency downshift (approximately from 590 cm^{-1} to 545 cm^{-1}) is observed. The downshift first occurs on spot C (Particle #3) at 3.84 V, followed by spot A (on Particle
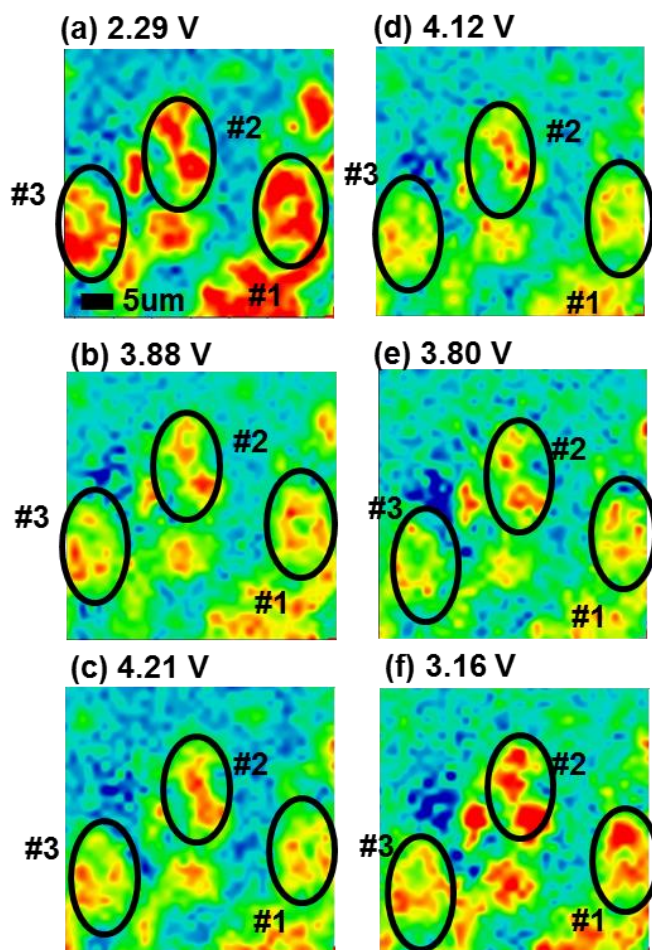
Figure 4.4 Mappings of NMC A$_{1g}$ vibration intensities during charging (a,b,c) and discharging (d,e,f). The peak frequency used to construct mapping are (a) 591cm^{-1} (b) 556cm^{-1} (c) 547cm^{-1} (d) 547cm^{-1} (e) 583cm^{-1} (f) 591cm^{-1}
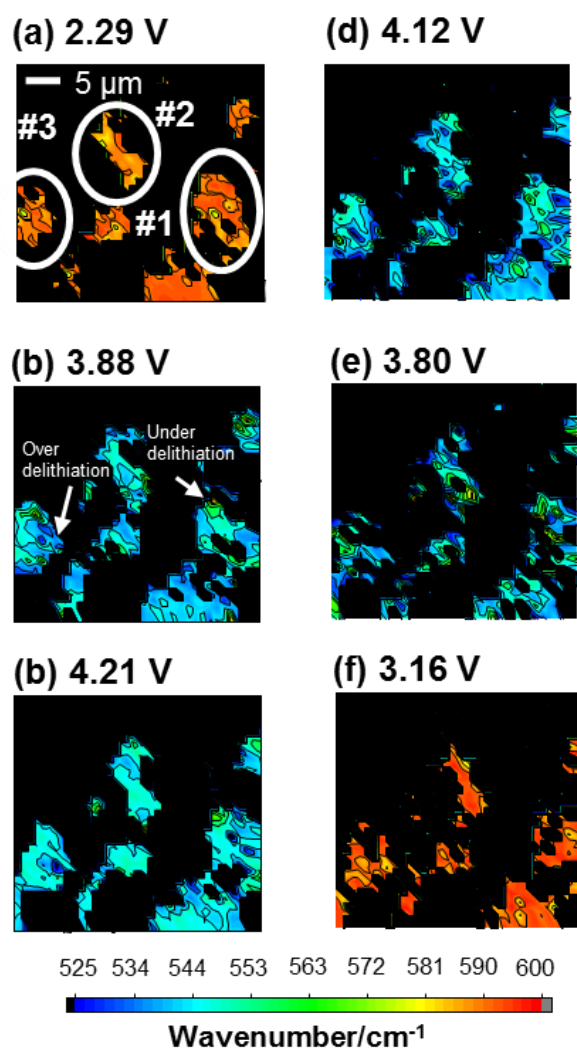
Figure 4.5 Mappings of NMC A$_{1g}$ vibrations position during charging (a,b,c) and discharging (d,e,f)
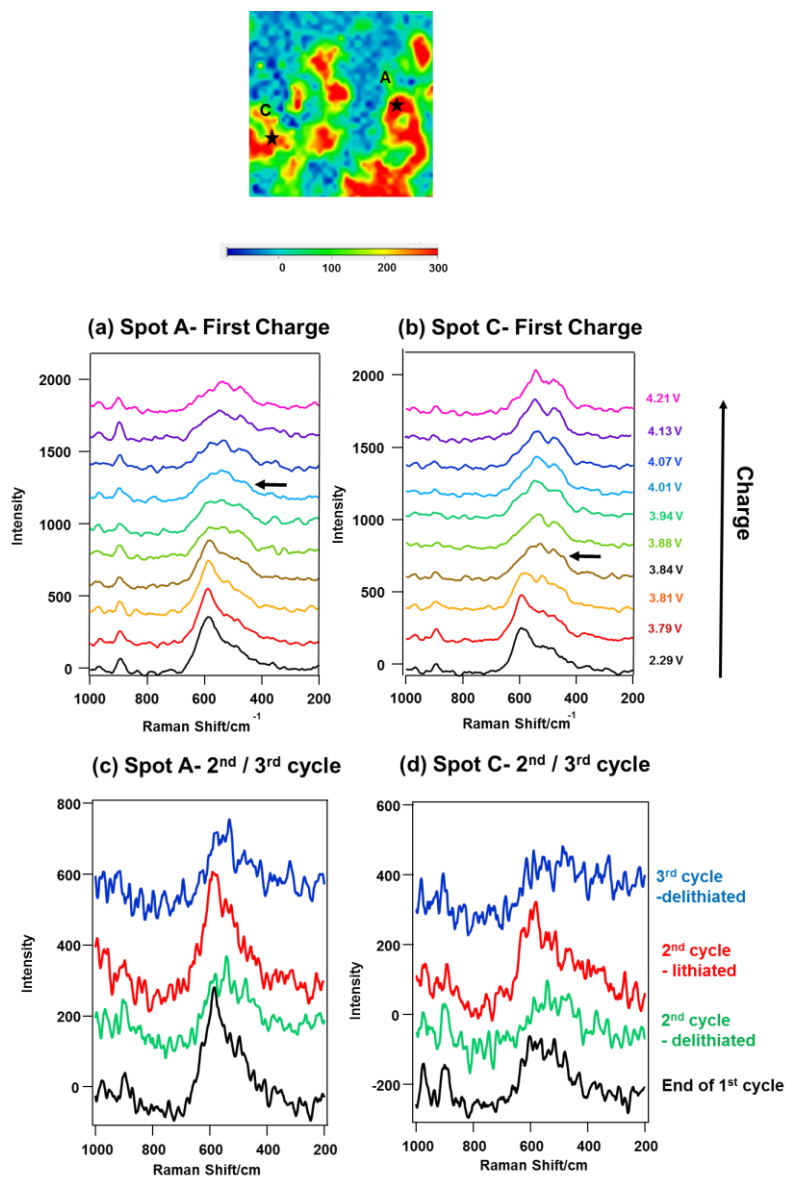
Figure 4.6 Single-point spectra of spot A and spot C during (a) (b) first charging and (c) (d) the second and third cycle. The positions are marked in the mapping. Arrows mark the onset of NMC peak downshift.

#1) at 4.01 V. The local difference of 0.2 V indicates significant inhomogeneity in the delithiation process. Fig. 4.6c and Fig. 4.6d tracks the two spots during the second and third cycle. Spot C from the "over-delithiated" region continues to show a lower A_{1g} frequency as well as peak broadening. We believe that early onset of delithiation on spot C during the initial cycle leads to an irreversible "over-delithiated" structure over the rest of cycles. That in turn leads to earlier material deterioration that is indicated by the peak broadening.

Fig. 4.7 compares in situ Raman mappings during C/6 and C/8 discharge. The data were collected of two separate in situ cells during the second discharge process. It is observed that discharge at different C-rate alters the degree of SOC inhomogeneity. Upon completion of C/6 discharge, Fig. 7c clearly indicates that some regions remain partially-lithiated (yellow-ish color) while others are fully lithiated (red-ish color), and that creates significant color gradients on the surface; for comparison, the surface after C/8 discharge (shown in Fig. 7f) is characterized by more homogeneous red-ish color. Overall, Fig.7 confirms the ability of the *in situ* cell to characterize electrochemical phenomenon at varying C-rates and potentially provide further insight into battery failure mechanisms.
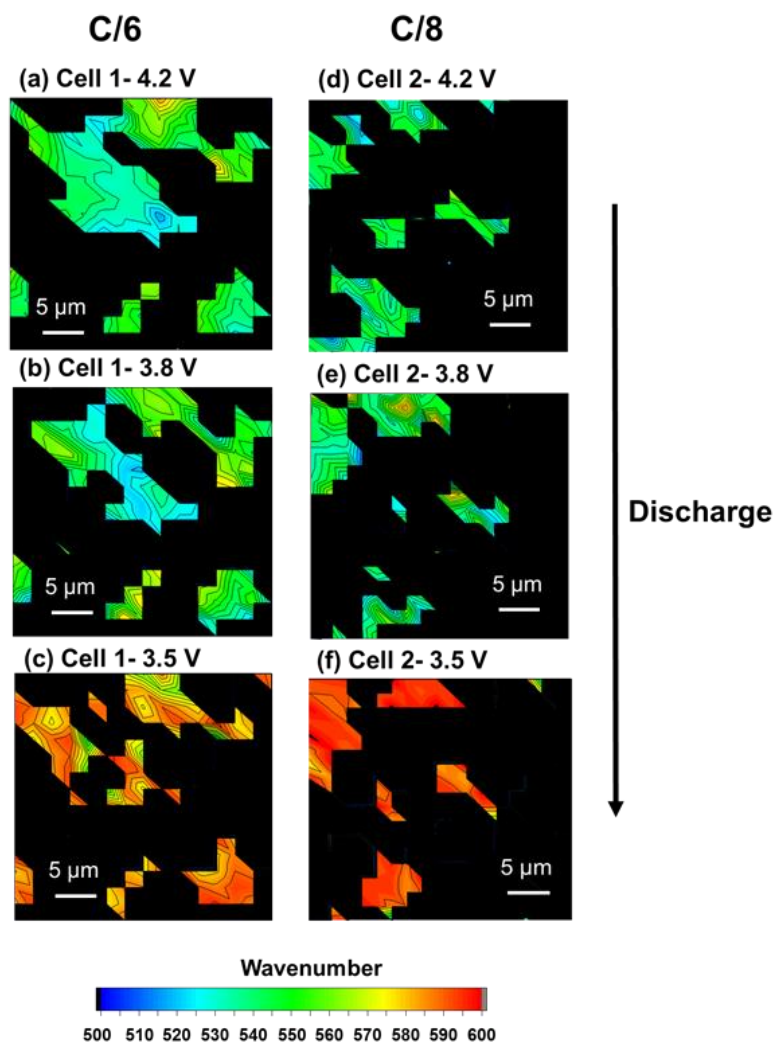
Figure 4.7 Raman images during (a) (b) (c) C/6 and (d) (e) (f) C/8 discharge.

4.5 Conclusions

We successfully set up an opto-electrochemical cell with a simple, effective *in situ* Raman configuration. Functional similarity between the *in situ* cell and regular coin cell were tested with $LiNi_{0.5}Mn_{0.3}Co_{0.2}O_2$ cathodes, and excellent electrochemical and optical performance were obtained. We show that peak position and intensity can be used to track the local state-of-charge to a spatial resolution of 1 μm, and that there is significantly inhomogeneous SOC between cathode particles and within a particular particle. Further investigation indicates that "over-delithiation" during first cycle is a cause of structural deterioration, and that increased C-rate also contributes to increased degree of SOC inhomogeneity. Overall, the cell design presented here provide a good platform for battery failure studies.

4.6 Reference

1.   Goodenough, J. B.; Kim, Y., Challenges for Rechargeable Li Batteries. *Chemistry of Materials* **2010,** *22* (3), 587-603.

2.   Tarascon, J. M., Key challenges in future Li-battery research. *Philos. Trans. R. Soc. A-Math. Phys. Eng. Sci.* **2010,** *368* (1923), 3227-3241.

3.   Arora, P.; White, R. E.; Doyle, M., Capacity fade mechanisms and side reactions in lithium-ion batteries. *Journal of the Electrochemical Society* **1998,** *145* (10), 3647-3667.

4.   Cai, L.; An, K.; Feng, Z.; Liang, C.; Harris, S. J., In-situ observation of inhomogeneous degradation in large format Li-ion cells by neutron diffraction. *Journal of Power Sources* **2013,** *236*, 163-168.

5.   Nishi, T.; Nakai, H.; Kita, A., Visualization of the State-of-Charge Distribution in a $LiCoO_2$ Cathode by In Situ Raman Imaging. *Journal of the Electrochemical Society* **2013,** *160* (10), A1785-A1788.

6.   Kostecki, R.; Lei, J. L.; McLarnon, F.; Shim, J.; Striebel, K., Diagnostic evaluation of detrimental phenomena in high-power lithium-ion batteries. *Journal of the Electrochemical Society* **2006,** *153* (4),

A669-A672.

7.   Kehrwald, D.; Shearing, P. R.; Brandon, N. P.; Sinha, P. K.; Harris, S. J., Local Tortuosity Inhomogeneities in a Lithium Battery Composite Electrode. *Journal of the Electrochemical Society* **2011,** *158* (12), A1393-A1399.

8.   Maire, P.; Evans, A.; Kaiser, H.; Scheifele, W.; Novak, P., Colorimetric determination of lithium content in electrodes of lithium-ion batteries. *Journal of the Electrochemical Society* **2008,** *155* (11), A862-A865.

9.   Nanda, J.; Remillard, J.; O'Neill, A.; Bernardi, D.; Ro, T.; Nietering, K. E.; Go, J. Y.; Miller, T. J., Local State-of-Charge Mapping of Lithium-Ion Battery Electrodes. *Advanced Functional Materials* **2011,** *21* (17), 3282-3290.

10. Lei, J. L.; McLarnon, F.; Kostecki, R., In situ Raman microscopy of individual $LiNi_{0.8}Co_{0.15}Al_{0.05}O_2$ particles in a Li-ion battery composite cathode. *Journal of Physical Chemistry B* **2005,** *109* (2), 952-957.

11. Migge, S.; Sandmann, G.; Rahner, D.; Dietz, H.; Plieth, W., Studying lithium intercalation into graphite particles via *in situ* Raman spectroscopy and confocal microscopy. *Journal of Solid State Electrochemistry* **2005,** *9* (3), 132-137.

12. Chueh, W. C.; El Gabaly, F.; Sugar, J. D.; Bartelt, N. C.; McDaniel, A. H.; Fenton, K. R.; Zavadil, K. R.; Tyliszczak, T.; Lai, W.; McCarty, K. F., Intercalation Pathway in Many-Particle $LiFePO_4$ Electrode Revealed by Nanoscale State-of-Charge Mapping. *Nano Lett.* **2013,** *13* (3), 866-872.

13. Braun, A.; Wang, H. X.; Funk, T.; Seifert, S.; Cairns, E. J., Depth profile analysis of a cycled lithium ion manganese oxide battery electrode via the valence state of manganese, with soft X-ray emission spectroscopy. *Journal of Power Sources* **2010,** *195* (22), 7644-7648.

14. Shao, M. H., In situ microscopic studies on the structural and chemical behaviors of lithium-ion battery materials. *Journal of Power Sources* **2014,** *270*, 475-486.

15. Baddour-Hadjean, R.; Pereira-Ramos, J. P., Raman Microspectrometry Applied to the Study of Electrode Materials for Lithium Batteries. *Chem. Rev.* **2010,** *110* (3), 1278-1319.

16. Panitz, J. C.; Novak, P., Raman microscopy as a quality control tool for electrodes of lithium-ion batteries. *Journal of Power Sources* **2001,** *97-8*, 174-180.

17. Kerlau, M.; Marcinek, M.; Srinivasan, V.; Kostecki, R. M., Studies of local degradation phenomena in composite cathodes for lithium-ion batteries (Reprinted from Electrochimica Acta vol 52, pg 5422-5429, 2007). *Electrochimica Acta* **2007,** *53* (3), 1385-1392.

18. Novak, P.; Panitz, J. C.; Joho, F.; Lanz, M.; Imhof, R.; Coluccia, M., Advanced in situ methods for the characterization of practical electrodes in lithium-ion batteries. *Journal of Power Sources* **2000,** *90* (1), 52-58.

19. Itoh, T.; Sato, H.; Nishina, T.; Matue, T.; Uchida, I., In situ Raman spectroscopic study of Li_xCoO_2 electrodes in propylene carbonate solvent systems. *Journal of Power Sources* **1997,** *68* (2), 333-337.

20. Huang, W. W.; Frech, R., *In situ* Raman spectroscopic studies of electrochemical intercalation in $Li_xMn_2O_4$-based cathodes. *Journal of Power Sources* **1999,** *81*, 616-620.

21. Hintennach, A.; Novak, P., A novel combinative Raman and SEM mapping method for the

detection of exfoliation of graphite in electrodes at very positive potentials. *Journal of Raman Spectroscopy* **2011,** *42* (9), 1754-1760.

22. Gross, T.; Giebeler, L.; Hess, C., Novel in situ cell for Raman diagnostics of lithium-ion batteries. *Review of Scientific Instruments* **2013,** *84* (7).

23. Dokko, K.; Mohamedi, M.; Anzue, N.; Itoh, T.; Uchida, I., In situ Raman spectroscopic studies of $LiNi_xMn_{2-x}O_4$ thin film cathode materials for lithium ion secondary batteries. *Journal of Materials Chemistry* **2002,** *12* (12), 3688-3693.

24. Itoh, T.; Anzue, N.; Mohamedi, M.; Hisamitsu, Y.; Umeda, M.; Uchida, I., Spectroelectrochemical studies on highly polarized $LiCoO_2$ electrode in organic solutions. *Electrochemistry Communications* **2000,** *2* (11), 743-748.

25. Itoh, T.; Abe, K.; Mohamedi, M.; Nishizawa, M.; Uchida, I., In situ SERS spectroscopy of Ag-modified pyrolytic graphite in organic electrolytes. *Journal of Solid State Electrochemistry* **2001,** *5* (5), 328-333.

26. Luo, Y.; Cai, W. B.; Xing, X. K.; Scherson, D. A., In situ, time-resolved Raman spectromicrotopography of an operating lithium-ion battery. *Electrochemical and Solid State Letters* **2004,** *7* (1), E1-E5.

27. Gasparov, L.; Jegorel, T.; Loetgering, L.; Middey, S.; Chakhalian, J., Thin film substrates from the Raman spectroscopy point of view. *Journal of Raman Spectroscopy* **2014,** *45* (6), 465-469.

28. Peterson, S. W.; Wheeler, D. R., Direct Measurements of Effective Electronic Transport in Porous Li-Ion Electrodes. *Journal of the Electrochemical Society* **2014,** *161* (14), A2175-A2181.

29. Wang, J.; Yao, X. Y.; Zhou, X. F.; Liu, Z. P., Synthesis and electrochemical properties of layered lithium transition metal oxides. *Journal of Materials Chemistry* **2011,** *21* (8), 2544-2549.

30. Shen, D. D.; Zhang, D. W.; Wen, J. W.; Chen, D. M.; He, X. J.; Yao, Y. J.; Li, X. L.; Duger, C., $LiNi_{1/3}Co_{1/3}Mn_{1/3}O_2$ coated by Al_2O_3 from urea homogeneous precipitation method: improved Li storage performance and mechanism exploring. *Journal of Solid State Electrochemistry* **2015,** *19* (5), 1523-1533.

31. Myung, S. T.; Izumi, K.; Komaba, S.; Sun, Y. K.; Yashiro, H.; Kumagai, N., Role of alumina coating on Li-Ni-Co-Mn-O particles as positive electrode material for lithium-ion batteries. *Chemistry of Materials* **2005,** *17* (14), 3695-3704.

32. Julien, C., Local cationic environment in lithium nickel-cobalt oxides used as cathode materials for lithium batteries. *Solid State Ionics* **2000,** *136*, 887-896.

33. Inaba, M.; Todzuka, Y.; Yoshida, H.; Grincourt, Y.; Tasaka, A.; Tomida, Y.; Ogumi, Z., Raman Spectra of $LiCo_{1-y}Ni_yO_2$. *Chemistry Letters* **1995,** (10), 889-890.

34. Inaba, M.; Iriyama, Y.; Ogumi, Z.; Todzuka, Y.; Tasaka, A., Raman study of layered rock-salt $LiCoO_2$ and its electrochemical lithium deintercalation. *Journal of Raman Spectroscopy* **1997,** *28* (8), 613-617.

35. Karan, N. K.; Saavedra-Arias, J. J.; Pradhan, D. K.; Melgarejo, R.; Kumar, A.; Thomas, R.; Katiyar, R. S., Structural and electrochemical characterizations of solution derived $LiMn_{0.5}Ni_{0.5}O_2$ as positive electrode for li-ion rechargeable batteries. *Electrochemical and Solid State Letters* **2008,** *11* (8), A135-A139.

36. Zhang, X. Y.; Mauger, A.; Lu, Q.; Groult, H.; Perrigaud, L.; Gendron, F.; Julien, C. M., Synthesis and characterization of $LiNi_{1/3}Mn_{1/3}Co_{1/3}O_2$ by wet-chemical method. *Electrochimica Acta* **2010,** *55* (22), 6440-6449.

37. Ben-Kamel, K.; Amdouni, N.; Mauger, A.; Julien, C. M., Study of the local structure of $LiNi_{0.33+d}$ $Mn_{0.33+d}$ $Co_{0.33-2d}$ O_2 (0.025 <= d <= 0.075) oxides. *Journal of Alloys and Compounds* **2012,** *528*, 91-98.

38. Katon, J. E.; Cohen, M. D., The Vibrational Spectra and Structure of Dimethyl Carbonate and its Conformational Behavior. *Canadian Journal of Chemistry-Revue Canadienne De Chimie* **1975,** *53* (9), 1378-1386.

Chapter 5
Conclusions and Outlook

In order to develop cathode materials with stable cycle performance, it is crucial to understand processes at the cathode-electrolyte interface. From this thesis, it is clear that the interfacial processes involve complicated interactions between different component inside the battery. In Chapter 2, we demonstrate that what is called a cathode-electrolyte interphase actually originates from the anode side. While this conclusion brings clarity on the CEI formation mechanism, it also raises questions on the actual function of artificial CEI (aka "coatings"). Our case study with Al_2O_3-coated cathode indicates that proper coating design can mitigate migration from the anode side. It will be an interesting future direction to understand whether migrant-repelling interface can be intentionally designed and how much it will contribute to better battery performance.

The study of silylated cathode in Chapter 3 is another example demonstrating complexity in coating design principles. Despite the conventional belief that crosslinked coatings are superior due to their stability and high coverage, we have demonstrated excellent performance with small, non-crosslinking molecules. A coating can serve more than one functions - in the case of silylated cathode, the Si-containing coating is both a protective barrier between cathode and electrolyte, and a group of molecular shuttles for interfacial ion transport. We propose that coatings can assist the desolvation of lithium-ion based on a hydrophobicity-performance correlation, which is an idea unexplored in the cathode field. As a future direction, we believe it is possible to design experiments monitoring interaction of different lithium-solvent complexes in electrolyte with the coated/uncoated surface to further explore the interfacial ion-transfer mechanism.

Chapter 4 focuses on the set up of *in situ* Raman mapping method. Development of *in situ* techniques is an important topic of battery research, and we have succeeded in designing a proper electrochemical cell that fits into analytical instruments. As a possible future direction, it will be interesting to use the method and explore problems such as comparison of SOC distribution in coated vs. uncoated cathode, or deconvolution of detailed band structure to understand detailed material evolution in ternary compounds.

Appendix 1

Supplementary Information for Chapter2 "Anode-originated SEI Migration for Formation of Cathode-Electrolyte Interphase"
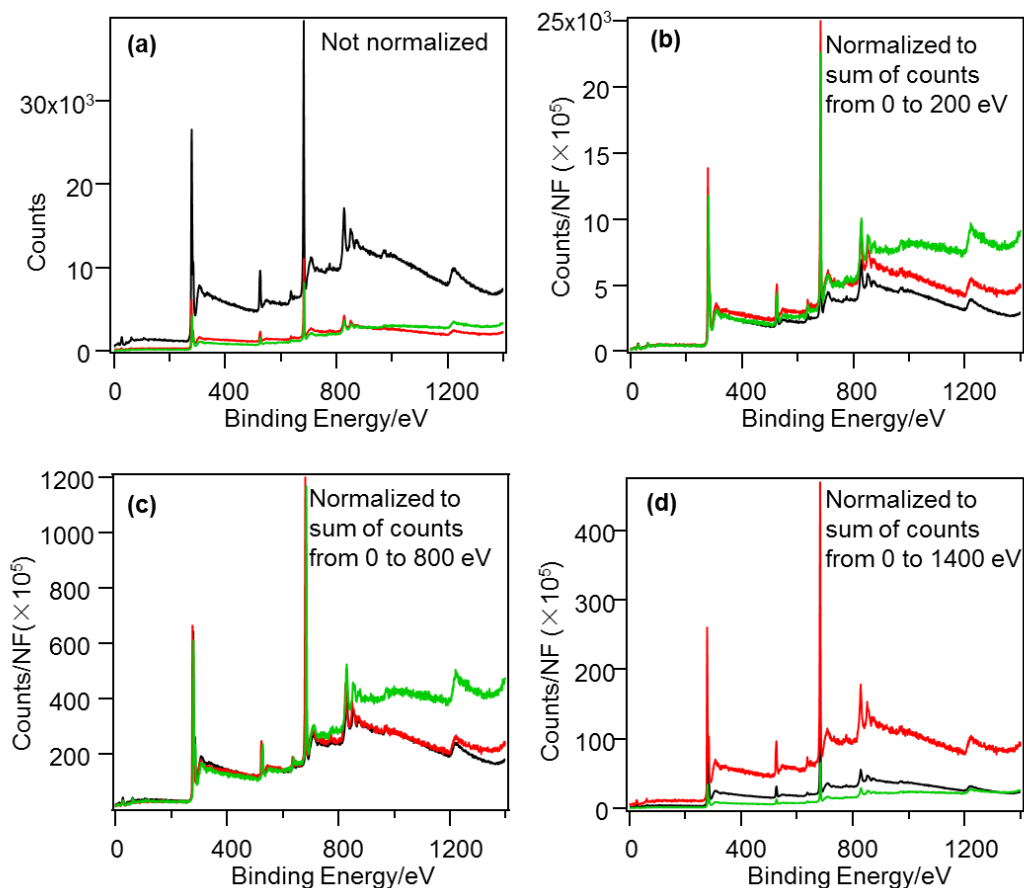"

Fig. A1.1 Survey spectra before normalization (a) and after normalization with (b) the sum of electron counts from 0 to 200 Ev, (c) the sum of electron counts from 0 to 800 eV, or (d) the sum of electron counts from 0 to 1400 eV

In XPS quantitative analysis, the raw spectra were normalized by a normalization factor to correct for the variance in total electron flux due to different alignment and instrument conditions on different days. To determine a proper normalization factor, we conducted an experiment where a single sample was placed in the XPS chamber, and the alignment was intentionally manipulated so that the total electron received by the detector changed. In Fig.S1a, three survey spectra were displayed, and they were collected of the same sample under different alignment conditions. A well-established normalization factor (NF) is expected to bring the spectra to the same/identical intensity since the three spectra were collected of the same sample. Fig. A1.1b, A1.1c and A1.1d shows the results from three different NF produced by summing up the total electron counts from 0 eV to 200, 800 or 1400 eV. It is

clear that NF in Fig. A1.1b and S1d is not proper because the survey spectra still show significant differences in baseline and peak intensity. In Fig. A1.4c, the three curves sit on top of each other in the range of 0-800 eV after normalization. For spectra in the range of 800-1200 eV, it is clear that curvature of background differs significantly between samples, and one normalization factor would not scale both the 0-800 and 800-1400 eV ranges simultaneously. Since the elemental peaks of interest all fall below 800 eV, it is determined that a proper normalization factor is (integrated electron counts between 0-800 eV in the survey spectra / 10^5). The 10^5 scaling factor is simply applied to ensure that the normalized spectra does not have extremely high or low intensity in order to facilitate further analysis with peak fittings.

To further testify this procedure, we took XPS multiplex spectra of a sample on different days. There was no intentional misalignment. Fig. A1.2 demonstrates the spectra before and after applying the normalization factor (NF). The normalization procedure successfully brought the spectra to same baseline level, and the peak intensity also matched better.
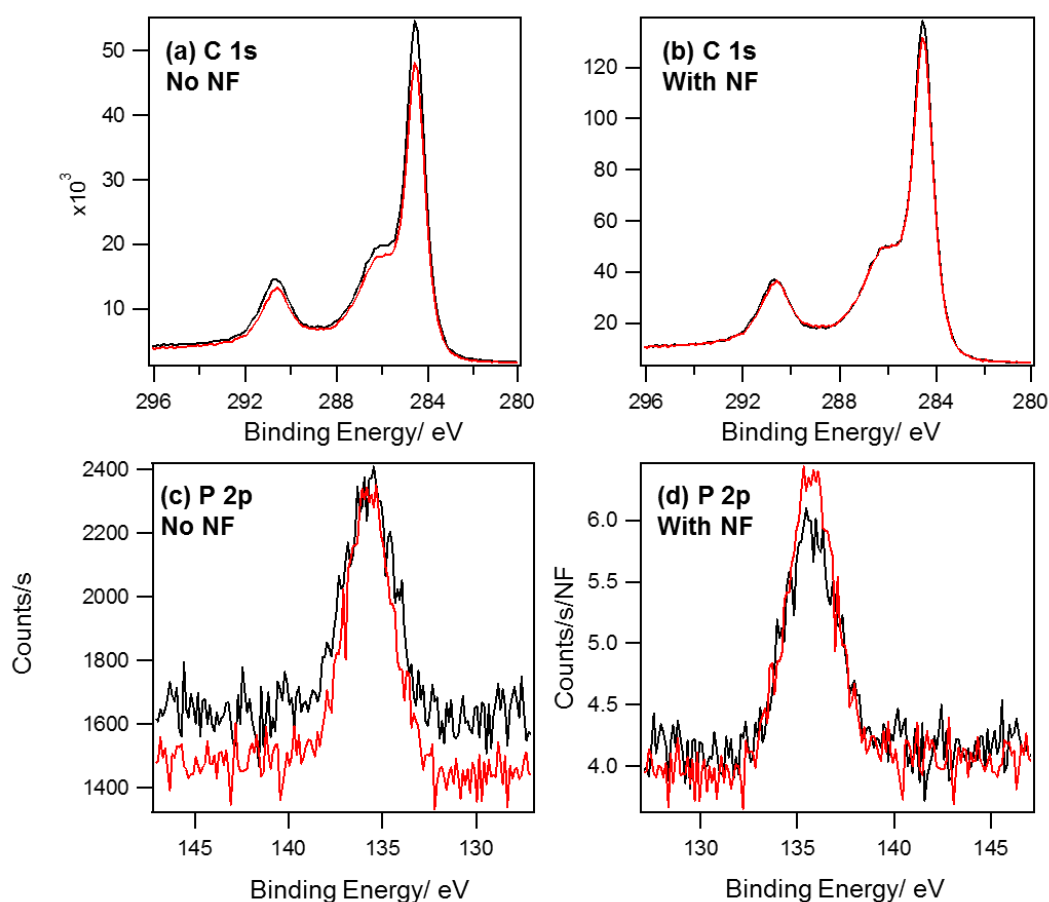
Fig. A1.2 Sample spectra before and after normalization

In Fig. 2.2, we discussed the Li-F correlation which indicates presence of LiF. Another group of CEI compounds that can contribute to the Li signal at 53eV is the $(Li)C_xH_yO_z$ (with C=O/C-O bonds). We therefore checked the Li-O and Li-C correlation to validate its presence. Fig. A1.3 shows the lack of quantitative correlation between Li-O and Li-C, indicating that $(Li)C_xH_yO_z$ is not the dominating species that give rise to the 53eV Li (1s) peak.
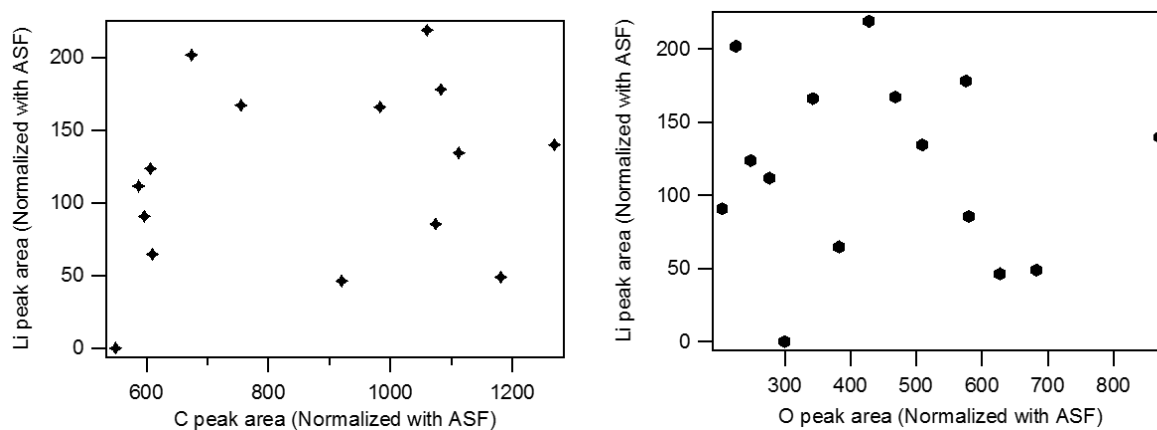

Fig. A1.3 Quantitative correlation of Li 53eV - C 286 eV intensity and Li 53 eV- O 532 eV peaks. Absence of positive correlation indicates that compounds such as Li₂CO₃ are not the major species contributing to the Li 53 eV peaks.

To eliminate interference originating from PVdF signals, we have prepared the electrodes binder-free. Fig. A1.4 summarizes the C (1s) and O (1s) XPS spectra of binder-free electrode. As discussed in the main text, the only significant peak in the C (1s) region comes from carbon black. During 1-4 cycles, there is little C-containing CEI formed. The O (1s) spectra also shows very little changes during 1-4 cycles. The O1s peak at 532 eV is assigned to native surface oxygen on the transition metal oxide.
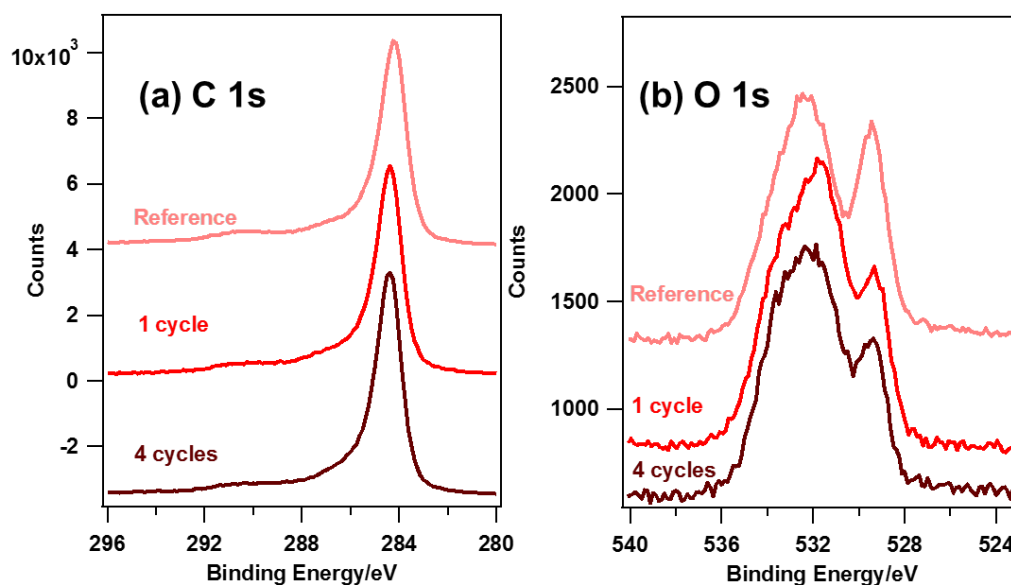
Fig. A1.4 C 1s and O 1s spectra of binder-free electrodes in the first four cycles

In Fig. 2.5 of the main text, we estimated IR drop due to addition of more separators based on differential capacity plots. Fig. A1.5 shows one set of differential capacity plots from one and three separator cells. The voltages in Fig. 2.5a were determined from the peak voltage.
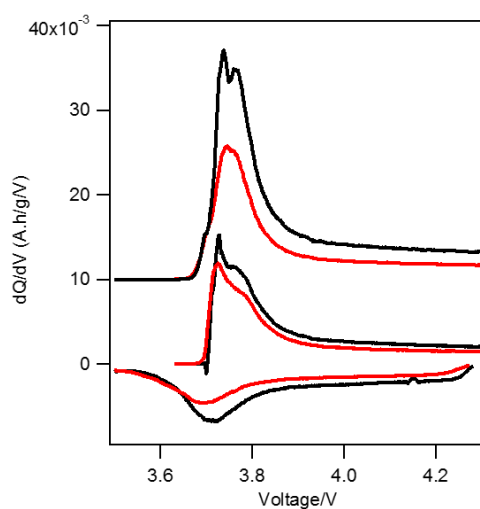

Fig. A1.5 Differential capacity plots of one and three separator cells. The C/10 data were vertically shifted for better display.

In the main text, we used NMC-LTO to see the effect of anode reactivity on CEI quantities. Fig. A1.6

shows the cycle performance of NMC-LTO cells. A noticeable feature is the very stable capacity and slow decay over cycles. This may be related to both little SEI formation and decreased CEI quantities via suppressed migration.
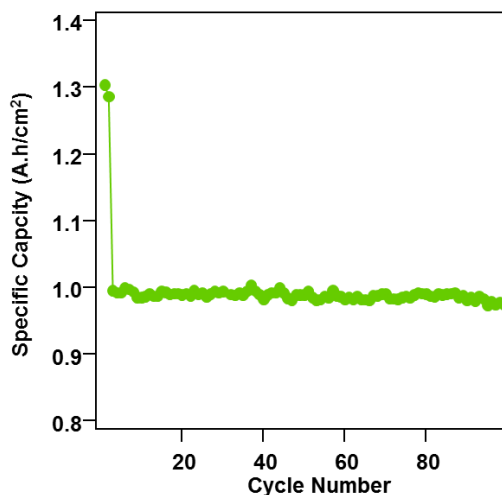
Fig. A1.6 Cycle performance of NMC-LTO full cells. The first two cycles are C/10 charge-discharge, and the following cycles are C/3 charge-1C discharge

In order to discuss anode-originated, it is essential to guarantee that the cathode-originated processes remain the same in NMC-LTO and NMC-graphite cells. That means NMC need to be charged to the same cut-off potential. Based on literature, we set the voltage window to be 1.6 V- 2.8 V in NMC-LTO cells. Fig. 2.7 examines the differential capacity plots during charging. In both types of full cells, the high cut-off is 1.2 V above the low voltage cut-off. In order to figure out the absolute potential on NMC, we can reference to the onset voltage of cathode delithiation V_{onset} or the peak delithiation voltage V_{peak}. Physically, V_{onset} (or V_{peak}) of cathode always is a constant value vs. Li/Li^+. As can be seen in Fig. 2.7a, V_{onset} in NMC-LTO and NMC-graphite cells falls at the exact same position relative to the 1.2 V window. That means NMC is charged to the same potential (vs. V_{onset}) in NMC-LTO and NMC-graphite cells. On the other hand, if we align the V_{peak}, potential cut-off in NMC-LTO cells is 0.03 V higher than NMC-graphite cells (shown in Fig. 2.6b). That means NMC is charged to higher potentials which will increase the amount of cathode-originated CEI. In either case, reduced CEI formation of NMC-LTO would have to be attributed to the existence of anode-originated processes. The cathode-originated CEI quantities

either remain the same or slightly increases in our NMC-LTO cells. The slight discrepancy in using onset vs. peak voltage is most likely due to the small shift of graphite potential during battery charging (differential capacity captures a summation of anode and cathode signals).
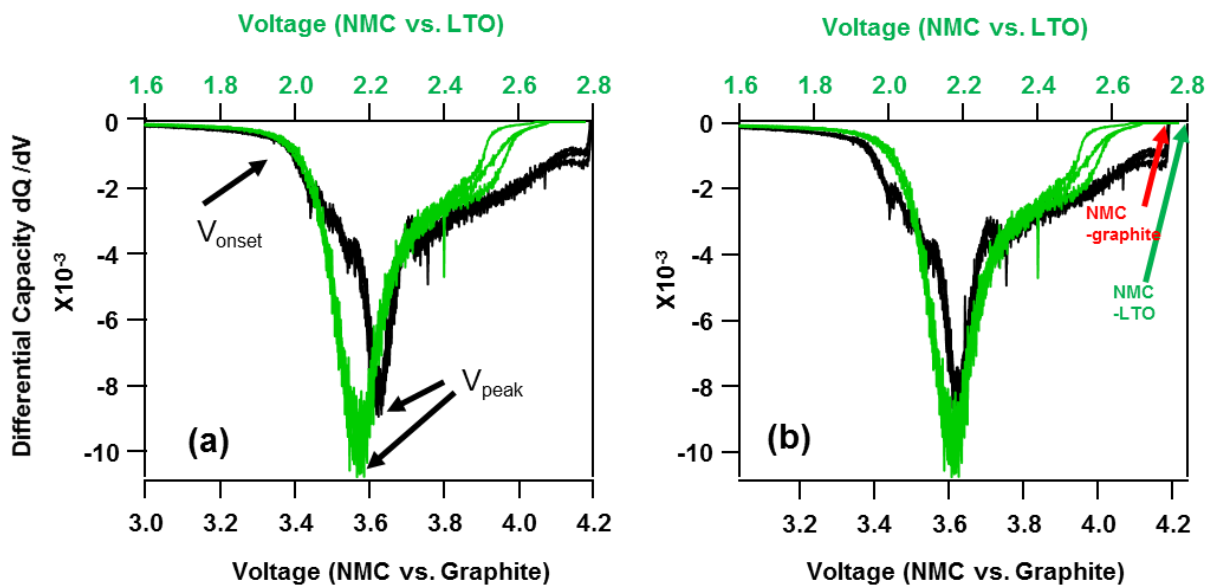

Fig. A1.7 Differential capacity plots of NMC-LTO (green) and NMC-graphite (black) full cells. In Fig.b, the voltage axis range is shifted to align the peak position.

Appendix 2

Supplementary Information for Chapter 3 "Improving performance of LiNi$_{0.5}$Mn$_{0.3}$Co$_{0.2}$O$_2$ cathode with surface silylation"

A2.1 Calculation of Si coverage on the surface

The coverage of trimethylsilyl (TMS) group on silylated cathode was calculated based on Si / Co ratio detected with XPS. The ratio was first corrected with atomic sensitivity factor (ASF). We assume that the surface layer is very thin so that elements in the bulk NMC and the surface layer are not attenuated by the surface layer.

In the first step, we calculate the intensity of Co signal from the following equation:

$$I_{Co} = N\rho_{Co}\lambda_{Co,NMC}\cos(\theta)$$

Where N is the total electron flux, ρ is the density of Co in the bulk NMC, λ is electron mean free path of Co in NMC, and θ equals 45° in our detector configuration. ρ can be calculated based on the unit cell size and stoichiometry. Based on literature[1], the unit cell has volume of 101.2 Å^3, and it contains Li$_3$M$_3$O$_6$ (M=Ni$_{0.5}$Mn$_{0.3}$Co$_{0.2}$). Therefore, ρ_{Co} = 5.93 atom/nm^3. The electron mean free path is calculated on the following equation[2]:

$$\lambda = 0.0129E^{0.7193}$$

Here E equals the kinetic energy E=1486.6 - Binding Energy (eV). The mean free path determined from this equation is 2.35nm for Co. Therefore,

$$I_{Co} = N * 5.93 * 2.35 * \cos(45) = 9.85N \ atoms/nm^2$$

Then we will calculate the intensity of Si coverage.

$$I_{Si} = N * \rho_{2D\_Si}$$

$$\frac{I_{Si}}{I_{Co}} = \frac{\rho_{2D_{Si}}}{9.85}$$

$$\text{For HM,} \quad \frac{I_{Si}}{I_{Co}} = 0.43 \quad \rho_{2D\_Si} = 4.2 \; atoms/nm^2$$

$$\text{For SILY,} \quad \frac{I_{Si}}{I_{Co}} = 0.79 \quad \rho_{2D\_Si} = 7.7 \; atoms/nm^2$$

$$\text{For PS,} \quad \frac{I_{Si}}{I_{Co}} = 4.93 \quad \rho_{2D\_Si} = 49 \; atoms/nm^2$$

A2.2 Toluene Control Sample

In HM and PS sample preparation, toluene is used as solvent during the treatment. To confirm the toluene as a solvent has no effect on the cell performance, a sample batch was prepared where NMC powder was treated by pure toluene solvent, and the performance was demonstrated in Fig. A2.1. The toluene-treated NMC has the same performance with untreated NMC. Performance improvement in the HM and PS samples is due to the use of silylation reagents.
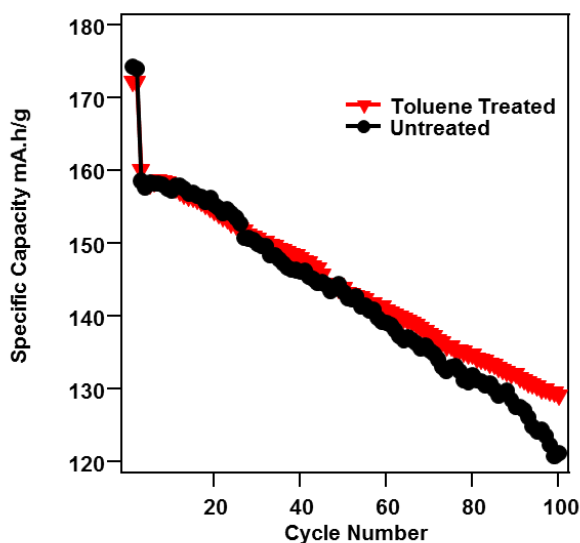
Fig. A2.1 Electrochemical performance of toluene-treated NMC

A2.3 CEI detection in C (1s) and O (1s) regions

In Fig. 3.6 of the main text, the F and P spectra were used to evaluate CEI formation on the NMC samples. Here the C 1s and O 1s regions are demonstrated.
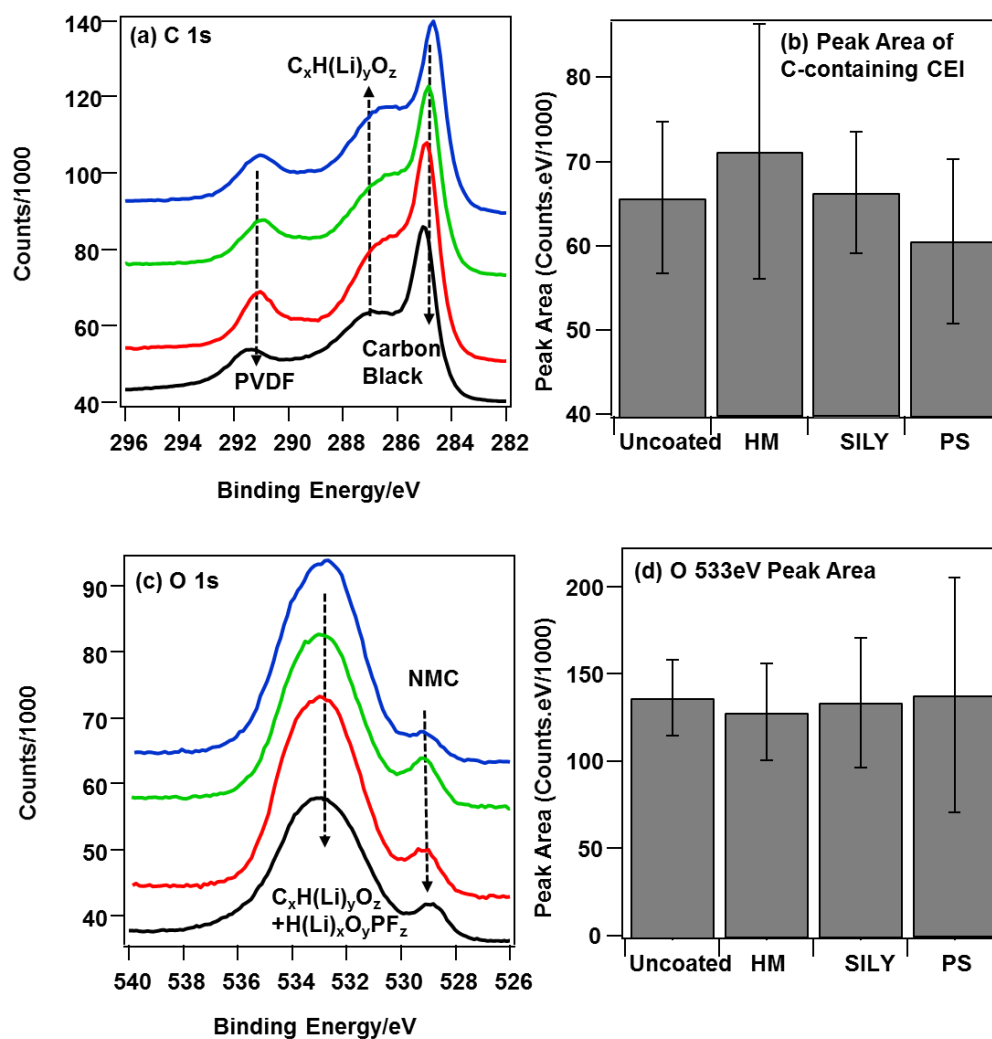
Fig. A2.2 XPS spectra of cathodes after 100 cycles (a) Representative C (1s) spectra (b) Average peak rea of C-containing CEI (c) Representative O (1s) spectra (d) Average peak area of O-containing CEI

A2.4 Contact angle measurement on composite cathode film

Fig. A2.3 summarizes the contact angle results obtained from composite cathode films. The cathode film is composed of NMC powder, PVDF binder and Carbon Black conductivity enhancer. Therefore, the droplet sits on a matrix of materials. It is still possible to identify trends of hydrophobicity. As is seen from the average contact angle from triplicate runs, the hydrophobicity of the cathode film increases with surface coverage in the order of uncoated<HM<SILY<PS. The absolute value of contact angle is higher than that observed of NMC powder pellet. It is because PVDF binder is quite hydrophobic itself. This figure further supports the conclusion from Fig. 3.8.
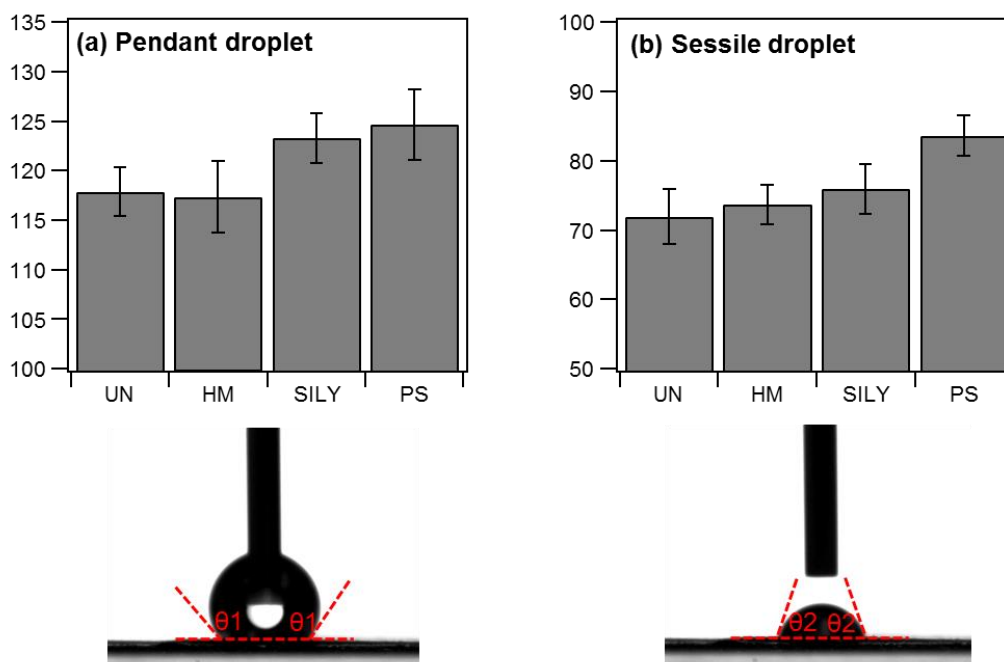
Fig. A2.3 Contact angle measurement on composite cathode film (a) Pendant droplet (b) Sessile droplet

A2.5 Matching dosage for HMDS in electrolyte vs. on cathode

One of the previously discussed mechanism involved HF scavenging through reaction with HMDS. In one experiment, we put HMDS directly in the electrolyte and match the dosage of HMDS to the TMS groups on NMC surface. Based on the coverage of 4.2 Si/nm^2 for the HM sample, surface area of $0.5m^2/g$ NMC and 0.02 g NMC per coin cell, we estimate that 0.69 μmol of TMS (trimethylsilyl) groups are present per cell. During coin cell assembly, a total of 40μL electrolyte was added. As a result, 0.018mol/L HMDS in electrolyte will match the dosage of TMS per HM cell. Similarly, 0.033mol/L HMDS will match the dosage of SILY cell. Fig. 3.9 in the main text demonstrates the cell performance with free HMDS in electrolyte both with matched dosage (0.018mol/L) and over dosage (0.033mol/L).

A2.6 Study of hydroxyl concentration-reactivity relationship

In the main text, we hypothesize that surface hydroxyls can act as reactive centers that catalyze electrolyte decomposition. In order to testify validity of this statement, chemical treatments were

performed on bare NMC cathodes to manipulate the number of hydroxyls. The NaOH treated sample
was obtained by stirring 2g NMC with 10 mL PH=11 NaOH for three hours at RT; The H_2O_2 sample
was obtained by stirring 2g NMC with 30% H_2O_2 for three hours at 130 ˚C; The 500 ˚C heated sample
was obtained by heating 2g NMC under continuously Argon flow at 500˚C for 6 hours inside a tube
furnace. Besides the 500˚C sample, all other samples were heated at 130 ˚C under vacuum for 15
hours before characterization. FTIR spectra were collected for 1% w/w powder in KBr and referenced
to pure KBr. Thermal mass spectra were collected with 0.1g NMC powder and 1mL electrolyte in the
vial. Other parameters for characterization is the same as described in experimental session.
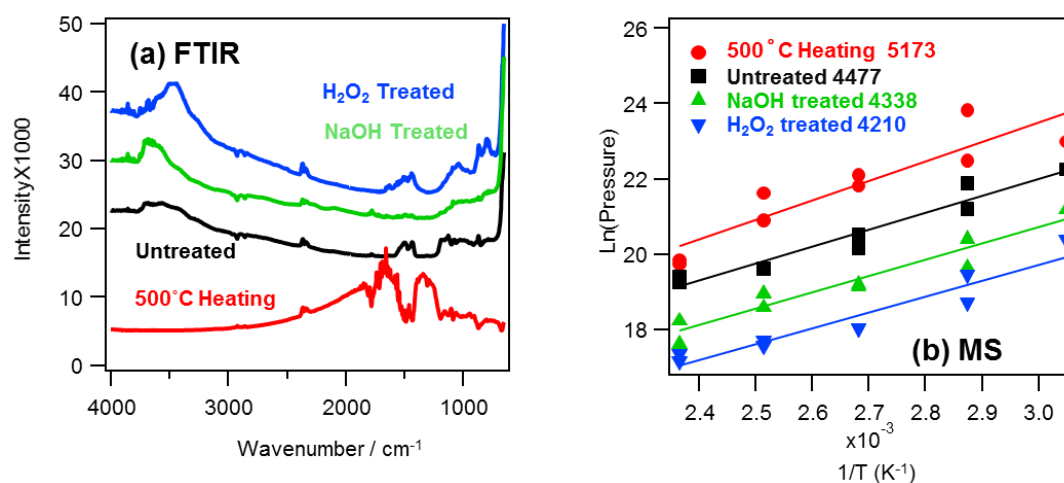

Fig. A2.4 Characterization of samples with varying amount of hydroxyls with (a) FTIR and (b) Thermal MS

From Fig. A2.4a, it is concluded that the NaOH and H_2O_2 treatments increased the amount of
hydroxyls on the surface. Hydroxyl vibrations were identified as the broad peak in 3300-3600 cm^{-1}
range. Heat treatment reduced the amount of surface hydroxyls, as evidenced by the lack of OH peak
in the red curve. Fig. A2.4b demonstrates the reaction barrier estimation from thermal MS. The
magnitude of reaction barrier follows: 500˚C treated > Untreated > NaOH treated > H_2O_2 treated. As
the number of hydroxyls increases, the reaction barrier for electrolyte decomposition decreases. This
experiment supports the statement that surface hydroxyls can act as reactive centers that catalyze
electrolyte decomposition.

1.   Shang, S. L.; Wang, Y.; Wang, W. Y.; Fang, H. Z.; Liu, Z. K., Low energy structures of lithium-ion battery materials Li(MnxNixCo1-2x)O-2 revealed by first-principles calculations. *Applied Physics Letters* **2013,** *103* (5), 5.

2.   Smith, G. C., Evaluation of a simple correction for the hydrocarbon contamination layer in quantitative surface analysis by XPS. *Journal of Electron Spectroscopy and Related Phenomena* **2005,** *148* (1), 21-28.

Appendix 3

Supplementary Information for Chapter 4

"Cell design for *in situ* Raman Mapping of Inhomogeneous State-of-Charge Profiles in Lithium-Ion Batteries"

A3.1 Determination of proper window material for the cell

Our *in situ* cell uses MgO window because it has no detectable fluorescence background or Raman signal in the 200-3500 cm^{-1} range. In the search process of a proper window, we tried a few other commonly used material including CaF_2, sapphire and quartz. Fig. A3.1 displays the Raman spectra when NMC electrodes are probed through different window candidates. The bottom spectrum is with no window material, and clear NMC Raman bands can be seen between 600-400 cm^{-1}. Both sapphire and quartz have a relatively strong peak starting around 500 cm^{-1}, which overlaps with the NMC peak and makes it difficult to quantify NMC features below 500 cm^{-1}. CaF_2 window shows several peaks around 500 cm-^{1}, so it is also not a good window for our experiment.
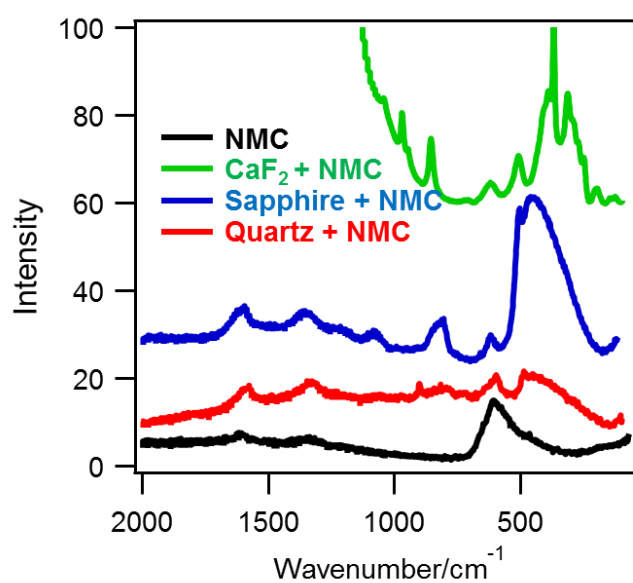
Fig. A3.1 Raman spectra of candidate window material

A3. Assignment of Raman spectra based on spectra of individual component

In the main text, we assigned the two broad bands at 1580 cm^{-1} and 1335 cm^{-1} in the *in situ* spectra to carbon black and CH stretch above 3000 cm^{-1} to electrolyte containing ethylene carbonate and diethyl carbonate. Fig. A3.2 supports this assignment with spectra collected from pure substances. The Raman spectra were collected on Thermo DXR Raman microscope with 10X objective and 532 nm laser at 10 mW power. All components were the same at used in *in situ* cells. The electrolyte contains 1M $LiPF_6$ in 1:1 ethylene carbonate/diethyl carbonate.
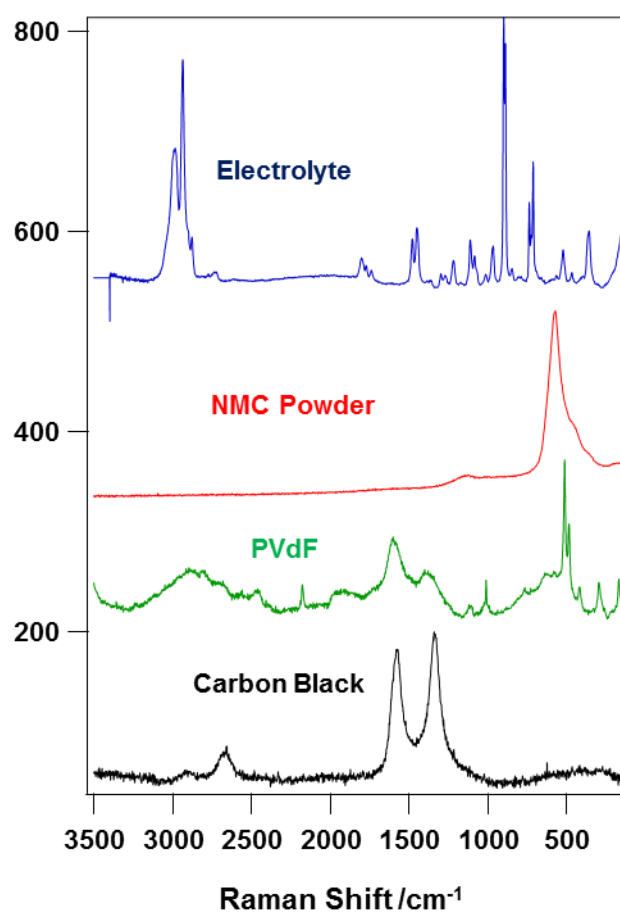
Fig. A3.2 Reference spectra of components in the cathode film.

A3.3 E$_g$-based mappings during first cycle

We have shown mapping constructed from A$_{1g}$ peak intensity in Fig.4. NMC has two vibrational modes, A$_{1g}$ and E$_g$. Fig. A3.3 demonstrates attenuation of Eg signal during charging and intensification during discharging. The trend is opposite to A$_{1g}$, and both can be used to track the delithiation / lithiation of NMC particles.
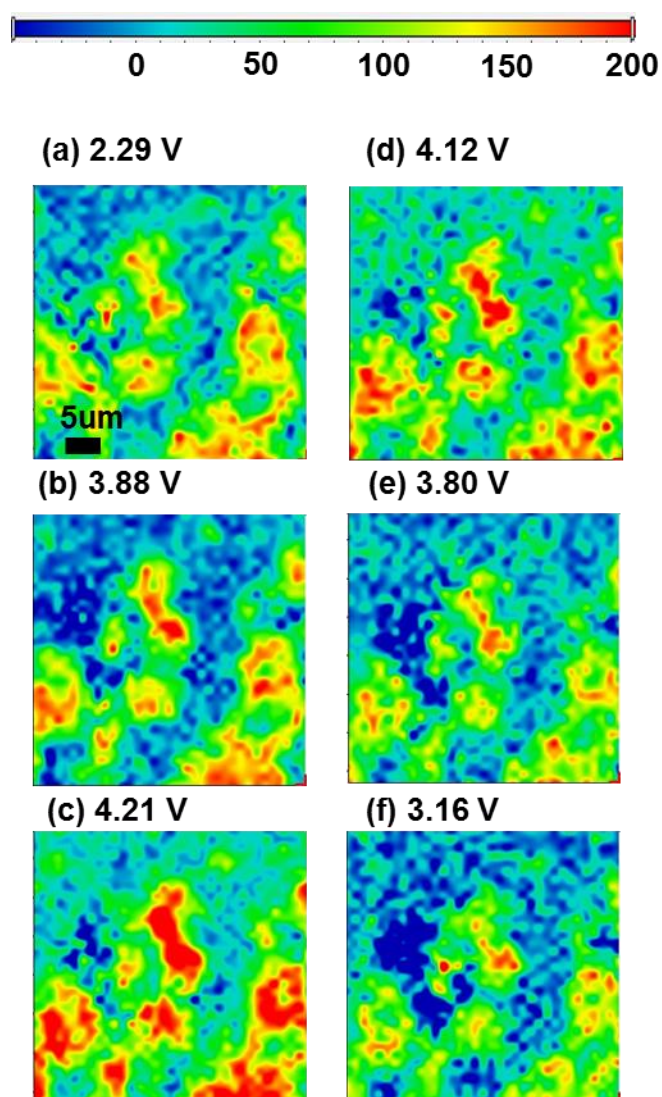

Fig. A3.3 Mappings of NMC E$_g$ vibrations during charging (a,b,c) and discharging (d,e,f). The peak frequency used to construct mapping are (a) 487cm^{-1} (b) 481cm^{-1} (c) 472cm^{-1} (d) 472cm^{-1} (e) 481cm^{-1} (f) 481cm^{-1}

A3.4 SEM image for particle size and particle distribution on cathode

SEM images in Fig. S3 demonstrate particle size and particle distribution on composite cathode surface. These were taken of the front side of the cathode film on a LEO Supra 55 VP field-emission instrument. Analysis of Fig. S3b with ImageJ software demonstrates NMC particle diameters between 4-18 μm with the average around 9.5 um. The specification from material supplier indicates D50 at around 10 μm, and so our SEM image is consistent with that. From Fig. S3, we can also determine that the inter-particle distance is normally between 0 μm to 20 μm.
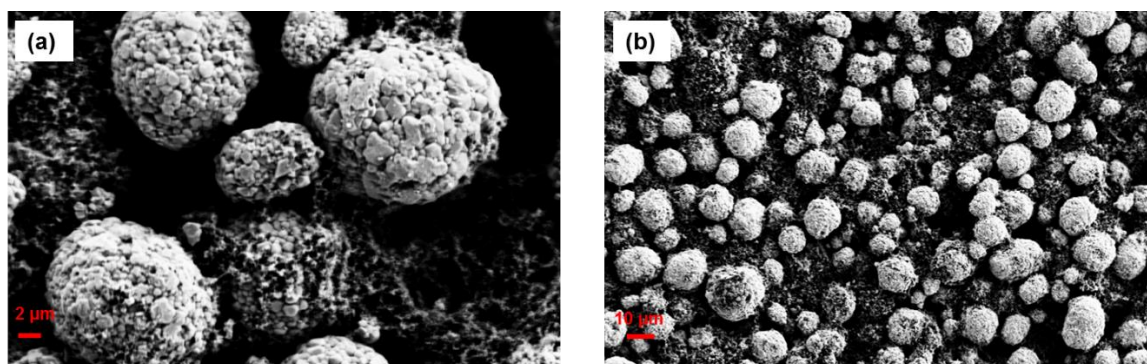

Fig. A3.4 SEM image of composite NMCcathodes

A3.5. Single-point spectra during first cycle

Fig. A3.5 shows single point spectra on different particles during charging and discharging. Some of that information is contained in Fig. 4.5 of the main text. In Fig. A3.5, we also show the spectra during discharging. All spectra are plotted in the range of 3600-200 cm^{-1} so that electrolyte peak above 300cm^{-1} can be clearly seen. The positions of spot A, B and C have been marked in Fig. 4.5.
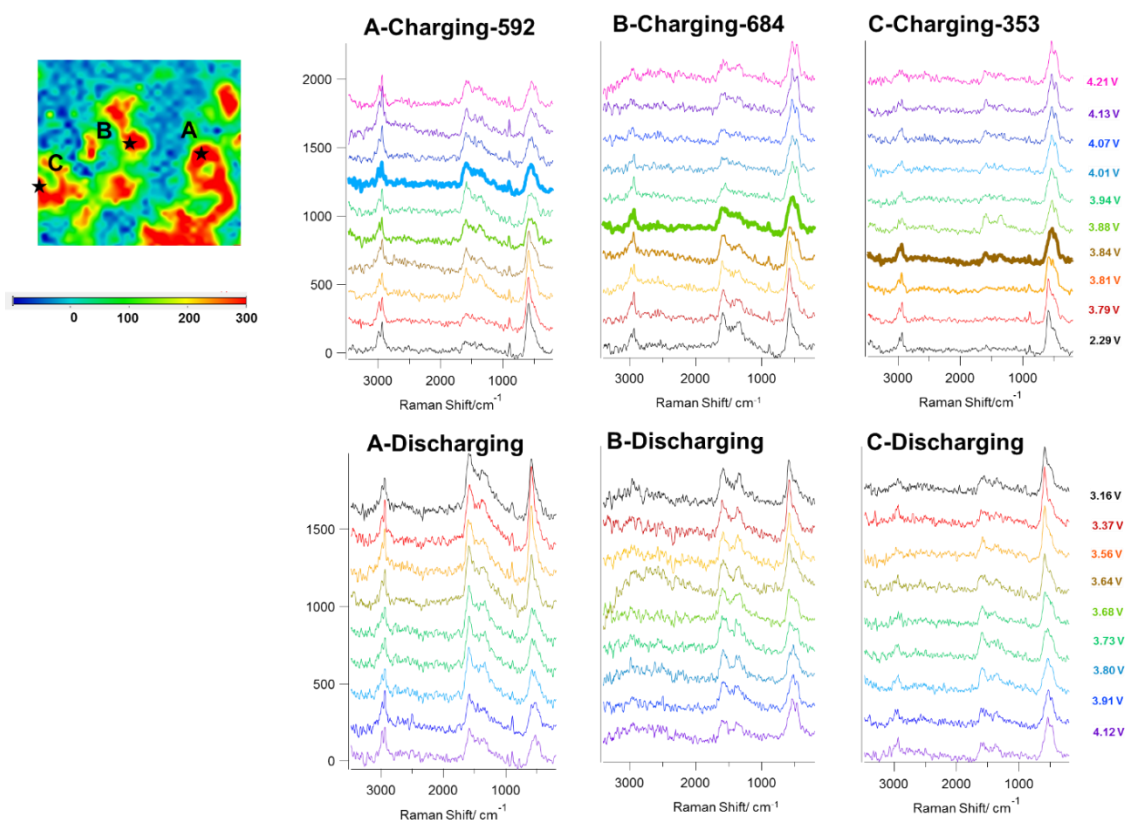
Fig. A3.5 Single-point Raman spectra of NMC particles during first cycle.